COUPLED FLOW AND GEOMECHANICS SIMULATION IN PRODUCTION MANAGEMENT

A Thesis

by

KEJUN JIN

Submitted to the Office of Graduate and Professional Studies of
Texas A&M University
in partial fulfillment of the requirements for the degree of

MASTER OF SCIENCE

Chair of Committee	George J. Moridis
Co-Chair of Committee	Thomas A. Blasingame
Committee Member	Zenon Medina-Cetina
Head of Department	Jeff Spath

May 2020

Major Subject: Petroleum Engineering

ABSTRACT

Pressure drawdown management plays a key technical role in reservoir management as it has an important impact on the estimated ultimate recovery (EUR) and, consequently, on the cash flow and economic viability. Thus, careful pressure depletion management, which controls production through choke management, can be used to attain maximal net present value. A frequently used current strategy is to use the largest available choke size and to maximize the production in order to recover the capital expenses as early as possible. However, there is evidence from a number of field production data that maximal production and estimated recovery can be accomplished by limiting the early production, a strategy that appears to increase recovery and long-term production.

This study aims to evaluate alternative drawdown management strategies for a specific reservoir in an effort to identify production strategies that maximize present-day and long-term production and ultimate recovery without geomechanically compromising the integrity of the hydraulic fracture (HF) by following strategies that may result in reduction of the HF aperture and productivity/performance because of adverse stress conditions.

The study has two components. The first component involves an analysis of field data from a reservoir of interest in an effort to identify possible correlations of production drawdown performance and choke setting during flowback. I estimate the flowing bottomhole pressure from the production rate, the surface pressure and the wellbore description, and I conduct a rate transient analysis in order to assess the properties and attributes of the reservoir and the fractures.

The second component of the study involves the analysis of a number of choke management and production practices associated with bottomhole pressure control. This is accomplished by means of numerical simulation of the coupled flow and geomechanical processes that are involved in the course of the production of reservoir fluids from hydraulically fractured shale oil reservoirs. For the needs of the project, (a) I developed a fully implicit, non-isothermal three-phase, three component compositional simulator to estimate production from a 3D shale oil multi-fractured horizontal well system and (b) I coupled the flow simulator with a pre-existing, validated 3D geomechanical model (based on the fixed-stress method) using a sequential implicit scheme. The two-way coupling of the flow and geomechanical simulators allowed the accurate description of the interdependence between the flow conditions and properties (pressure, phase saturation, porosity and permeability) and the geomechanical attributes (stresses, strains and displacements) in the course of the production. I used the numerical simulator to investigate the evolution of pressure, porosity, displacements and volumetric strains in the matrix and the fracture system under different pressure drawdown strategies. The estimated ultimate recovery is the criterion used for the evaluation of the various choke management strategies.

ACKNOWLEDGEMENTS

I would like to thank the following persons for their guidance and support throughout this research:

My committee chair, Dr. George J. Moridis,

My co-chair, Dr. Thomas A. Blasingame, and

My external committee member, Dr. Zenon Medina-Cetina

I would like to also thank my friends and the Department faculty and staff for making my time at Texas A&M University a great experience.

Finally, I thank my parents for their encouragement and support.

CONTRIBUTORS AND FUNDING SOURCES

Contributors

This work was supervised by a thesis committee consisting of Professor Dr. George J. Moridis and Dr. Thomas A. Blasingame of the Department of Petroleum Engineering and Professor Dr. Zenon Medina-Cetina of the Department of Civil Engineering.

Funding Sources

This graduate study was supported mainly by a grant from an unnamed sponsoring company, and to a lesser extent by a fellowship provided by the Texas Engineering Experiment Station and the Department of Petroleum Engineering at Texas A&M University through their start-up funding of the projects of Professor G. Moridis.

NOMENCLATURE

b	=	Biot's coefficient	dimensionless
$\mathbf{C}$	=	Elasticity tensor	Pa
$\mathbf{f}^k$	=	Mass flux vector of component *k*	$\mathrm{kg \cdot m^{-2} \cdot s^{-1}}$
m^k	=	Mass of component *k*	$\mathrm{kg \cdot m^{-3}}$
q^k	=	The source term of component *k*	$\mathrm{kg \cdot m^{-3} \cdot s^{-1}}$
ρ_b	=	Density of bulk	$\mathrm{kg \cdot m^{-3}}$
ρ_J	=	The fluid density of phase *J*	$\mathrm{kg \cdot m^{-3}}$
$\mathbf{g}$	=	Gravitational acceleration vector	$\mathrm{m \cdot s^{-2}}$
k	=	Rock intrinsic permeability	$\mathrm{m^2}$
k_{rJ}	=	Relative permeability of the phase *J*	dimensionless
p_{wf}	=	Bottomhole pressure	Pa
p_J	=	The pressure of phase *J*	Pa
S_J	=	Saturation of saturation J	dimensionless
s_{ir}	=	The irreducible saturation	dimensionless
T	=	Temperature	°C
X_J^k	=	Mass fraction of component *k* in phase *J*	kg/kg
ϕ	=	Porosity	dimensionless
Φ	=	The Langrage's porosity	dimensionless
μ_J	=	Viscosity of phase *J*	Pa S
α_T	=	Thermal dilation coefficient	dimensionless
α_p	=	Matrix pore compressibility	dimensionless
$\boldsymbol{\sigma}$	=	Cauchy total stress tensor	Pa
$\boldsymbol{\sigma}'$	=	Effective stress tensor	Pa
$\mathbf{u}$	=	The displacement vector	m
ε	=	The strain tensor	dimensionless
K_s	=	Intrinsic solid-grain bulk modulus	Pa
K_{dr}	=	Drained bulk modulus	Pa
Ω	=	Computational domain	
Γ	=	Boundary of computation domain	
$\mathbf{n}$	=	Normal vector of the boundary	
$\boldsymbol{x}_0$	=	The vector of the perturbation variables in history matching	
$\Delta \boldsymbol{x}$	=	The vector of the deviations of the perturbation variables from their optimal values	

SI Metrics Conversion Factor

m	×	3.280 840	E+00	=	ft
m^3	×	6.289 811	E+00	=	bbl
m^3	×	3.531 467	E+01	=	ft^3
Pa·s	×	1.0*	E+03	=	cp
°C		1.8×°C+32		=	°F
kg	×	2.204 623	E+00	=	lbm
Pa	×	1.450 377	E-04	=	psi
m^2	×	9.869 233	E-13	=	Darcy

*Conversion factor is exact.

TABLE OF CONTENTS

Page

LIST OF FIGURES

LIST OF TABLES

Page

CHAPTER I

INTRODUCTION

1.1 Background

Unconventional reservoirs, the majority of which are tight sand and shale plays, have recently become some of the most important energy resources in the US. This has been possible because of the introduction of effective reservoir stimulation technologies (mainly hydraulic fracturing), which are the reason for the dramatic increase in oil production from such reservoirs over the last 15 years. Thus, production from shale oil reservoirs has risen from negligible levels in 2005 to 59% of the total oil production in 2018 (U.S. EIA, 2019), contributing 6.5 million barrels per day. Production from shale oil reservoirs can be high initially as the fractures and the matrix in their immediate vicinity drain, but declines very rapidly because the very low permeability of the matrix inhibits continuous flows at sufficiently high rates from its interior toward the HF. This results in low recoveries that range between 3% and 10% of the Oil-In-Place (OIP) in the U.S. (US DOE, 2013; EIA, 2016; Todd and Evans, 2016). The rapidly declining production and the recovery from shale oil reservoirs may be further adversely affected by inadequate production strategies that involve over-aggressive choke management in an effort to maximize early production, leading to irreversible production loss. This loss is attributed to geomechanics-related factors that involve reduction in (or even closure of) the HF aperture because of proppant embedment in ductile media or proppant crushing/pulverization in harder media (Wilson, 2015).

Pressure drawdown management plays a key technical role in reservoir management and has a pronounced effect on the estimated ultimate recovery (EUR), cash flow, and acceleration of producer operations in hydraulic fractured tight/shale reservoirs. A careful pressure depletion management, which controls the well production rate or the bottomhole pressure (BHP), can lead to maximal EUR and net present value. A common current strategy is to use the largest available choke size and to maximize the production rate in order to recover the capital expenses as early as possible. However, there are field studies indicating that maximal production and estimated recovery were achieved by simply limiting the early production rate, a strategy that appeared to improve the long-term recovery. For example, Rojas and Lerza (2018) reported that aggressive choke management may cause a reduction in EUR of up to 20% in the Vaca Muerta Shale play in Argentina. Similarly, a severe productivity loss in the Haynesville shale gas play throughout the production life of the reservoir was attributed to such aggressive choke management practices (Okouma Mangha *et al.*, 2011). Conductivity losses in hydraulic fractures caused by geomechanical changes brought about by inappropriate choke management practices could result in substantial cumulative gas production reductions (Mirani *et al.*, 2018). The above-mentioned observations became the focus of comprehensive studies that used analytical, semi-analytical, and numerical solutions to characterize various features of productivity loss, including pressure-dependent properties, fracture conductivity decrease, etc. (Ilk *et al.*, 2011).

To summarize, drawdown management optimization is recognized as a challenging but rewarding endeavor. In this study, I would like to add my contribution to the limited number of scientifically robust studies on the subject of choke management in the literature, and to provide suggestions for optimal production management methods with respect to various criteria and the associated production schedules.

1.2 Objectives

The objectives of this work are as follows:

- To analyze historical field data from a reservoir of interest, including choke schedule, phase flowrates, and pressures, in an effort to develop, if possible, empirical correlations describing the relationship between production performance and drawdown management strategies both during early production (flowback) and during the later stages of production. I propose to use surface data and wellbore information to develop BHP estimates using the PROSPER software (IPM Prosper ,2018). The BHP information is a critical input in the subsequent numerical simulation studies to evaluate various alternative production management options.

- To develop a 3D non-isothermal, three-phase, three-component simulator of fluid and heat flow and transport through porous and fractured media; to fully couple the flow simulator with a pre-existing 3D geomechanics simulator based on the fixed-stress method using sequential implicit scheme.

- To use the coupled flow-geomechanical model and field data in order to conduct inverse (history matching) simulations in an effort to determine the flow parameters of the hydraulic fractures (HFs) and of the subdomains of the matrix (*i.e.,* the undisturbed matrix and the Stimulated Reservoir Volume, SRV) of the unconventional (shale oil) reservoir through an optimization process that minimizes deviations between numerical predictions and field observations. Rough estimates provided by the operator are used as initial parameter estimates in the history matching process.

- To use the coupled flow-geomechanical model in a forward (deterministic) model in order to evaluate alternative production management plans and BHP control strategies. The study and analysis here will not only investigate the coupled flow and geomechanical behavior of the system, but will also monitor production flows and changes in the flow and geomechanical conditions, properties and attributes of the system during production periods (short- and long-term). A critical parameter to be monitored is the possible change in the HF aperture during production -- which is affected by the various BHP management options and the associated production strategies -- and its effect on the HF conductivity and performance.
- To conduct a sensitivity analysis that involves a wide range of geomechanical parameters of fracture and matrix in an effort to determine their relative importance and assess the impact of geomechanics on the production and reservoir performance during the depletion of the reservoir.
- To propose a general methodology (much wider than that proposed for the reservoir of interest) that identifies the key parameters that define optimal

production management strategies tailored to the specifics of individual reservoirs and well completions.

1.3 Research Approach

This is a numerical study that was based on the analysis of coupled multiphase flow and 3D geomechanics in hydraulically fractured tight/shale reservoirs. I investigated different drawdown management strategies, I evaluated them using various criteria (such as the EUR) and I conducted an optimization analysis of the corresponding production process. The activities that were necessary to achieve the work objectives are discussed in the following sections.

1.3.1 Analysis of Historical Production Data

Using historical field production data, I first attempted to determine the correlation of production performance and key well and operation parameters during both the early production stage and later production. In the next step, I used the commercial software Kappa Topaze (Kappa Engineering, 2018) to conduct a Rate Transient Analysis (RTA) using the "log-log" plot and the "Blasingame" plot for a multi-fracture horizontal well with variable wellbore storage and time-dependent skin factor. RTA methods were used to estimate the reservoir and completion properties — including the fracture conductivity, the fracture half-length and the reservoir permeability, all of which were crucially important inputs in the numerical simulation studies that followed.

1.3.2 Development of Coupled Flow and Geomechanics Simulator

I developed a fully implicit, non-isothermal three-phase, three component compositional simulator of flow and transport of fluids and heat in porous and fractured media to estimate production from the multi-fractured horizontal wells in the reservoir of interest. I then coupled the flow simulator with a pre-existing, validated 3D geomechanical model in order to investigate the fracture evolution during production under different drawdown strategies. The geomechanical simulator uses the fixed-stress split method, which is unconditionally stable in a sequential implicit scheme. The coupled simulators provided two-way coupling between geomechanics and the flow and transport of fluids and heat, in which changes in the flow parameters and conditions affect the geomechanics and changes in the geomechanical properties affect the flow parameters.

1.3.3 Evaluation of Alternative Production Management Options

In this numerical simulation study, I investigated the effects of different drawdown strategies, BHP drawdown rate, total pressure drawdown, and production duration on the production performance. In addition, I monitored and analyzed the evolution of the associated time-dependent conditions and parameters, including the pressure, the fracture porosity, the fracture permeability, the volumetric strain and the displacements. The cumulative oil production is the main criterion for the comparison of the various options.

1.3.4 Sensitivity Analysis Studies

Following the evaluation of alternative production management options, I conducted a sensitivity analysis to determine the relative impact of variations in the geomechanical parameters on the production performance. Here, I investigated the sensitivity of production to the Young's modulus of elasticity, the Poisson's ratio and the Biot coefficients of both matrix and fracture.

1.3.5 Optimization Studies

Combining all the analyses discussed in Sections 1.3.3 and 1.3.4, I proposed an optimal methodology to achieve the desirable objective of maximal oil recovery.

1.4 Production Analysis

In this activity, I conducted an RTA of each well to explore the uncertainty ranges of many important flow-related parameters with the help of the commercial software Kappa Topaze. The major steps are summarized as follows: I first used the Prosper software to calculate the bottomhole pressure based on the available data on the PVT properties of the oil, the completion diagram and geometry and the well deviation, perforation, and wellbore geometry. I then uploaded the oil production rate and pressure to Kappa and extracted the uploaded historical data within the specified time interval. Next, I used both the Blasingame plot and the log-log plot for data diagnosis and selected a standard analytical model for a multi-fractured horizontal well (vertical hydraulic fracture) to conduct the analysis and interpretation in the software. To minimize the regression errors between the observed and the calculated data of the BHP and of the fluid production rates, I invoked the optimization tool in the software. Through this history matching process, I developed a better understanding of the uncertainty of the ranges in the values of the target variables. I used these value ranges as the starting points in the ensuing simulations, which determined the optimal parameters that yielded a good match of predicted and observed oil rates and bottomhole pressures.

1.5 Numerical Simulation

In this activity, I used the knowledge and the parameter values acquired from the RTA to construct a representative numerical simulation model accordingly. As discussed earlier, the simulation process involves the two-way coupling of the flow simulator and the geomechanics simulator.

I used the coupled flow and geomechanics simulator to study the effects of different production management scenarios on the production performance. First, I investigated various drawdown strategies, including the cases of (a) a stepwise declining BHP, (b) a linearly declining BHP and (c) a constant BHP. Moreover, I investigated the effects of total pressure drawdown, the BHP ramp-down duration and the variable declining rate of BHP are illustrated. Finally, I proposed an optimal strategy for long-term production.

In addition, I conducted sensitivity analyses of the effects of several geomechanical parameters on the production performance. The parameters I considered were the Young's modulus of elasticity, the Poisson's ratio and the Biot coefficient of both the matrix and the hydraulic fracture, and provided an insight into the impact of geomechanics parameters on the reservoir production performance (as quantified by the cumulative oil production) over a 3-year period.

CHAPTER II

LITERATURE REVIEW

This chapter reviews the current developments in time-rate analysis, followed by discussions on the coupled simulation of multiphase flow and geomechanics and on current strategies of production drawdown management.

2.1 Rate Transient Analysis (RTA)

Rate transient analysis (RTA), known as "modern" decline curve analysis as this methodology employs the time, rate, and pressure histories, as well as a specified reservoir model. RTA is a standard practice and plays a vital role in understanding the flow and production of fluids in a reservoir. RTA is the process of analyzing "time-rate-pressure" data where it is anticipated that transient flow features are observed, so that reservoir properties can be estimated. This is analogous to pressure transient analysis of a single shut-in sequence, but in the case of RTA the entire production data set is used. The major benefit of RTA methods is that the well does not have to be shut-in for testing (as is the case in pressure transient analysis), but the entire data sequence is used for diagnostics and analysis. This being the case, RTA emerges as a cost-efficient and powerful tool to take advantage of large volumes of data and improve the accuracy of prediction of the reserves and the characterization of the well-reservoir system.

Many researchers have proposed different RTA methods, thus making significant contributions to the development and improvement of the method. Among the earlier researchers, Blasingame and Lee (1986) presented a new RTA method of estimating the drainage area size and shape from bottomhole pressure and flow rates. Their method is even applicable to variable-rate flows in a closed reservoir but assumes that transient effects are negligible. Thus, the method is acceptable for cases of single-phase flow in systems with low compressibility. Blasingame *et al.* (1989) proposed new type curves and type curve plotting functions using the integration rather than differentiation of well test data, which yield a smoother function match for noisy data.

The RTA method of Blasingame *et al.* (1991), in addition to being able estimate reservoir properties during transient flow, uses a superposition function based on boundary-dominated flow that permits the reservoir volume to be estimated from variable-rate and/or variable pressure production. This method provides accurate results during both boundary-dominated flow and transient flow. Palacio and Blasingame (1993) presented a new method of production data analysis for the case of single-phase flow of oil or gas using type curve analysis. By using plots of the flow rate integral and the flow rate integral derivative functions vs. the material balance time, they were able to obtain a consistently accurate match with decline type curves. In their RTA method, the normalized rate $\frac{q(t)}{p_i - p_w(t)}$, the normalized rate integral $\frac{1}{t_e}\int_0^{t_e}\frac{q(t)}{p_i - p_w(t)}dt$ and the normalized rate integral derivative $\frac{\partial}{\partial \ln(t_e)}\left(\frac{1}{t_e}\int_0^{t_e}\frac{q(t)}{p_i - p_w(t)}dt\right)$ vs. the material balance time are shown on log-log scale plots, in which the boundary-dominated flow exhibits a negative unit slope line. Additionally, in a log-log plot of $\frac{p_i - p_w(t)}{q(t)}$ versus $t_e = \frac{Q(t)}{q(t)}$, the boundary-dominated flow is identified by a unit slope line.

Valkó (2009) presented the stretched-exponential decline (SEPD) model and this approach has two advantages. Most importantly, it is applicable to both transient and boundary dominated flow behavior. Beyond that, the SEPD model yields a finite EUR prediction regardless of total production time. Additionally, the SEPD has only 3 parameters to tune as shown below.

$$q_w(t) = q_i \cdot \exp\left[-\left[\frac{t}{\tau_v} \right]^{n_v} \right]$$

where, q_i is the initial (or maximum) production rate, t is the production time, τ_v is the characteristic production time, and n_v is the time exponent (dimensionless). One needs to conduct history matching and determine the values of q_i, τ_v, and n_v iteratively. Later, Valkó and Lee (2010) extended the SEPD model for EUR prediction.

The "Duong" model (Duong, 2011) is an empirical method designed for fracture dominant flow without a substantial contribution from the matrix. The Duong rate-time relation can is given as

$$q_w(t) = q_i \cdot t^{-m_{dg}} e^{\frac{a_{dg}}{1-m_{dg}}\left(t^{1-m_{dg}}-1\right)} + q_\infty$$

where, m_{dg} and a_{dg} are the slope (dimensionless) and intercept (inverse time) respectively, of the data when a straight-line trend is evident on a log-log plot of rate/cumulative production versus time. In addition, q_∞ is the rate at infinite production time. There is no limitation on q_∞, which can be positive, zero, or even negative, while m_{dg} is always positive: $m_{dg} < 1$ may indicate a conventional tight well and $m_{dg} > 1$ typically corresponds to shales. The Duong method implicitly assumes a growing drainage volume and thus it never reaches boundary dominated flow. Therefore, it tends to overestimate EUR unless extra constraints are employed to account for boundary effect.

Unlike above-mentioned RTA methods that honors 3-D fluid flow and production data, other researchers tried to simplify the geometry first before conducting analysis. King et al. (2016) and Wang et al. (2017) developed a semi-analytical (asymptotic) approach which utilizes a geometric approximation of dynamic drainage volume to relate the production rates of a well to its flowing bottomhole pressure. These authors managed to map the 3-D diffusivity equation in space into a new 1-D coordinate named diffusive time of flight (DTOF), from which semi-analytical pressure and rate expressions can be easily derived. Their approach leads to a convenient way to connect transient drainage volume with production history, making it possible to first inversely interpret the formation & facture properties along the DTOF coordinate system with historical data and then conduct EUR predictions with the tuned model (Wang et al. 2018, 2019). This method successfully takes formation heterogeneity and well interference into consideration, which may be challenging for many RTA approaches, however, it suffers from limitations such as multiphase flow, just like other analytical approaches (Wang 2018).

2.2 Numerical Simulation

Coupled flow and geomechanics simulation can play an important role in reservoir production, and a critical role in unconventional (such as shale oil) reservoirs where hydraulic fracturing is the only process that makes commercially viable production possible. Reservoir geomechanics has recently become an important research area in reservoir engineering, as it can provide information to optimize field development strategies, as wells as to provide better understanding of subsidence, wellbore stability, stress state changes and rock failures (Zoback, 2010). According to Terzaghi (1939), pore pressure changes cause changes in the effective stresses in a reservoir, which can result in reservoir rock deformation.

Reservoir compaction can enhance the oil reservoir pressure and, thus, slow the decline in the reservoir pressure. However, it can also lead to severe damage because of subsidence, which can adversely affect the permeability of the original reservoir system and the well structural integrity. Production results in a lower pore pressure and a larger effective stress, which can lead to compaction of the reservoir and land subsidence. Land subsidence in response to hydrocarbon production from petroleum reservoirs has been reported as a problem as early as in 1939 (Allen, 1972). In conclusion, consideration of geomechanics in unconventional (tight sand and shale oil) reservoirs is vital for well stimulation processes, long-term production, and environmental impact.

Addressing the interdependence of flow and geomechanics requires the solution of the coupled flow and geomechanical constitutive equations. In practical terms, this means that the simulator describing this type of problem need to have the capability to solve the coupled equations of flow (mass balance) and equilibrium geomechanics. These equations can be solved simultaneously in fully implicit schemes (resulting in very large matrices that are impractical) or sequentially (far more manageable). In sequential coupling, one of the several variants of Finite-Difference (Burstein *et al.*) methods are routinely used for the solution of the flow equations, and the geomechanical equations are almost invariably solved by a Finite Element (FE) method.

Coupled flow and geomechanics have been investigated by many scholars. Settari and Mourits (1994) developed an approach to couple commercial software solving the flow equation with a geomechanical code using an iterative coupled approach with porosity correction. Settari and Walters (2001) proposed several different methods to combine poroelastic geomechanical models with models of flow through porous media, such as explicitly coupled, iteratively coupled and fully coupled techniques. Fully coupled and sequentially coupled methods are commonly used in most practical applications. Fully-coupled method solve simultaneously the flow and the geomechanical equations at each timestep, resulting in a single, very large matrix equation that is solved through the Newton-Raphson method in the fully-implicit formulation of the problem. The advantages of the fully coupled approach are the unconditional stability of the solution and the preservation of second-order convergence of the nonlinear iterations. The drawback of the fully coupled approach is the high computational demand and, consequently, the considerably longer execution times compared to other coupled methods solving the same problem.

Sequentially coupled methods solve either the flow or the geomechanical equation first, and then separately the other (remaining) equation. This procedure involves iteration at each time step until the solutions to both equations converge within an acceptable criterion. Note that the domain of the geomechanical problem is usually larger than that of the flow problem because of the need to account for the large stress and strain fields of the overburden and underburden of the petroleum reservoirs that have a pronounced effect on the system behavior. The advantage of the sequential method is that coupling the flow and the geomechanics simulators is a rather straightforward process. In addition to these widely applied coupling techniques, the explicitly coupled method computes the flows at each timestep but solves the geomechanical problems at selected timesteps only. This approach provides a fast solution, in addition to being easy to implement as the coupling of the flow and the geomechanics simulators is weak and straightforward, but the solutions may suffer from instability, in addition to potentially significant mass balance errors.

Gutierrez *et al.* (2001) discussed the interaction between multiphase flow and rock deformation in a fully coupled system, and showed that the reservoir deformation could affect the permeability and the compressibility of the rock. Their fully implicit model of coupled flow and geomechanics used displacements and pressure as the primary variables, but could suffer from numerical instability caused by the compressibility values used in the reservoir simulation.

Dean *et al.* (2006) compared several coupling methods, including the explicitly coupled, iteratively coupled and fully coupled techniques. They reported that the iteratively coupled techniques produce similar results with the other methods if the tolerance for the nonlinear iterations is sufficiently tight, and that the explicitly coupled technique yields results similar to those from the two other methods if the timestep is sufficiently small.

Kim *et al.* (2009) conducted a conclusive study presenting the sequential solution method for coupled flow and geomechanics. They compared four sequential coupling methods in detail: drained, undrained, fixed-strain and fixed-stress splits. The stability, accuracy and efficiency of these sequential methods were analyzed. Their results showed that the drained and the fixed-strain split methods under certain conditions converged to the wrong solution, and that the fixed-stress method was generally more accurate than the undrained method. Thus, they strongly recommended the fixed-stress method.

Kim *et al.* (2012) developed a two-way coupling method between the fluid flow and geomechanics. In their process, the solutions of mechanics were reflected in the flow problem solutions. Rutqvist and Moridis (2007) presented an one-way coupling of fluid flow, heat transfer and geomechanics, with the change of fluid pressure and temperature affecting geomechanics. The difference of one-way and two-way coupling is the feedback from geomechanics to fluid flow.

Kim and Moridis (2014) performed numerical simulation studies of coupled flow and geomechanics in shale- and tight-gas reservoirs, which considered the interdependence of variations in porosity, permeability and pore volume, and those in the stresses, strains and displacements . Their results showed that it was essential to use tightly coupled flow and geomechanical models when the uncoupled (or flow-only) simulation approach cannot capture the reservoir behavior accurately during production from tight- and shale-gas reservoirs.

Ashida *et al.* (2017) employed the coupled flow and geomechanical simulator TOUGH-FLAC to conduct studies on the effects of the depletion-induced reservoir compaction on production. An alternative approach in this study was the use of the volumetric strain to the mass balance by correcting the rock compressibility in the fluid simulator. They suggested that changes in the porosity and permeability due to reservoir compaction should be considered for optimal reservoir management.

Liu *et al.* (2020) developed an implicit, sequentially-coupled flow and geomechanics simulator incorporating a discrete fracture model to model fluid distribution and recovery performance from ultra-low permeability reservoirs, where the results of such simulations can provide insight on the stimulated fracture volume, water invasion zone size, and the fracture treatment design.

To summarize, numerical studies on coupled flow and geomechanics are essential to model the production performance with geomechanical effects acting on the fractures and rock matrix of unconventional, ultra-low permeability reservoirs.

2.3 Production Drawdown Management

Productivity loss in unconventional reservoirs is often attributed to geomechanics-related factors, such as reduction in the hydraulic fracture aperture caused by proppant crushing or a decrease in the matrix and proppant-filled HF permeability because of increasing vertical and/or horizontal stresses during production-induced pressure depletion (Wilson, 2015). Analyses of data from horizontal wells in the Vaca Muerta Shale provided evidence that aggressive choke management may cause a reduction in EUR of up to 20% (Rojas and Lerza, 2018). To investigate the stress change and fracture evolution during production-induced pressure depletion, the use of coupled flow and geomechanics models is essential. Kumar *et al.* (2018) used their fully coupled geomechanical reservoir model to report that (a) a conservative drawdown strategy can maintain the fracture conductivity for a longer period and (b) an aggressive drawdown strategy results in higher initial production rates but leads to faster fracture closure. Using multiply-fractured horizontal wells, Okouma-Mangha *et al.* (2011) proposed two permeability decay functions and indicated that a low drawdown yields a higher recovery, thus showing that rate restriction is a mitigating factor in decreasing well productivity.

In this study, a sequentially coupled flow and geomechanics model is used for the study and analysis of production management. In the coupled simulator, the porosity and permeability for the matrix and the fracture, as well as the fracture volume and all the geomechanical variables (stresses, strains and displacements) are dynamically updated.

CHAPTER III

RATE TRANSIENT ANALYSIS

3.1 Diagnostic Plots Analysis

3.1.1 Field Overview and Reservoir Description

The production data used in this work originate from a well in the SCOOP/STACK play in Oklahoma (USA). The Meramec and Osage are the two main prolific reservoirs. The play studied in this research lies within the Meramec unit, which comprise argillaceous and calcareous siltstones.

The initial reservoir pressure is 38 MPa (or 5,565 psia) and the bubblepoint pressure is 35 MPa (or 5,053 psia). The reservoir temperature is 90 ^{o}C (or 165 ^{o}F). The porosity average is around 3% and the permeability is in the 10^{-19}~10^{-17} m^2 (0.1~10 μd) range. The condensate gas-oil ratio is 511 m^3/m^3 (2,867 scf/bbl).

The measured depth (MD) and vertical true depth (TVD) of the hydraulic fractured horizontal "Well A" are 4376 m (14,358 ft) and 2898 m (9,508 ft). The well has 15 hydraulic fracture treatment stages with 4 perforation clusters per stage and the average perforation cluster spacing is 22.86 m (75 ft). The production history for this well lasts at the time of analysis was 1400 days and includes good/very good quality production data (rates and pressures).

3.1.2 BHP Calculation

Bottomhole pressure measurement during field production is costly and difficult, so only "spot pressure" and/or temporary bottomhole pressure measurements were obtained by the operator. Therefore, the industry standard software PROSPER was used to estimate bottomhole pressure from wellhead pressure, flowrates, and the wellbore configuration.

Historically, there has been considerable effort in the petroleum industry to calculate pressure drop behavior for multiphase flow in wellbores and pipelines. Most pertinent to this work, the selection of the most appropriate correlation is essential for the accurate calculation of bottomhole pressure.

The correlation presented by Duns and Ros (1963) was a result of an extensive laboratory study, in which the liquid holdup and pressure gradients were measured. This correlation performs well in "mist" flow regime and it can be used in production with high GOR.

Hagedorn-Brown (1977) developed the tubing correlation after hundreds of tests in an experimental well and the essence of the method is a correlation for liquid holdup. However, this method under-predicts vertical liquid performance at low flowrates. Note that performance in condensate and mist flow systems cannot be predicted well by the Hagedorn-Brown method. In addition, significant errors have been observed for cases of large bore deviated wells.

Beggs and Brill (1973) proposed a correlation used in both horizontal and inclined flow, but many practitioners suggest that this method tends to over-predict pressure drop in vertical and deviated wells.

In this work the "PROSPER" software (2018) was used, and in particular, the "PETEX-2" (or Petroleum Experts 2) correlation was selected as it combines the best features of the previous correlations and uses different correlations for separate flow regimes: For example, it uses the Wallis and Griffith correlation for bubble flow, the Hagedorn-Brown correlation for slug flow, and the Duns and Ros correlation for transition and mist flow regimes. For the PETEX-2 model, numerous experiments with high flowrates were conducted and the results were generally very good to excellent. Another correlation is the "PETEX-5" (or Petroleum Experts 5) model, which is said to be capable of modeling any fluid type for different types of well and trajectory.

For this work we selected the PETEX-5 (or Petroleum Experts 5) model as the tubing correlation to calculate the bottomhole pressure (or BHP) profile. The steps to calculate the BHP using this software are as follows:

- First, I built the black oil model and used as inputs the PVT data and gas-lift data provided by the operator and shown in **Tables 3.1** and **3.2**.

Table 3.1 PVT Input Data

Parameters	Values
Fluid Model	Black Oil
Oil Gravity	40.1
Mole percent H_2S	0
Mole percent CO_2	0.0019
Mole percent N_2	0.009
Pb, Rs, Bo Correlation	Vazquez-Beggs
Oil Viscosity Correlation	Petrosky et al

Table 3.2 Gas-lift Input Data

Parameters	Values
Gas Lift Type	Valve Depths Specified
Gas Lift Method	No Friction Loss in Annulus
Gas Rate Method	Use Injected Gas Rate
Gas-lift Gas Gravity	0.66
Injected Gas Rate	0.6 MMscf/day
Dp Across Valve	100 psi
Depth Valve, ft	2166, 2853, 3410, 3967, 4522, 5080, 5637, 6195, 6720, 7246

- Second, I entered as inputs the equipment data, including the deviation survey, downhole equipment, and average heat capacities, shown in **Tables 3.3** and **3.4**.

Table 3.3 Downhole Equipment

Type	Xmas Tree	Casing	Casing	Casing	Casing	Casing	Casing	Tubing
Measured Depth, ft	0	8042	8952	9046	9077	9281	9308	9593

	Inside Diameter, inches	Inside Roughness, inches
Casing	4.67	0.0006
Tubing	2.441	0.0006

Table 3.4 Average Heat Capacities

Parameters	Values
Cp oil, btu/lb/F	0.53
Cp gas, btu/lb/F	0.51
Cp water, btu/lb/F	1

- Third, I entered as inputs the following data: liquid rate, wellhead pressure and temperature, gas oil ratio, water cut and gaslift gas rate. The tubing correlation was provided by Petroleum Expert 5. Bottomhole pressure is then be calculated based on the given conditions shown in **Figure 3.1**.

I validated this method as a reliable and effective approach to calculate the BHP by comparing the calculated BHP to the measured BHP from the field data of a single well, shown in **Figure 3.2**. In **Figure 3.2**, he bottomhole gauge pressure is given by the black line and the red symbols are the values calculated from the PETEX-5 BHP model. Given this performance, we believe that the PETEX-5 BHP model is appropriate for applications in this work.

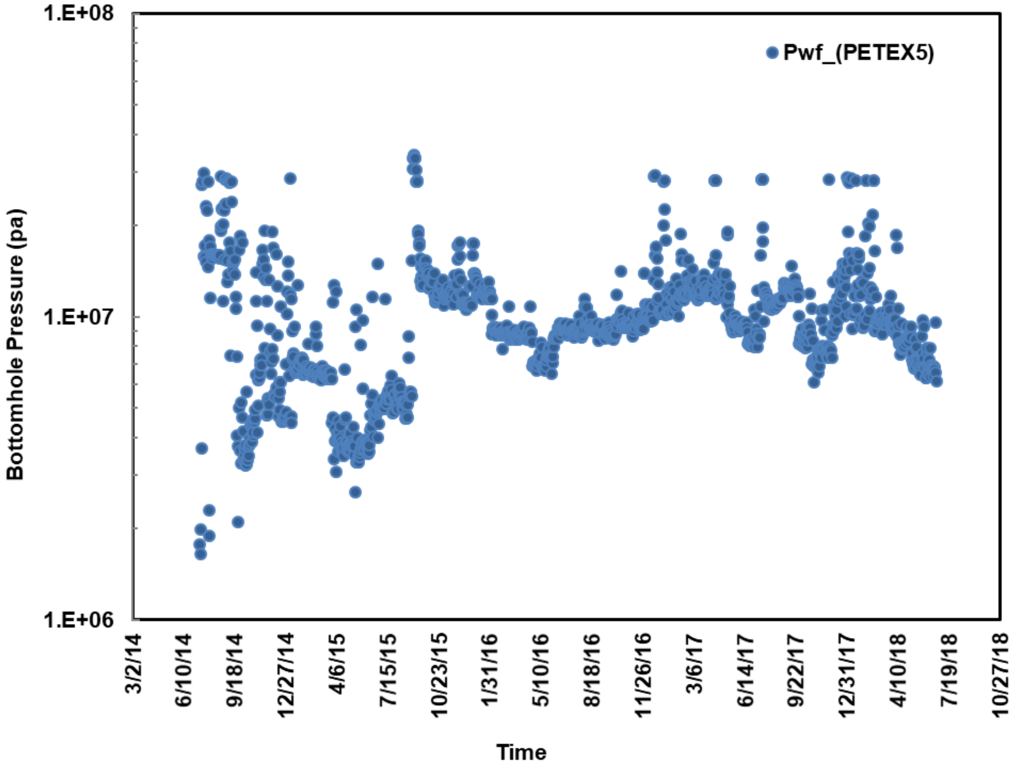

Figure 3.1 BHP Calculation Result of Well A

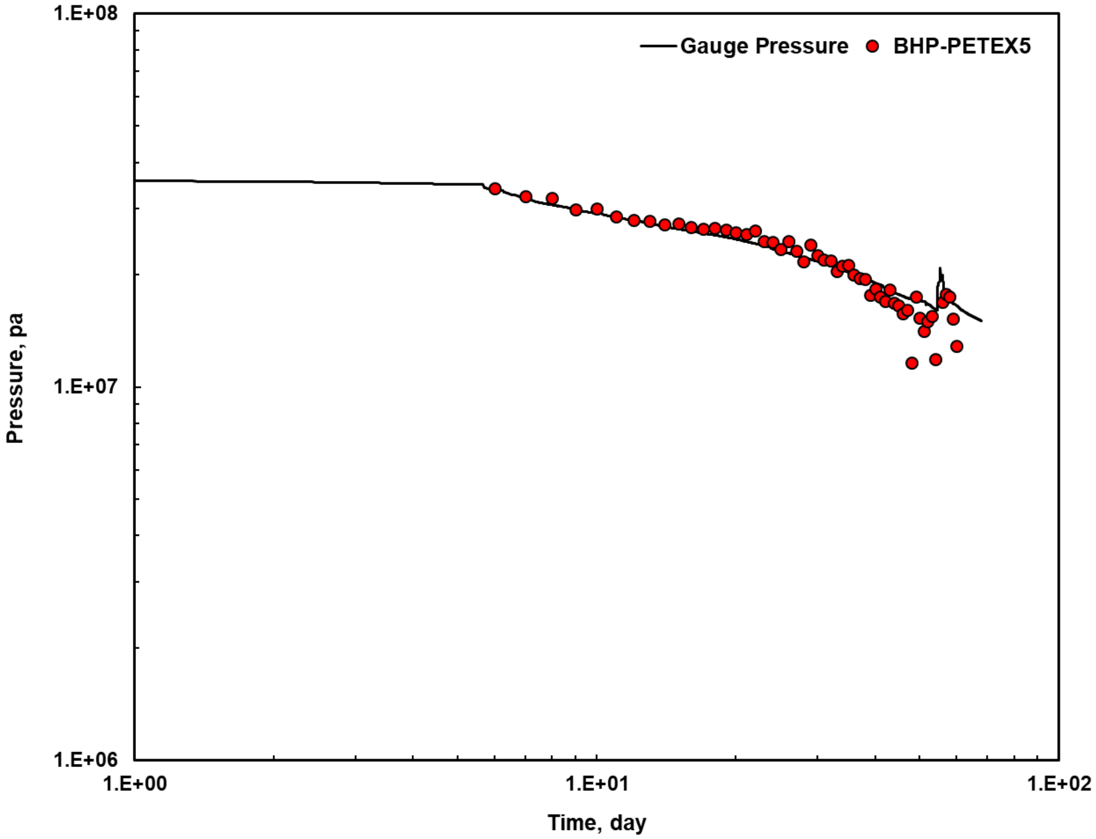

Figure 3.2 Comparison Between Measured and Calculated BHP of Well B

3.1.3 Historical Data and Diagnostic Plots

Figure 3.3 displays the production rates of oil, gas and water, the choke setting, and the calculated bottomhole pressure at t_{total} = 1400 days production for "Well A." Based on the source of the data, we believe that the oil, water, and gas flowrates have sufficient accuracy for the application of advanced analysis and interpretation techniques, as well as high-resolution reservoir modelling.

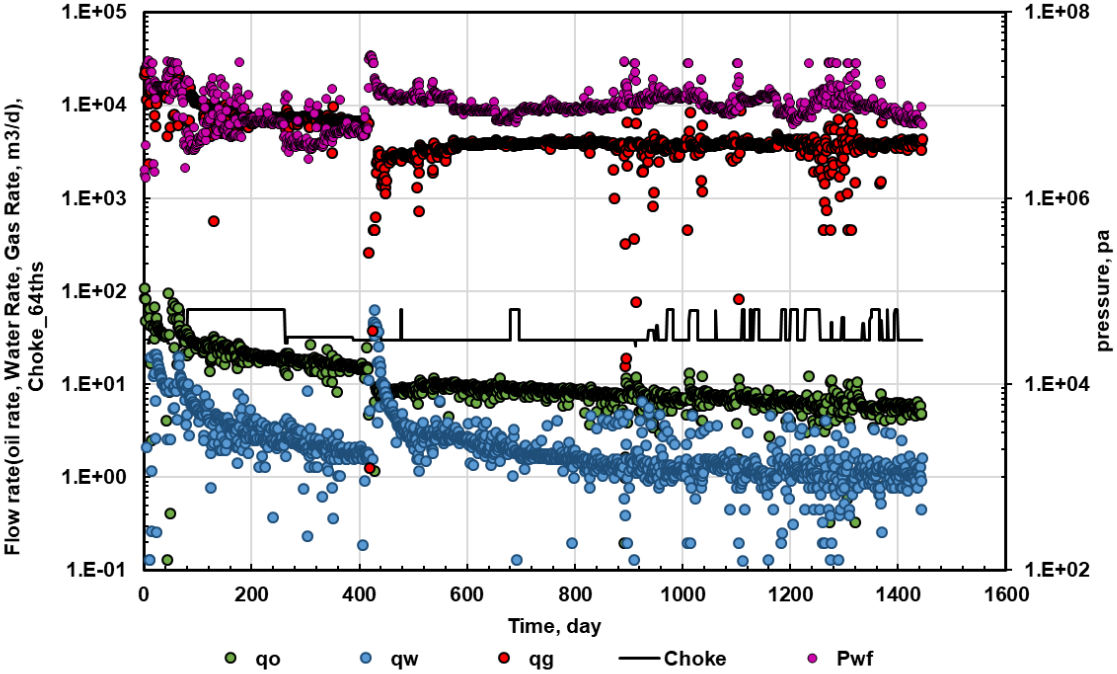

Figure 3.3 History Production of Well A: Production Rates of Oil, Water, Gas, BHP, and Choke Setting.

The gas oil ratio (GOR) corresponding to **Figure 3.3** are plotted in **Figure 3.4**. We can observe the GOR range is above 178 m^3/m^3 (1000 scf/stb), which is considered as the volatile oils.

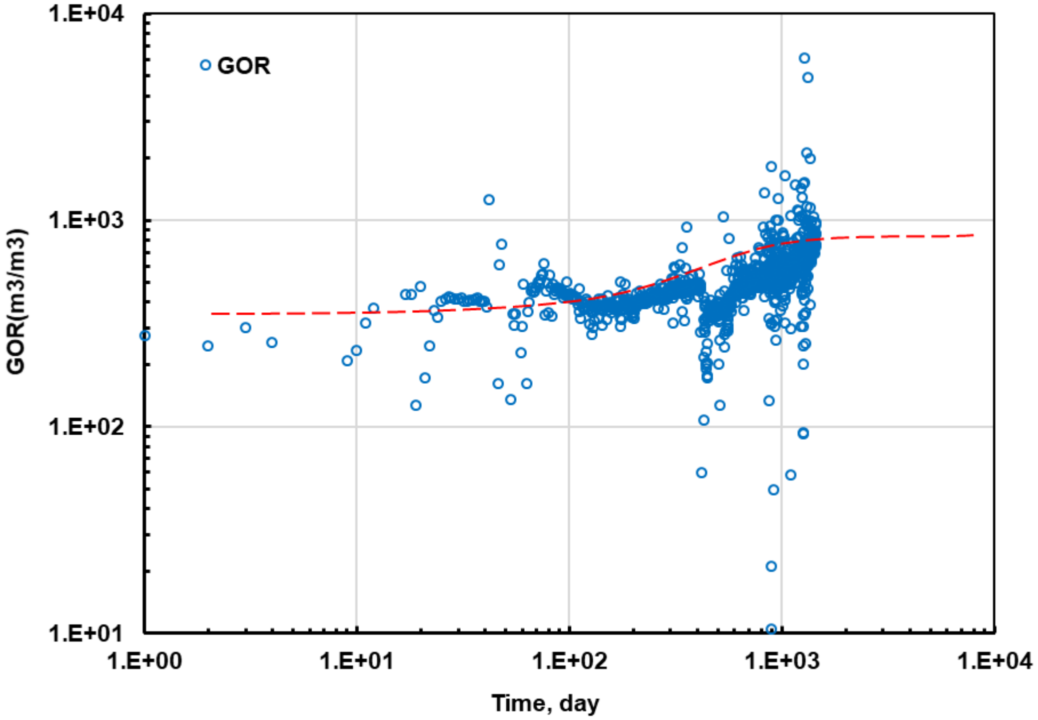

Figure 3.4 Evolution of GOR function Over Time for the System Described in Figure 3.3

The production index is calculated using the formula below (Lee *et al*., 2003)

$$J = \frac{q_{\text{total}}}{p_i - p_{wf}} \quad\text{.......}(3.1)$$

J is the production index. p_i is the initial reservoir pressure. p_i is the flowing bottomhole pressure. q_{total} is the total rate of oil, water and gas.

The log-log production index plot in **Figure 3.5** exhibits a clear and stable linear flow trend (-1/2 slope line) beginning at t = 200 days of production.

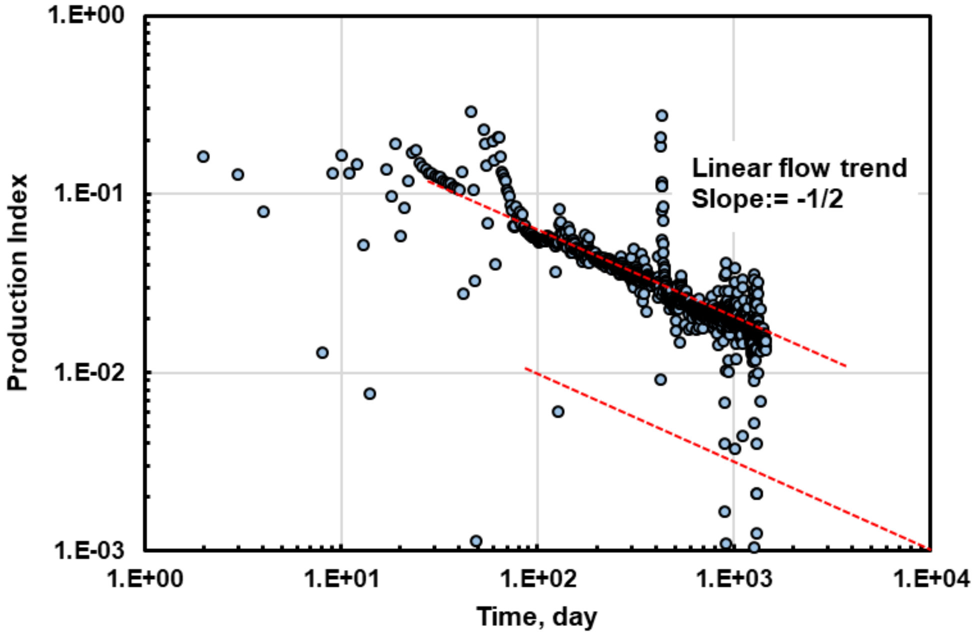

Figure 3.5 Production Index Versus Production Time for the System Described in Figures 3.3 and 3.4

3.2 Rate Transient Analysis

Kappa Topaze (Houze *et al*., 2015) is the basic tool I used to analyze the field production data via RTA. RTA is a tool that maximizes the information that can be deduced from the production data, including the estimation of the formation permeability, of the fracture properties (fracture half-length and fracture conductivity), and of the pressure-dependent properties reservoir (permeability and porosity). The original production history of the well shown in **Figure 3.3** was used as the input data for the RTA analysis. More precisely, I used the estimated BHP and oil rate for the analysis — the pressure range was 1.655 - 35 MPa (240 - 4942 psi); the oil production rate began at $1.28\text{x}10^{-3}$ m^3/s (696 STB/D) and decreased all the way to $5.686\text{x}10^{-5}$ m^3/s

(30.9 STB/D) at the end of the production period. Topaze automatically calculated the cumulative oil production associated with the oil production rate.

The analytical model used in RTA includes: (a) a horizontal fractured well model; (b) homogeneous reservoir condition; (c) infinite boundary case; (d) uniform flux fracture; (e) time-dependent skin values.

In conducting the RTA, I selected the time interval for the data analysis, *i.e.*, the period that is sufficiently representative of the production behavior over the majority of the production period. And I did an iterative history-matching process, in which the reasonable ranges of skins, number of fractures, fracture length and height, and reservoir permeability should be set. By running the optimization tool in Topaze software, we obtain the optimized parameters that has the minimal deviations between observations and model predictions.

Figure 3.6 shows the oil rate, the cumulative oil production and the flowing BHP data originating both from the production history and generated by the history-matching with the analytical model in Topaze. In general, there is a good match between the field data and the analytical model predictions.

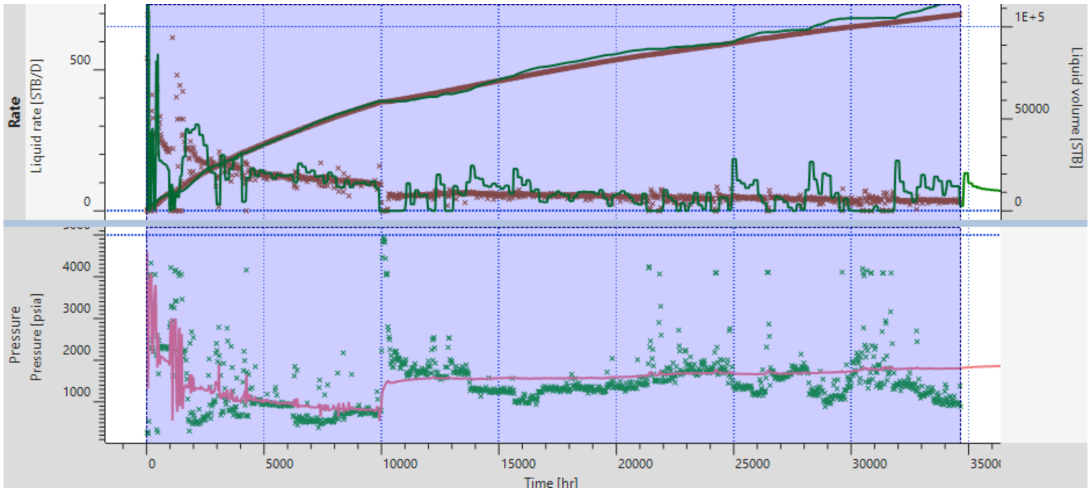

Figure 3.6 Rate and Pressure Matching Plots Corresponding to the System Described in Figures 3.1 to 3.3.

Figure 3.7 shows the log-log plot of pressure drop and pressure drop derivative from observation data (markers) and analytical model (curves) versus time. The matches of pressure drop and pressure drop derivative between calculated data and the history data for the entire production period are good.

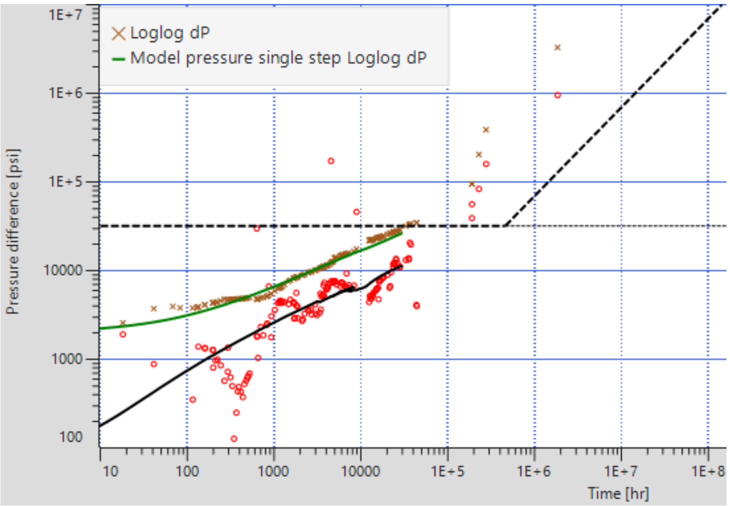

Figure 3.7 Log-log Plot of Rate Transient Analysis: Pressure Drop, Pressure Drop Derivative of History and Calculated Data

Figure 3.8 presents the Blasingame plot of the productivity index, the productivity index integral function, and the productivity index integral derivative function using observation data (markers) and the analytical model (curves) versus material balance time. Overall, the matches of these observed productivity index functions and the model predictions are good. Because of unstable flow behavior during early production times, we observe a mismatch between observations and model predictions at early production times.

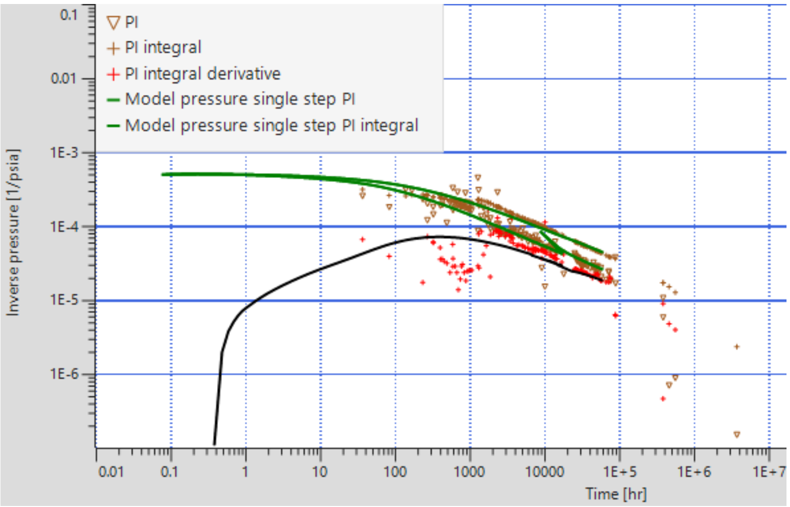

Figure 3.8 Blasingame Plot of Rate Transient Analysis: Pressure Integral, Pressure Integral Derivative of History and Calculated Data

Table 3.5 summarizes the reservoir and fracture parameters that were deduced from the time-rate transient analysis, in which the reservoir permeability, fracture geometry and time-dependent skin values are the reference for the numerical simulation studies in Chapter IV.

Table 3.5 Rate Transient Analysis Result

Parameters	Values
Reservoir permeability k_m, mD	0.0007
Fracture half-length x_f, ft	300
Fracture height h_f, ft	180
Skin value s, early	0.0313
Skin value s, late	0.033

3.3 Summary and Conclusion

I conducted an RTA for Well A using a history-matching process. The relevant reservoir parameters are estimated after a successful agreement of field observations of time-rate data with the predictions of an analytical model available in the commercial software package Topaze (Kappa Engineering). The data inputs include the fluid properties, reservoir properties, and the production rates and pressures. The bottomhole pressures for this work were calculated using Prosper software (Petroleum Experts, 2018). The correlation we chose to use is "PETEX-5" (or Petroleum Experts 5), which is validated as a reliable reference through comparing the calculated BHP with the available measured BHP data **(Figure 3.2)**.

The analyzed well is a multi-fractured horizontal well in a homogeneous reservoir with and infinite reservoir boundary. Using this model in the Topaze software, I obtained optimized values for the fracture half-length, the fracture height, the reservoir permeability and the time-dependent skin.

CHAPTER IV

COUPLING FLOW AND SIMULATION

4.1 Mathematic Model

In my coupled simulation, the flow problem is solved first and it is followed by the geomechanical problem that incorporates data from the solution of the flow problem. The flow of information in the components of the coupled simulator is illustrated in the sketch of

Figure 4.1. The sequential coupling of the flow and geomechanical codes is described as follows. The fluid and heat flow problem is solved first, providing updated/current values of pressure, phase saturation and temperature. In the next step, the updated variables are imported into the geomechanics simulator to solve the stress, strain, volumetric strain and displacements at each timestep. The updated geomechanical variables (especially stresses and strains) are used to update the porosity and permeability of each element in the flow simulator according to appropriate constitutive equations. The flow equation is solved again with the updated properties, and the process is repeated.

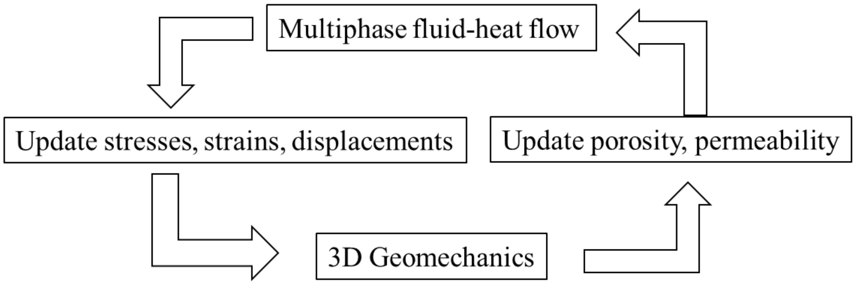

Figure 4.1 The Flowchart of Coupled Flow and Geomechanics Simulator

4.1.1 Governing Equations

The governing equations of fluid mass and heat balance can be written as (Moridis, 2014)

$$\frac{d}{dt}\int_{\Omega} m^k d\Omega + \int_{\Gamma} \mathbf{f}^k \cdot \mathbf{n} d\Gamma = \int_{\Omega} q^k d\Omega \quad \text{.......} (4.1)$$

Where k indicates the fluid component; d(.)/dt means the time derivative of a physical quantity (.); m^k is fluid mass of component k, [kg/m^3]; $\mathbf{f}^k$ is the Darcy flux vector of component k, [kg/m^2/s]; q^k is the source and sink terms on the physical domain Ω with a boundary surface Γ, and $\mathbf{n}$ is the outer normal vector of the boundary, [kg/m^3/s].

The fluid mass of component k is shown as:

$$m^k = \sum_J \phi S_J \rho_J X_J^k \quad \text{.......} (4.2)$$

Where ϕ is the porosity, [dimensionless], S_J is the saturation of phase *J*, [dimensionless], ρ_J is the density of phase *J*, [kg/m^3], X_J^k is the mass fraction of component *k* in phase *J*, [kg/kg].

The mass flux term is written as:

$$\mathbf{f}^k = \sum_J w_J^k = \sum_J X_J^k w_J \quad \text{.......} (4.3)$$

And the flux term is described by Darcy's law as

$$w_J = -k \frac{k_{rJ} \rho_J}{\mu_J} \left(\nabla p_J - \rho_J \mathbf{g} \right) \quad \text{.......} (4.4)$$

Where k is the rock intrinsic permeability, [m2], k_{rJ} is the relative permeability of the phase J, [dimensionless], μ_J is the viscosity of the phase J, [Pa S], p_J is the pressure of phase J, [Pa], $\mathbf{g}$ is the gravitational acceleration vector, [ms^{-2}]

The governing equation for mechanics is written as

$$\nabla \cdot \boldsymbol{\sigma} + \rho_b \mathbf{g} = 0 \quad (4.5)$$

Where $\boldsymbol{\sigma}$ is the Cauchy total-stress tensor, [Pa], ρ_b is the bulk density, [kg/m^3].

The infinitesimal transformation is assumed, such that the strain tensor ε can be expressed as the symmetric gradient of the displacement vector u , *i.e.,*

$$\varepsilon = \frac{1}{2}\left(\mathrm{Grad}^{\mathrm{T}}\mathbf{u} + \mathrm{Grad}\,\mathbf{u}\right) \quad (4.6)$$

4.1.2 Coupling and Constitutive Relations

The constitutive relation for coupled multiphase nonisothermal flow and elastoplastic geopmechanics are based on Biot (1941) and Coussy (1995, 2004), which can be written as

$$\boldsymbol{\sigma} = \boldsymbol{\sigma}' - b\mathbf{1}p = \mathbf{C} : \boldsymbol{\varepsilon} - b\mathbf{1}p - 3\alpha_T K_{dr} T\mathbf{1} \quad (4.7)$$

Where $\boldsymbol{\sigma}$ and $\boldsymbol{\sigma}'$ are the total stress tensor and effective stress tensor, respectively, [Pa]; b is the Biot coefficient, [dimensionless]; C is the elasticity tensor, [Pa]; $p = \sum_J s_J p_J$ is the fluid pressure, [Pa]; α_T is the volumetric skeleton thermal dilation coefficient, [dimensionless]; K_{dr} is the drained bulk modulus, [Pa].

The two simulators I coupled are implemented in a sequential implicit scheme for the fluid flow and heat transfer and the geomechanics. These two problems are solved by fixing one or more parameters. To solve the fluid and heat flow problem, the total strain and total stress are fixed. And the fluid pressures, temperature, saturation of each phase are fixed to solve geomechanics problem. During the calculation of flow problems, the Lagrange's porosity is employed.

The Lagrange's porosity, which is defined as the ratio of the pore volume in the deformed confirmation to the bulk volume in the initial configuration, can be expressed as (Kim *et al.*, 2012)

$$\delta\Phi = \frac{b-\phi}{K_s}\sum S_J \delta p_J + b\delta\varepsilon_v \text{ ......} \quad (4.8)$$

Where Φ is the Lagrange porosity, [dimensionless]; ε_v is the volumetric strain, [dimensionless]; S_J is the saturation of phase *J*, [dimensionless]; p_J is the fluid pressure of phase *J*, [Pa].

From **Eq. 4.8**, we can find the coupling relation between the fluid flow and geomechanics it is obvious that the volume change cannot be ignored. To accurately describe the system behavior, two-way coupling is necessary to be applied (Kim *et al.*, 2012). Following the fixed stress split method, the flow problem is solved first to obtain pressure by fixing the total stress, i.e. $\delta\sigma_v = 0$. Thus, combing **Eq. 4.8** and the constraint $\delta\sigma_v = 0$ under the backward Euler method yields

$$\Phi^{n+1} - \Phi^n = \left[\frac{b-\phi}{K_s} + \frac{b^2}{K_{dr}}\right]\sum S_J\left(p_J^{n+1} - p_J^n\right) + 3\alpha_T b\left(T^{n+1} - T^n\right) - \Delta\Phi_c \text{ ......} \quad (4.9)$$

$$\Delta\Phi_c = \frac{b^2}{K_{dr}} \sum S_J \left(p_J^n - p_J^{n+1} \right) + 3\alpha_T b \left(T^n - T^{n+1} \right) - b \left(\varepsilon_v^n - \varepsilon_v^{n-1} \right) \quad \text{.................................} (4.10)$$

where $\Delta\Phi_c$ is the porosity correction term, [dimensionless]; K_{dr} is the drained bulk moduli, [Pa].

Note that the computation cost for one-way and two-way coupling are almost the same, the difference of them are the Lagrange's porosity correction term, which can be negligible compared to the global computation (Kim *et al.*, 2012).

4.1.3 Dynamic Permeability Method

The permeability of the matrix and of the proppant-filled hydraulic fractures are affected by the deformation of the reservoir and its components. The permeability-porosity is provided by (Rutqvist and Tsang, 2002) as:

$$k = k_0 \exp\left[c \left(\frac{\phi}{\phi_0} - 1 \right) \right] \quad \text{..} (4.11)$$

where k and ϕ are the permeability and porosity, 0 denotes a reference state, and c is a coefficient. We use 6 for fracture domain.

To adjust the fracture permeability more accurately, it is important to consider the adjustment of the volume of the fracture-associated element as a function of the fracture aperture that changes in response to changing stresses in the HF vicinity. This is described by **Eq. 4.12** :

$$Vol = Vol \cdot \frac{d_{\mathrm{HF}}}{d_{\mathrm{HF0}}} \quad \text{..} (4.12)$$

Where d_{HF} is the current fracture aperture, [m]; d_{HF0} is the initial fracture aperture, [m]; Vol is the volume of the fracture element.

Note that the volume of the matrix-associated elements does not change in my simulation, but the effects of subsidence and compaction are reflected in the permeability change.

4.1.4 Relative Permeability Method

The relative permeability model used in this work is described by the three-phase model of (Stone, 1970) as

$$k_{rg}=\left[\frac{s_g-s_{gr}}{1.0-s_{wr}}\right]^{ng} \tag{4.13}$$

$$k_{rw}=\left[\frac{s_w-s_{wr}}{1.0-s_{wr}}\right]^{nw} \tag{4.14}$$

$$k_{ro}=\left[\frac{1.0-s_g-s_w-s_{or}}{1.0-s_g-s_{wr}-s_{or}}\right]\left[\frac{1.0-s_{wr}-s_{or}}{1.0-s_w-s_{or}}\right]\left[\frac{\left(1.0-s_g-s_{wr}-s_{or}\right)\left(1.0-s_w\right)}{\left(1.0-s_{wr}\right)}\right]^{no} \tag{4.15}$$

Where k_{ro}, k_{rw}, k_{rg} are relative permeability for oil, water and gas, [dimensionless]. s_g, s_g, s_g are the saturation of oil, water and gas, [dimensionless]; s_{or}, s_{wr}, s_{gr} are the irreducible saturation of oil, water and gas, [dimensionless]; n_o, n_w, n_g are the exponent of oil, water, gas for relative permeability model, [dimensionless].

In order to determine the effects of the different parameters in the relative permeability equations on production, in my study I varied exponent values of the three phases and irreducible saturations of water and oil in both the HF and the matrix.

4.2 The Numerical Simulator

The numerical simulator I used for this study involved the coupling of two numerical codes: a 3D flow/thermal numerical simulation code and a geomechanical numerical model. FTSim was the purpose-built fully-implicit multi-phase, multi-component compositional simulator that I developed for the description of the 3D flow and transport of fluids and heat in porous and fractured media. I validated FTSim against several analytical and numerical solutions of flow of oil, gas and water (separately or in combination) through porous and fractured media.

The 3D geomechanical simulator I used was the T+M code of Kim and Moridis (2013) based on the finite element method, which was validated with analytical solutions in Terzaghi's and Mandel's problems (Terzaghi, 1943; Abousleiman, 1996) to examine the poromechanical effects. The time discretization in both components of T+M is based on the backward Euler method.

The sequential implicit method uses the existing two simulators for the solution of the subproblems. Fixed-stress sequential scheme provides the unconditional stability and numerical convergence to solve poromechanical problems accurately. And the integrated simulator provides the two-way coupling between fluid-heat flow and geomechanics, which accurately models the evolution of the stress, strain, displacement, pore volumes and permeability during production.

4.3 The Simulation Domain

The domain in my simulations is based on the concept of "stencil", which is the “minimum repetitive element” that can accurately represent a multiple-fractured horizontal well system (Olorode *et al.*, 2013). An example of a stencil is shown in **Figure 4.2**. In my simulation, the stencil describes one-quarter of the domain associated with a single hydraulic fracture (**Figure 4.3**). The stencil-based simulation reduces significantly the grid size, thus reducing the order of the matrix equation without adversely affecting the reliability of the solution and resulting in a corresponding reduction in the execution time. To obtain the total rate and cumulative production, the rate and cumulative production for the stencil are multiplied by the number of stencils in the entire multi-fractured horizontal well system. Use of a stencil is necessary and sufficient to describe the behavior of the entire multi-fractured horizontal well system (Moridis, 2017).

The fine discretization of the stencil results in a high-resolution domain that can capture flow processes and phenomena at any scale. As shown in **Figure 4.2**, the stencil describes one-quarter of the reservoir volume between parallel horizontal wells that is associated with a single hydraulic fracture, and is sufficient because of symmetry about (a) the vertical (x,z) plane that passes by the horizontal well, (b) the vertical (x,z) plane at the midpoint between the parallel horizontal wells and (c) the vertical (y,z) plane at the midpoint between the parallel vertical HFs. The fracture half-length in the x-direction is 91 m (300 ft). The fracture height is 54 m (180 ft) and half space between two HFs is 11.5 m (37.7 ft). The half fracture width (aperture) is 1 mm.

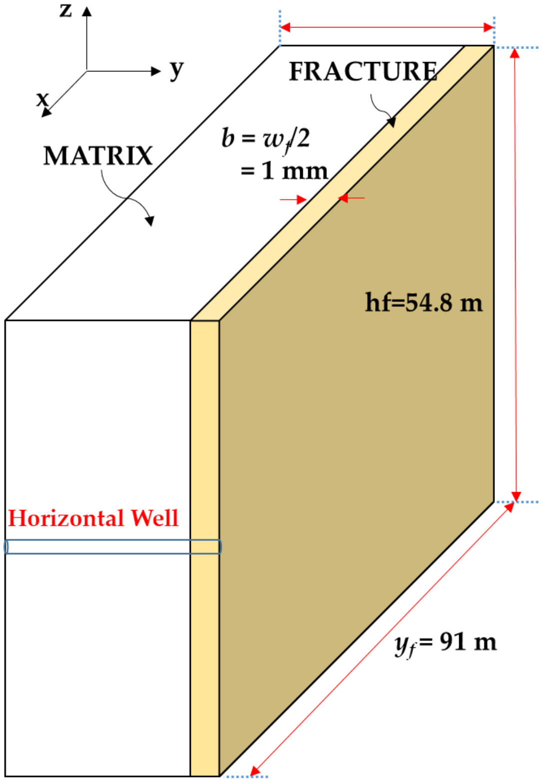

Figure 4.2 Stencils of the Systems Involving a Horizontal Well in the Reservoir

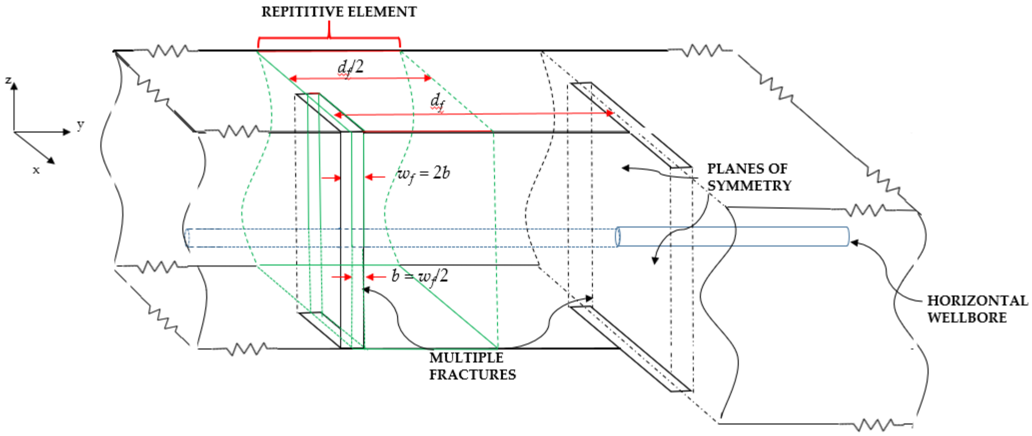

Figure 4.3 Schematic of the Stencil in Multi-fractured Horizontal Well System

The discretization of the stencil is depicted in **Figure 4.4**. The discretization is especially fine in the vicinity of the face of the HF, where elements with mm-sized Dx subdivisions are encountered. The domain is subdivided in 41514 elements in (x, y, z), resulting in a total of 166056 simultaneous equations for the solution of the flow problem. The grid block near the well and fracture are refined.

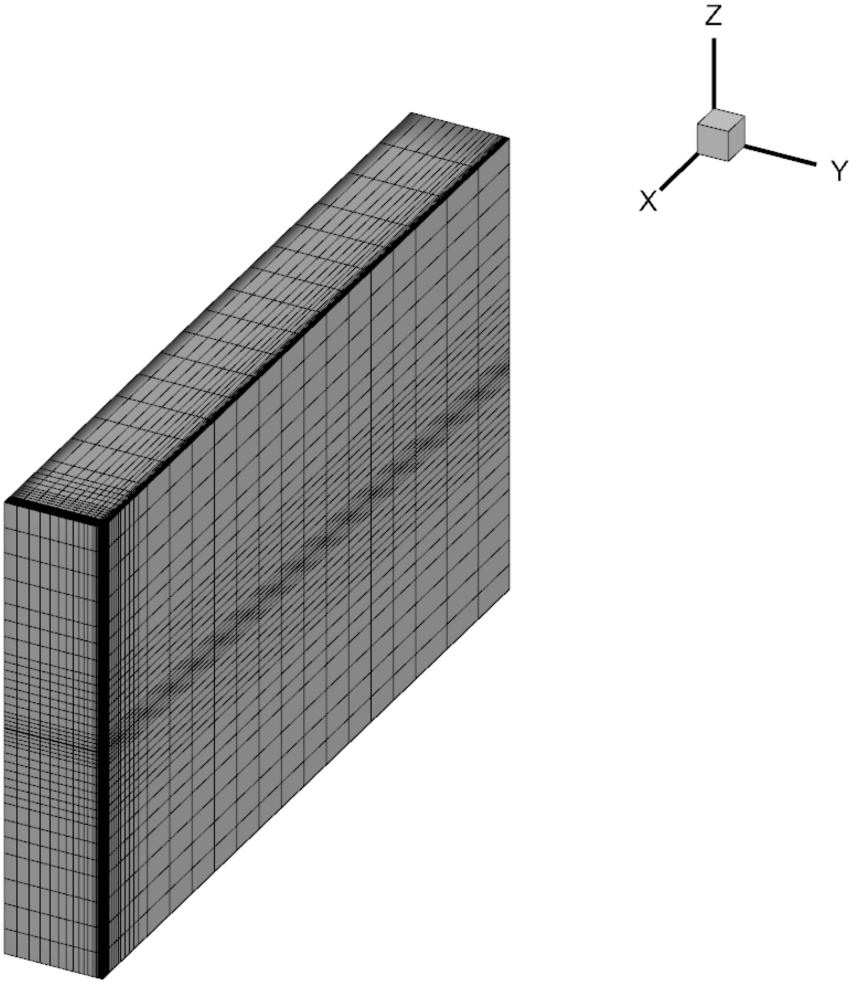

Figure 4.4 Discretization of the Stencil

4.4 History matching

History matching is a process that involves tuning a mathematical model to yield results as close as possible to reality (*i.e.,* field observations of production data) by continuously adjusting the reservoir parameters. In other words, the accuracy of my reservoir model and the reliability of key input parameters can also be verified through history matching. This process is often conducted using a trial-and-error method involving cycles of adjustment of the reservoir parameters and comparisons to field data until an acceptable agreement is attained. In this study, parameter tuning in the history matching process is based on Gauss-Newton least-square techniques, as implemented by (Thomas *et al.*, 1972).

In my study, the perturbation parameters to be optimized through the history-matching process were the intrinsic permeabilities of the fracture and the matrix, as well as the relative permeability parameters (*i.e.*, the irreducible water and oil saturations and the exponents of the relative permeability models) in the matrix. The objective of this process is to determine the parameters that minimize the error between the observed historical production data and the numerical results obtained from the flow simulator, as described by **Eq. 4.16**.

$$E = \sum_{k=1}^{m} \left[f^k \left(x_1, x_2, ...x_n \right) \right]^2 \quad \text{.......} \quad (4.16)$$

Where E is the target function to be minimized. f^k is the k^{th} difference value between the observed and the calculated data.

where the error term with a weight factor is defined as

$$f^k \left(x_1, x_2, ...x_n \right) = w_k \left(q_{obs}^k - q_{sim}^k \right), k = 1, 2, ..., \mathrm{m} \quad \text{.......} \quad (4.17)$$

q_{obs} is the observation data. q_{sim} is the calculated data. w is the weighting factor. $\boldsymbol{x}$ is the vector of the reservoir parameter.

Minimization of E requires that its first-order derivative be

$$\frac{\partial E}{\partial x_i} = 2\sum_{k=1}^{m}\left[f^k\left(\boldsymbol{x_0} + \Delta\boldsymbol{x}\right)\frac{\partial f^k\left(\boldsymbol{x_0} + \Delta\boldsymbol{x}\right)}{\partial x_i}\right] = 0 \qquad (4.18)$$

$\boldsymbol{x_0}$ is the vector of the variable given at the present position. $\Delta\boldsymbol{x}$ is the vector of variable giving distance to the minimum, $\boldsymbol{x} - \boldsymbol{x_0}$.

Applying a Taylor's series expansion to the error term results in

$$f^k\left(\boldsymbol{x_0} + \Delta\boldsymbol{x}\right) = f\left(\boldsymbol{x_0}\right) + \sum_{j=1}^{n}\Delta x_j \frac{\partial f}{\partial x_j} \qquad (4.19)$$

Substitute **Eq. 4.19** into **Eq. 4.18** yields

$$\sum_{k=1}^{m}\left[f^k\left(\boldsymbol{x_0}\right) + \sum_{j=1}^{n}\Delta x_j \frac{\partial f^k}{\partial x_j}\right]\frac{\partial f^k}{\partial x_i} = 0 \qquad (4.20)$$

The Gauss-Newton least-squares equation is expressed as

$$\sum_{j=1}^{n}\sum_{k=1}^{m}\left[\frac{\partial f^k}{\partial x_i}\frac{\partial f^k}{\partial x_j}\right]\Delta x_j = -\sum_{k=1}^{m} f^k\left(\boldsymbol{x}_0\right)\frac{\partial f^k}{\partial x_i} \qquad (4.21)$$

Eq. 4.21 can be written in matrix as $A\triangle x = b$. Where A and b can be expressed as

$$A_{ij} = \sum_{k=1}^{m}\left[\frac{\partial f^k}{\partial x_i}\frac{\partial f^k}{\partial x_j}\right], j = 1, 2, ...n, i = 1, 2, ...n \qquad (4.22)$$

$$b_i = -\sum_{k=1}^{m} f^k\left(\boldsymbol{x}_0\right)\frac{\partial f^k}{\partial x_i}, i = 1, 2, ...n \qquad (4.23)$$

To test the optimal value, the method evaluates the partial derivatives in **Eqs. 4.22** and **4.23** by perturbing each variable separately while keeping the rest of the perturbation variables unchanged. The process involves several iterations, with the results of the last parameter determination cycle through the Gauss-Newton (GN) process serving as the starting point for the next iteration. In a well-behaving system and if the number of perturbed parameters is not very large, the sum of square errors keeps decreasing with each iteration until a minimal error value or the maximum number of iterations are reached.

As shown in **Figure 3.3**, the choke is not fully opened during the entire production period. The choke is fully opened from t = 80 days to t = 300 days of production, which defines the period for the history matching of the production data. The objective for history matching is to minimize the error between the set of observed and calculated performance data in a least-squares method.

The flow, geomechanical and thermal properties of the fracture and matrix, as well as the initial conditions are listed in **Table 4.1**. The initial aqueous and oil saturation ($S_{A,}$ *and* S_o) were uniformly distributed in the matrix and the fracture.

Table 4.1 Input Parameters

Parameter	Value
Initial pressure, P_0	3.8×10^{7} pa (5565 psi)
Bottomhole pressure, P_{wf}	1.3×10^{7} pa (2000 psi)
Initial temperature, T_0	90 °C
Initial matrix saturation	S_A=0.45, S_O=0.55
Initial gas-oil ratio, SCF/BBL	2867
Bubble point pressure	3.5×10^{7} pa (5053 psi)
Oil API	40.1
Matrix porosity, ϕ	0.03
Matrix pore compressibility, α_p	3.37×10^{-9} Pa^{-1}
Matrix permeability	7.0×10^{-19} m^2 (700 nD)
Matrix k_{rel} model parameters	S_{irA}=0.25, S_{iro}=0.25, S_{irG}=0.05 n_A =3.0, n_o=2.5, n_G=2.0
Matrix capillary pressure parameters	$n=1.86$, S_{wr}=0.25
Matrix Poisson's ratio	0.25
Matrix Young's Modulus	20 GPa
Matrix Biot's coefficient	0.7
Fracture porosity, ϕ_f	0.5
Fracture permeability	8.0×10^{-13} m^2 (0.8 Darcy)
Fracture k_{rel} model parameters	S_{irA}=0.1, S_{iro}=0.05 , S_{irG} =0.01 n_A =2.2, n_o=2.5, n_G=1.5
Fracture Poisson's ratio	0
Fracture Young's Modulus	200 MPa
Fracture Biot's coefficient	0.7
Initial stress	$H_{x,y}=5.0\times10^{7}$pa, $H_z=7.0\times10^{7}$pa
Rock density, kg/m^3	2600
Matrix specific heat, J/kg/K	1000

The geomechanical boundary conditions are shown in **Figure 4.5**: on the top face, there are displacements in the *x*, *y* and *z* directions; there are also displacements in the remaining 5 faces, but no displacements in the directions that are normal to the surfaces.

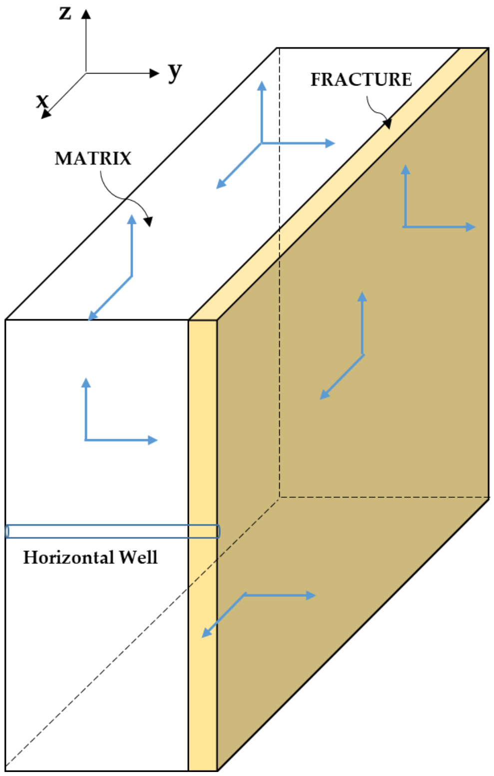

Figure 4.5 3D Geomechanical Boundary Conditions of the Basic Simulation Case

The base case before the onset of the history-matching process involved ranges of reasonable parameter estimates that were in line with values provided by coarse scale simulations provided by the petroleum company supporting this study. These parameters and their ranges described the intrinsic and relative permeability behavior of the fractured system and are listed in **Table 4.2**.

Table 4.2 Parameters Sensitivity Analysis

Parameters		Low	Base	High
Relative Permeability	Water RelPerm Exponent, n_w	2.0	3.0	4.0
	Oil RelPerm Exponent, n_o	2.0	2.5	3.0
	Oil Irreducible Saturation, S_{or}	0.2	0.3	0.35
	Water Irreducible Saturation, S_{wr}	0.2	0.25	0.3
Fracture Permeability, D		0.3	0.5	1.0

The uncertainty in each of these parameters is analyzed via the tornado plot shown in **Figure 4.6**. In this plot, the effects of the 5 parameters on the oil cumulative production are calculated and displayed. The % change in the oil cumulative production for a ±1% perturbation in the value of each parameter is quantified. From this plot, it is clear that the exponent n_o of the oil relative permeability in the matrix has the greatest effect on the oil cumulative production: an increase by 1% in the value of this exponent corresponds to an increase by 1.096% in the cumulative oil production compared to that in the base case; a decrease by 1% in the value of n_o results in a decrease in the cumulative oil production by 1%.

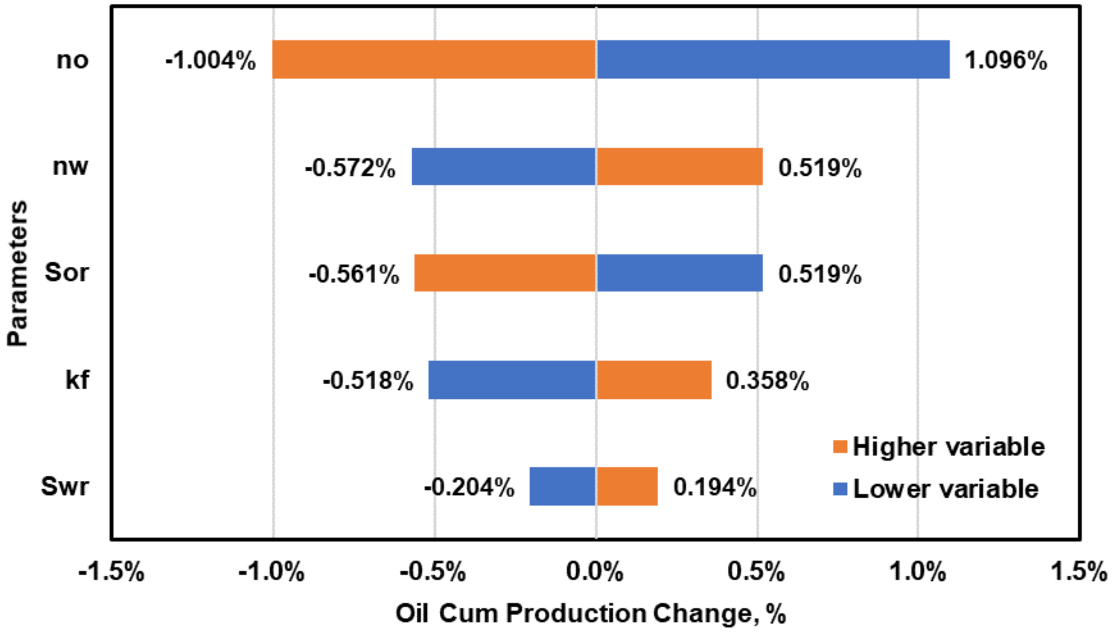

Figure 4.6 Uncertainty Analysis of Parameters in Tornado Plot

After multiple Gauss-Newton runs, the optimal values of all perturbation parameters were obtained and are listed in **Table 4.3**. Note that the relative permeability parameters of the matrix and the fracture permeability were obtained through history matching, which helped in the creation of reliable set of inputs for the coupled flow-geomechanical model. A comparison of the field data of cumulative production of oil, water and gas, and the corresponding numerical simulation predictions (obtained with the optimized parameters of **Table 4.3**) in **Figure 4.7** shows a very good agreement of the two data sets.

Table 4.3 Optimized Parameters

Parameters	Optimized Values	Field Reference Values
k_f, m^2 (Darcy)	8x10^{-13} m^2 (0.8 Darcy)	1.2x10^{-13} m^2 (0.12 Darcy)
n_o, matrix	2.5	/
S_{iro}, matrix	0.25	0.3
n_w, matrix	3.0	/
S_{irw}, matrix	0.25	0.15-0.25

As shown in **Figure 4.7**, the solid lines indicate the simulation results and the symbols are the historical field data of cumulative production. The proximity of the two is obvious, thus lending credibility to the optimized values of the perturbation parameters. The optimized fracture permeability is 8x10^{-13} m^2 (0.8 Darcy), comparing to the reference value (initial estimate) of 1.2x10^{-13} m^2 (0.12 Darcy). The oil and water irreducible saturations are both 0.25, and align well with the initial estimates of these two parameters (0.3 and 0.15-0.25, respectively). The exponents of the relative permeability models for oil and water are 2.5 and 3.0, respectively, which are both reasonable values. Thus, I conclude that my history-matched results are reliable.

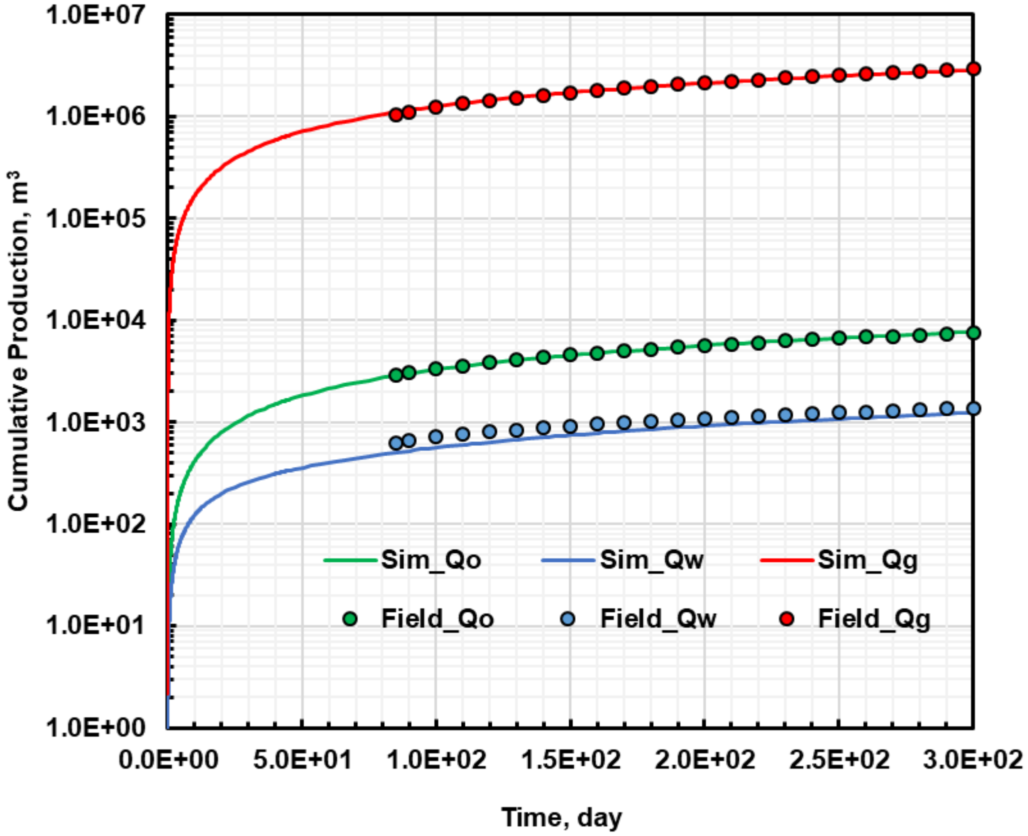

Figure 4.7 Comparison of Field Data and Optimized Numerical Predictions of Cumulative Production

In the next activity, the history-matched optimized parameters were used as inputs in the base case for the analysis and evaluation of the drawdown strategies that are discussed in Chapter V.

CHAPTER V

PRODUCTION STRATEGIES

5.1 Introduction

Pressure drawdown management is needed in order to control production by setting an appropriate bottomhole pressure that can meet production criteria such as maximal EUR or net present value. The drawdown management strategy can play an important role in avoiding rapid and excessive drawdown, which may cause excessive sand production or adverse development of stresses that can result in proppant crushing and/or embedment. In this component of my study, I explore various BHP drawdown plans in an effort to identify the scenario(s) that can yield maximal production.

5.2 Drawdown Strategies Cases

5.2.1 Drawdown Strategies Comparison

I investigated the three different bottomhole pressure drawdown schedules shown in **Figure 5.1** in an effort to determine their impacts on production. In the constant BHP case (Case S1), the bottomhole pressure was maintained unchanged at 13.79 MPa (2000 psi) during the 3-year production period. In the stepwise-declining BHP case (Case S2), the bottomhole pressure decreased from its original value to the 13.79 MPa (2000 psi) level in a series of six distinct depressurization stages, each one lasting 5 days and being characterized by the same pressure drop. The BHP remains constant at the 13.79 MPa (2000 psi) level after the first 30 days. In the linearly-declining BHP case (Case S3), the

BHP decreases linearly from the initial 33.09 MPa (4800 psi) level to 13.79 MPa (2000 psi) in the first 30 days, and remains constant at that level until the end of production.

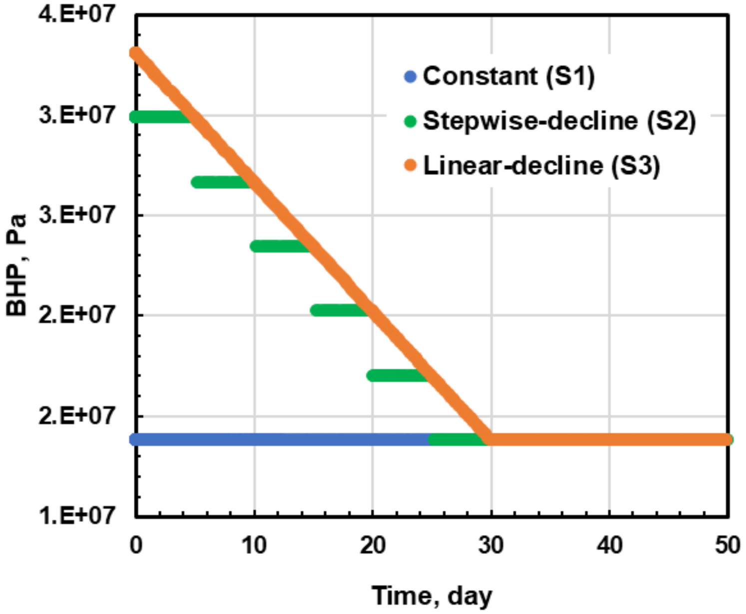

Figure 5.1 The Different Drawdown Strategies in the Production Simulations

The evolution of the rate of oil production and the cumulative oil production over time are shown in **Figures 5.2** and **5.3**. The constant BHP case (Case S1) has the largest initial rate of oil production among the three cases. This is caused by the lowest BHP during the first 30 days of production, as illustrated in **Figure 5.1**. As time advances, the oil production rates of the three cases tend to converge and become almost identical at *t* = 3 years. Case S1 case has the largest cumulative oil production very early in the production period (~10 days), but Cases S2 and S3 have consistently larger cumulative oil production after that time. At *t* = 3 years, the cumulative productions in Case S2 and the S3 are practically the same: 17.17 vs. 17.35 x10^3 m^3 (108 vs. 109 MSTB), respectively.

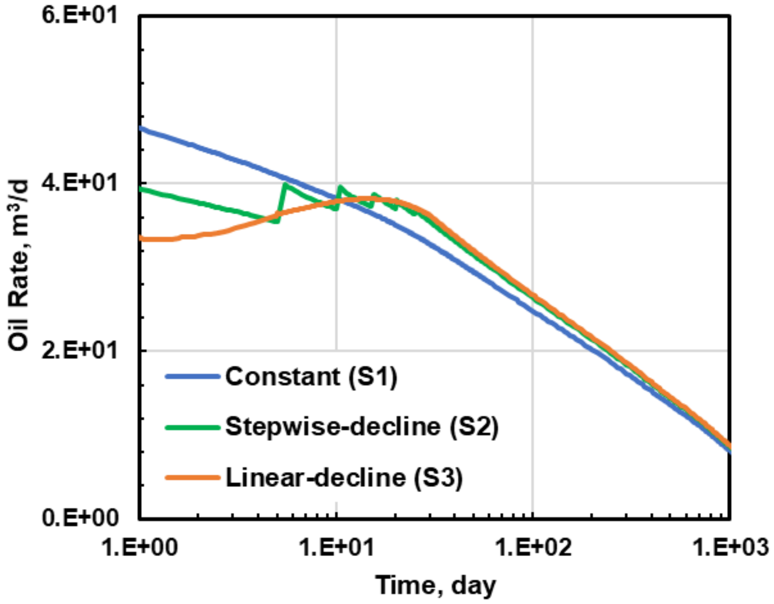

Figure 5.2 Oil Rate Evolution for Alternative BHP Management Strategies

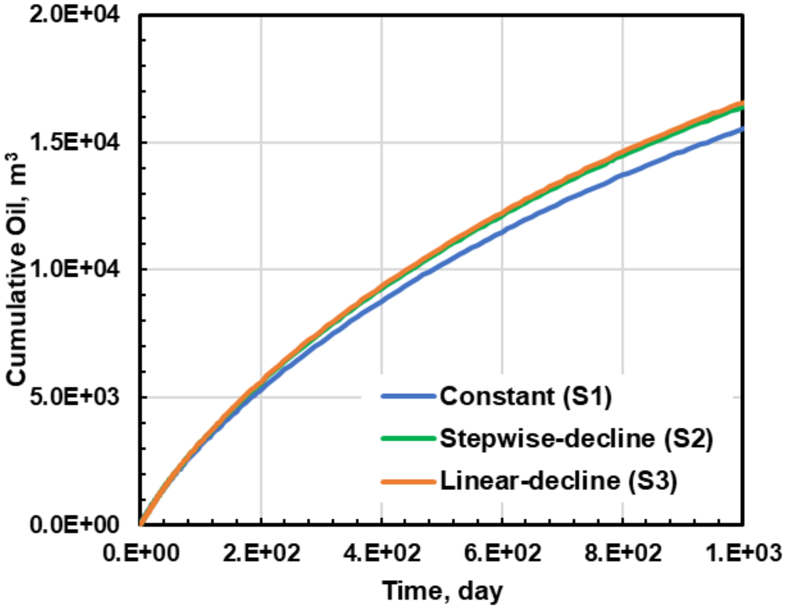

Figure 5.3 Comparison of Oil Cumulative Production for Different BHP Management Strategies

In **Figure 5.4**, we compare the cumulative oil production for the three BHP management options at t = 10 days and t = 3 years. At t = 10 days, production in Case S1 (constant

BHP) yields the largest amount of cumulatively produced oil 421 m^3 (2.6 MSTB). This was expected because of the largest pressure drawdown at the well, and is a strategy that appears to offer the fastest way to recover the investment. At the end of the 3-year production period, the Case 3 option yields 17,350 m^3 (109.2 MSTB), which is the highest cumulative oil production and represents an increase of 1.1% over that Case S2, and an increase of 6.8% over that in Case S1.

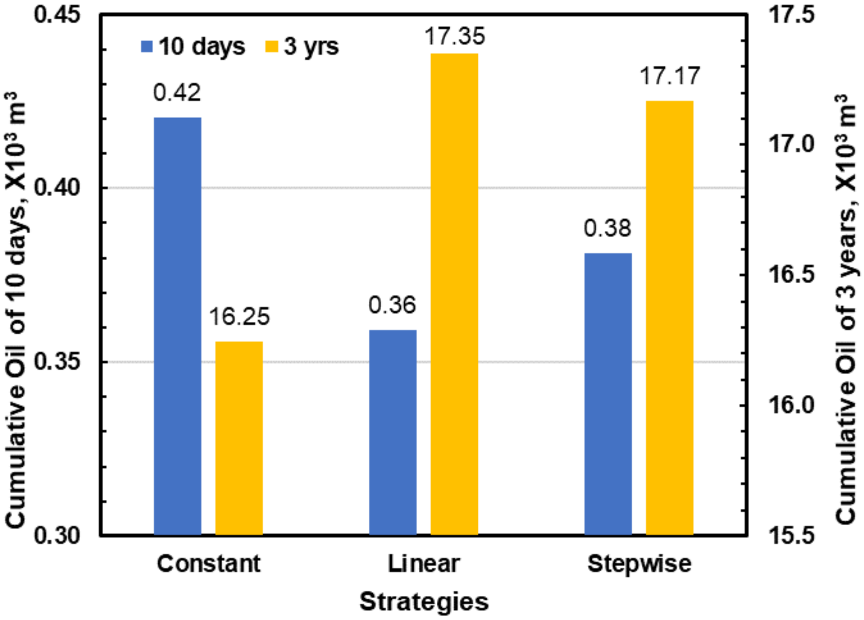

Figure 5.4 Comparison of Short- and Long-term Cumulative Oil Production

Figure 5.5 displays the evolution of the spatial distributions of pressure in the three BHP cases during production. As expected, the pressure in the domain declines over time. Although there are some visible differences in the early pressure distributions of the three cases (with the constant BHP case showing the largest decline), these become rapidly attenuated and the pressure distributions do not show significant (if any) differences at later times, *i.e.*, at $t > 180$ days.

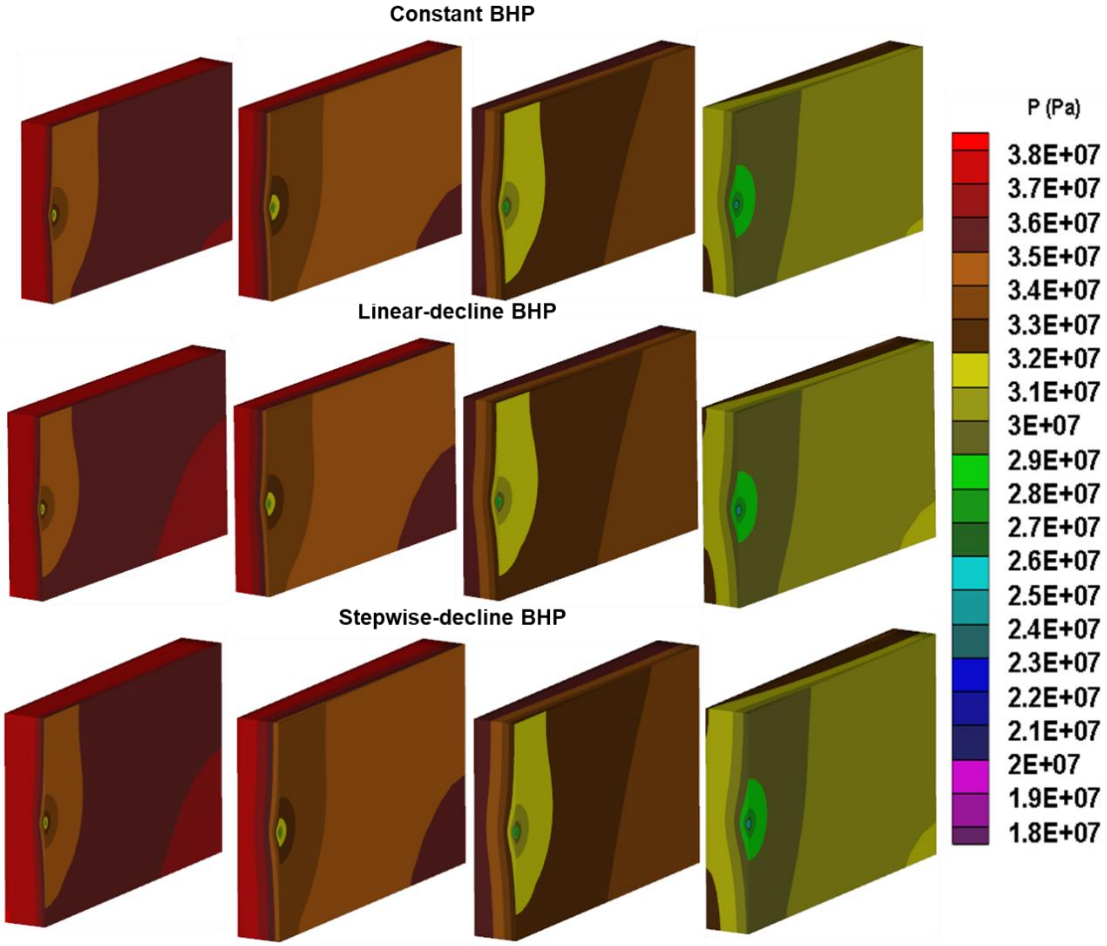

Figure 5.5 The Pressure Distribution in the Stencil at *t* = 30, 180, 360 Days and 3 Years from Left to Right for Different BHP Management Strategies.

Figure 5.6 shows the evolution of the fracture aperture over time in the grid block (element) that is close to the horizontal wellbore. Initially, the fracture aperture exhibits the largest decrease in Case S1 because of the largest pressure drops associated with this option. The largest aperture at early times occurs in the Case S3 (linearly-declining BHP), and the aperture in Case S2 (stepwise-declining BHP) is between the other two and follows the stepwise pattern of the declining pressure. The HF aperture decreases with time in all three cases. The rate of the narrowing of the fracture aperture slows as time advances in all three cases because of reduction in the fracture stress. At *t* = 3 years, the fracture aperture in case S1 is 0.867 mm from the original value of 1 mm. At the same time, the fracture apertures in Cases S2 and S3are both 0.863 mm, *i.e.*, not very different from that Case S1. clearly indicates that a significant pressure drawdown within a short time will lead to an early and sharp decrease in the fracture aperture, which has the potential to adversely affect the short-term production goals, but the long-term effect appears to be minor.

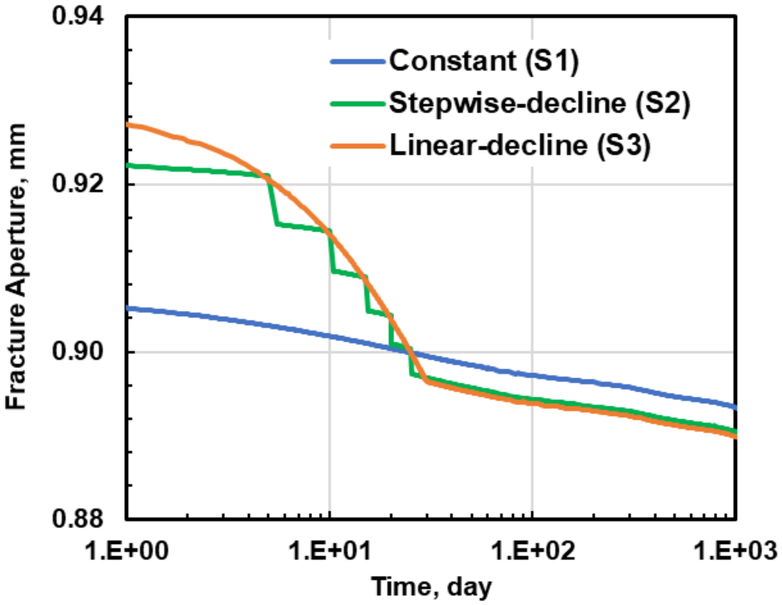

Figure 5.6 Evolution of Fracture Aperture for Different BHP Management Strategies

Figure 5.7 displays the fracture volumetric strain during production, which describes the shrinkage in the original fracture volume. The volumes of the fracture elements in grid are updated at each timestep, as affected by changes in the fracture aperture. At *t* = 1 day, the volumetric strain in Case S1 stands at the lowest (of all cases) initial value of -0.0348, with the negative sign denoting a decrease in the fracture element volume because of the high initial stresses in this case and the lowest value indicating the largest volume reduction, which lasts for around 30 days until the volumetric strains in the other two scenarios surpass it. This indicates that an increasing fracture volume reduction results in a lower long-term cumulative oil production.

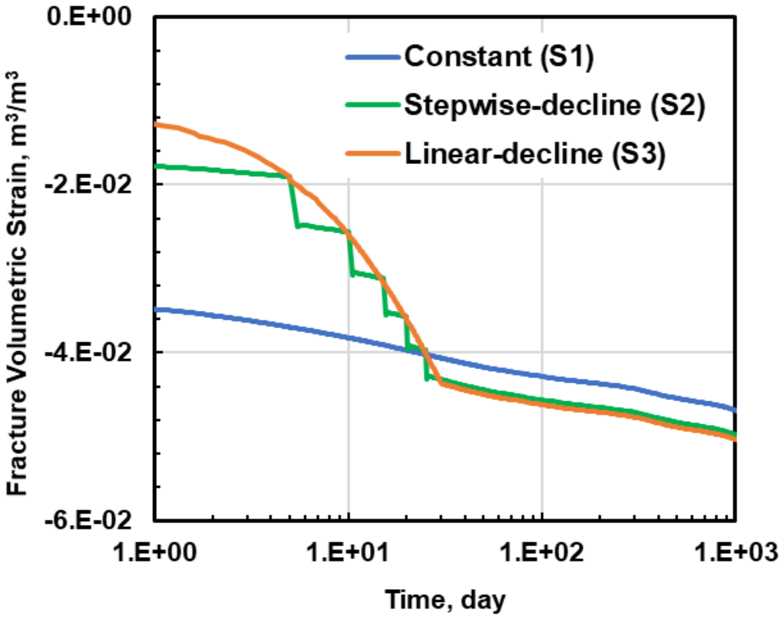

Figure 5.7 Evolution of Volume Strain in the Hydraulic Fracture for Different BHP Management Strategies

In **Figure 5.8,** the evolution of the HF fracture porosity shows significant reductions from the original level of 0.5 in all three BHP management cases. At the beginning of production, the HF porosity Case S1 decreases sharply to about 0.32 in the HF elements, but the porosities in the three cases converge and continue to decline for $t > 30$ days, reaching the level of 0.22 in all cases after 3 years of production.

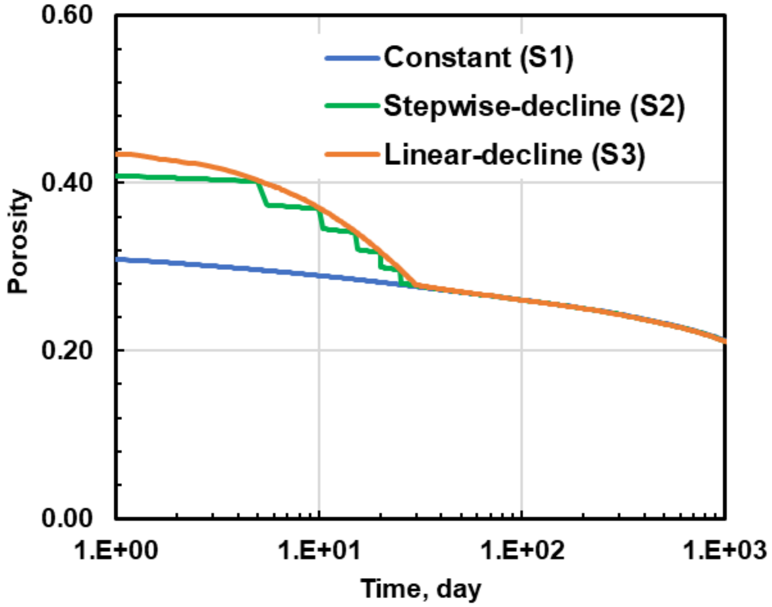

Figure 5.8 Evolution of Porosity in the Hydraulic Fracture for Different BHP Management Strategies

Figure 5.9 shows the evolution of the fracture permeability over time for three BHP strategies. At *t* = 1 day, the HF permeability in Case S3 is the highest at 3.7x10^{-13} m^2 (0.37 Darcy); the HF permeability in Case S2 is 2.53x10^{-13} m^2 (0.253 Darcy), and is the lowest at 8x10^{-14} m^2 (0.08 Darcy) in Case S1. The change in the permeability over time reflects the combined effects of the decline in fracture aperture and in the HF porosity. Note that the HF permeabilities in the three cases converge for *t* > 30 days.

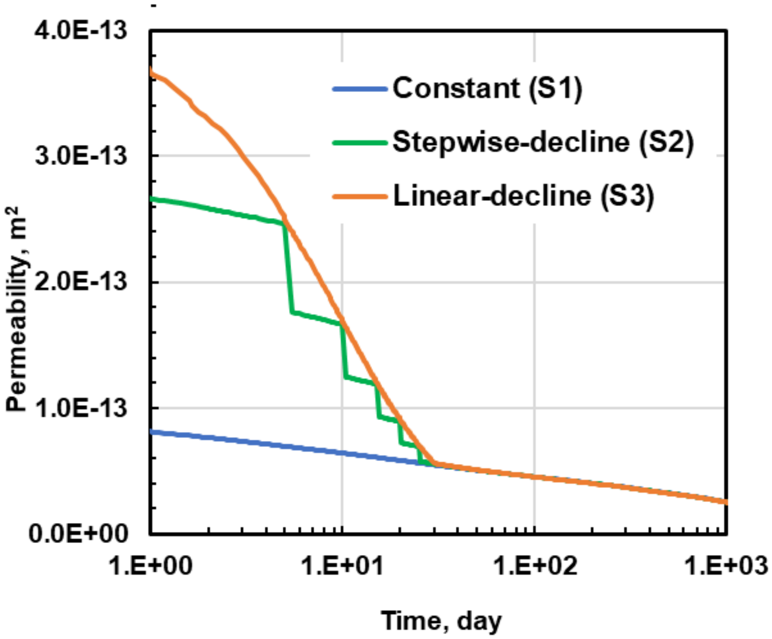

Figure 5.9 Evolution of Permeability in the Hydraulic Fracture for Different BHP Management Strategies

In conclusion, a continuous linear drawdown appears to be the better strategy for short-term production and system behavior, compared to the cases of stepwise-declining and constant BHP, but the advantages of this strategy become less pronounced for longer production periods. Sharp pressure drawdowns that are imposed at the onset of production can affect sharp reductions in the fracture volume, porosity and permeability, resulting in lower oil recoveries.

5.2.2 Final Drawdown Level

In this section, I discuss the effects of the level of the pressure drawdown on the production performance. The three cases I investigated Cases P1, P2 and P3, corresponding to lowest BHPs of 13.8, 17.3 and 20.7 MPa (2000, 2500 and 3000 psi), respectively. In all three cases, the BHP decreases linearly in the first 30 days and thereafter is kept constant at its final level. **Figure 5.10** shows the BHP control over the first 50 days of production.

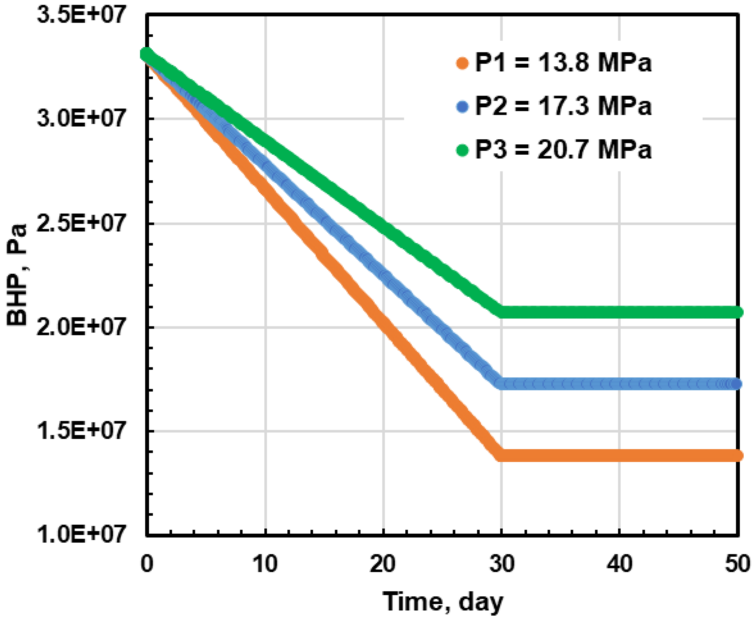

Figure 5.10 Final Drawdown Level Cases

In **Figure 5.11**, the oil production rates peak at around 20, 25, 30 days in Cases P1, P2 and P3, respectively. A larger pressure drawdown results in a higher peak production rate, but the rates appear to converge for *t* > 400 days. **Figure 5.12** shows the cumulative oil production of in the 3 cases over *t* = 3 years. A larger pressure drawdown results in a higher cumulative oil production. At *t* = 3 years, the difference between the maximum (Case P1) and minimum (Case P3) cumulative oil production is about 476.7 m^3 (3,000 barrels).

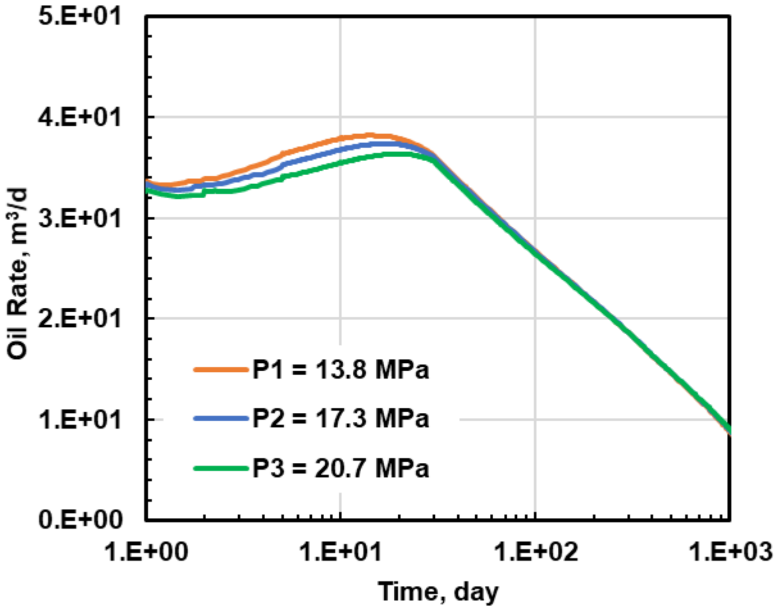

Figure 5.11 Effect of Total Drawdown on the Oil Production Rate

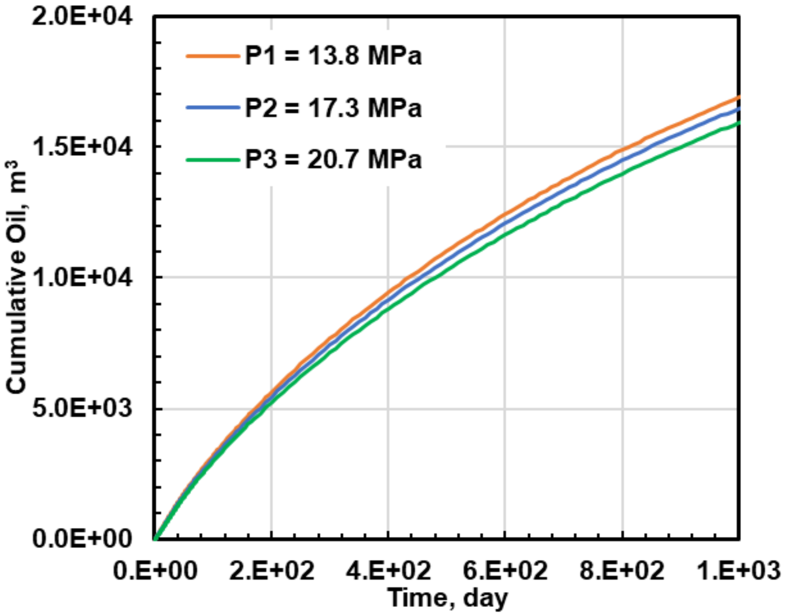

Figure 5.12 Effect of Total Drawdown on the Cumulative Oil Production

Figure 5.13 displays the evolution of the pressure profile over time in Cases P1, P2 and P3. The differences in the spatial distributions of pressure (a) at the same time for the cases and (b) in the same care at different times are obvious and easily discernible, with the pressures in Case P1 showing the largest and strongest declines (as expected).

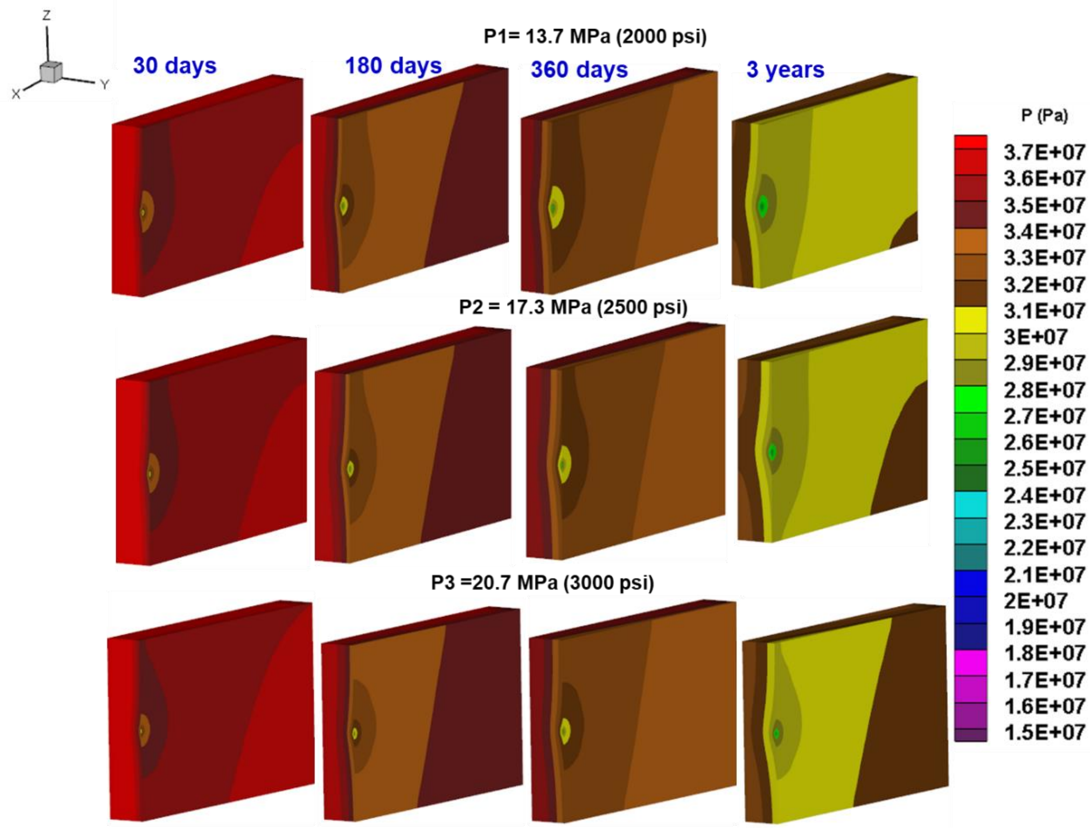

Figure 5.13 Effect of Total Drawdown on the Pressure Distributions in the Stencil at *t* = 30, 180, 360 Days and 3 Years from Left to Right

Figure 5.14 shows the evolution of porosity in the hydraulic fracture. The HF porosity declines the fastest in Case P1, and the slowest in Case P3. At t = 30 days, the HF porosity in cases P1, P2 and P3 is reduced substantially from the initial value of 0.5 to 0.278, 0.295 and 0.318, respectively. The rate of the HF reduction in the porosity declines further for t > 30 days, and the final porosity at t = 30 days is 0.21, 0.23 and 0.26 in Cases P1, P2 and P3. Thus, a declining BHP is associated with a lower HF porosity at any time during production.

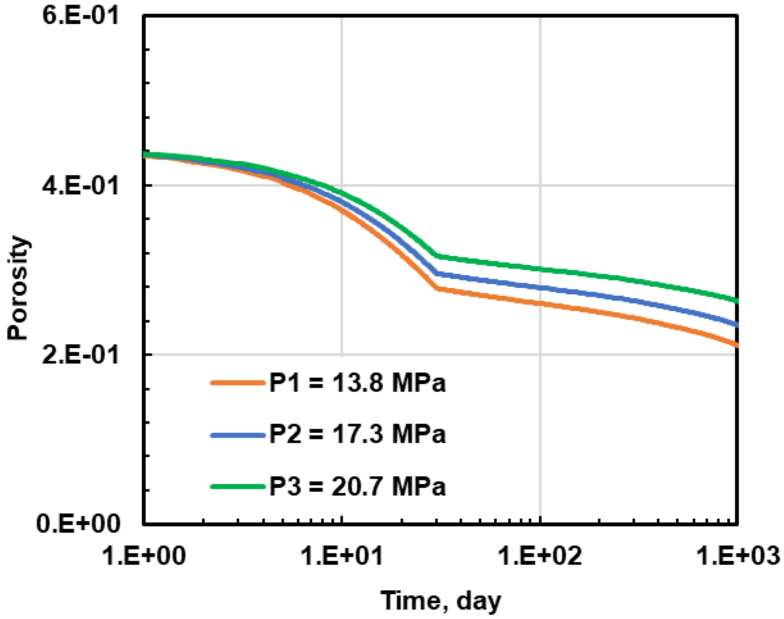

Figure 5.14 Effect of Total Drawdown on the Porosity in the Hydraulic Fracture

The evolution of the HF permeability over time in **Figure 5.15** shows a monotonic decline with time and reflects the combined effects of declining porosity and reduced fracture aperture. The larger the BHP pressure, the larger the permeability at any time during production. At t = 3 years, the fracture permeability in Cases P1, P2 and P3 shows a substantial decline from the initial level of $8x10^{-13}$ m^2 (0.8 Darcy) to $2x10^{-14}$, $3.3x10^{-14}$ and $4.6x10^{-14}$ m^2 (0.0254, 0.033 and 0.046, Darcys), respectively.

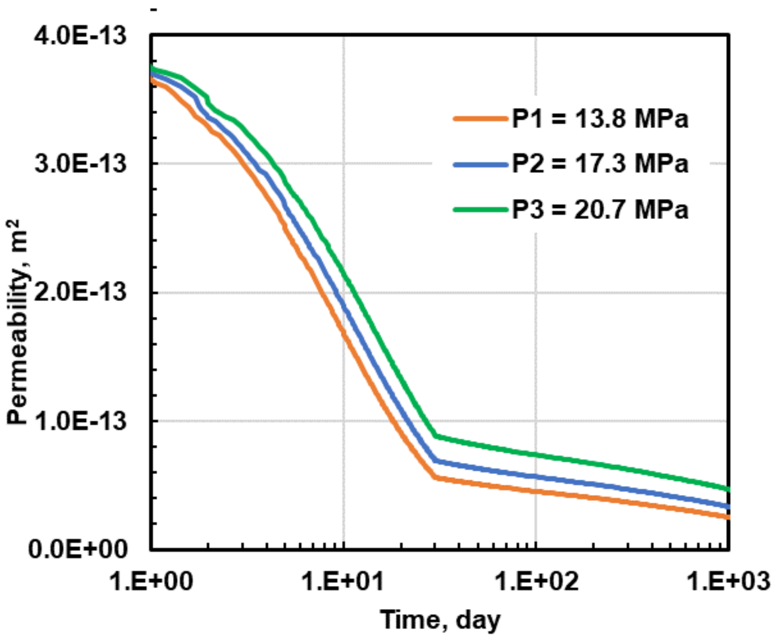

Figure 5.15 Effect of Total Drawdown on the Permeability in the Hydraulic Fracture

Figure 5.16 shows the fracture aperture evolution vs. the production time. As expected, the larger the BHP, the smaller the reduction in the fracture aperture, but the differences appear small. At *t* = 3 years. The HF aperture is reduced from its original level of 1 mm to about 0.89 mm for all three cases in this study.

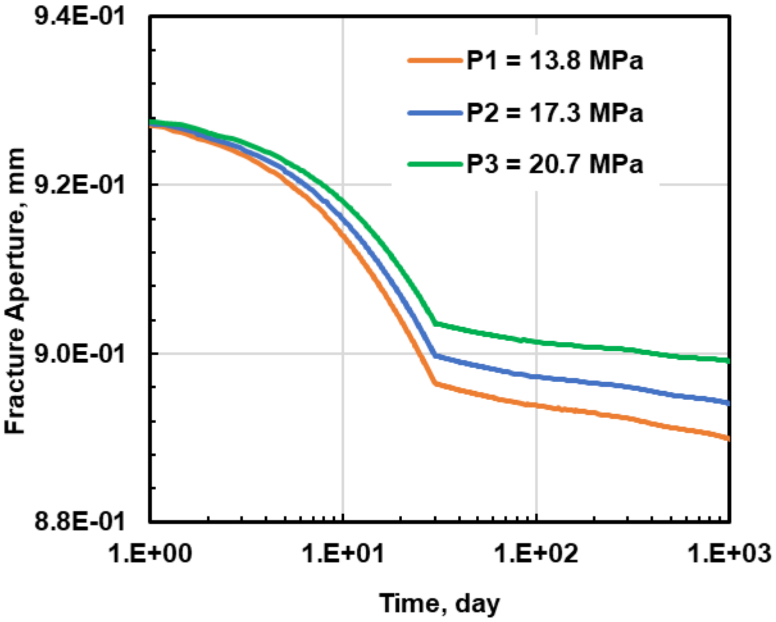

Figure 5.16 Effect of Total Drawdown on the Fracture Aperture

Figure 5.17 descripts the evolution of the volumetric strain of the HF subdomain as time advances. As discussed earlier, the negative sign in the volumetric strain indicates volume reduction. The early volumetric strains are practically identical in all cases because of the same initial pressure drawdown, but they diverge as time advances and production continues. At *t* = 3 years of production, the volumetric strains in Cases P1, P2 and P3 are substantial at -0.050, -0.045, and -0.040, respectively.

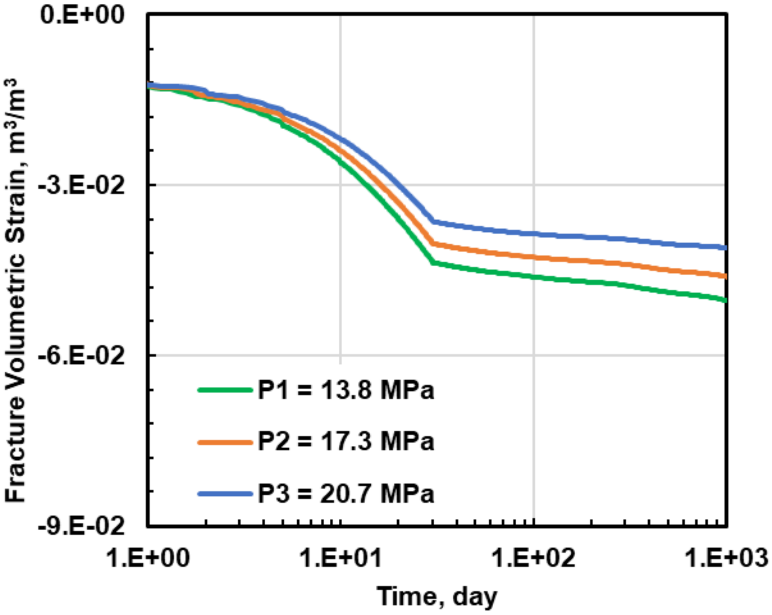

Figure 5.17 Effect of Total Drawdown on the Volumetric Strain in the Hydraulic Fracture

In summary, the total pressure drawdown plays an important role in long-term production. A larger pressure drawdown leads to larger oil production rates and a larger cumulative production of oil, but also to a lower porosity, permeability, aperture and volumetric strain in the hydraulic fracture. However, the difference in the reductions in the HF permeability and aperture are rather minor, indicating that a more aggressive low BHP strategy may be acceptable without significant adverse geomechanical implications.

5.2.3 Ramp-down Duration in Linearly-Declining BHP

I investigated the effect of the length of the BHP ramp-down period, during which the BHP is lowered from its initial level of 33.09 MPa (4800 psi) to a final level 13.79 MPa (2000 psi). The three cases R1, R2 and R3 in this study corresponded to ramp-down durations of 5, 30, 100 days, respectively. **Figure 5.18** shows the three ramp-down regimes in Cases R1 to R3 in the first 100 days of the 3-year production period. Note that the BHP is kept constant at 13.79 MPa (2000 psi) in all three cases for *t* > 100 days.

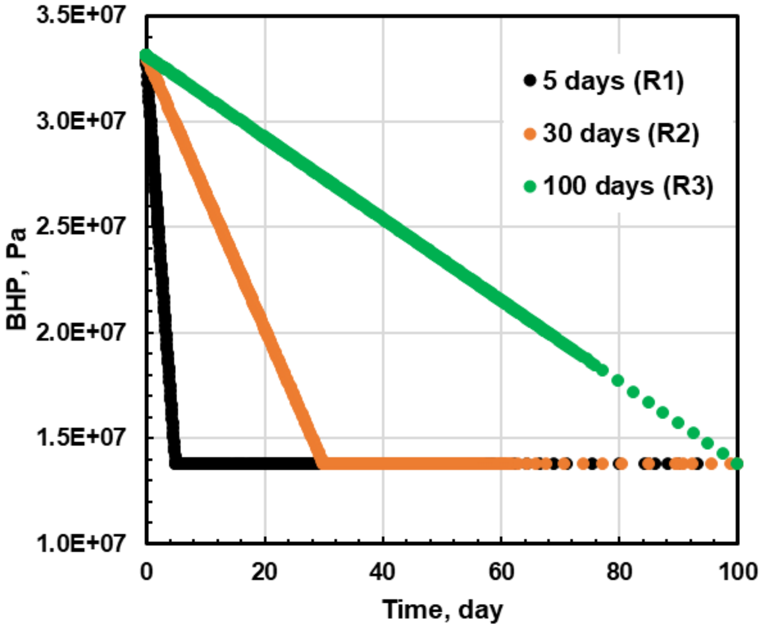

Figure 5.18 BHP Control Schedule in Ramp Down Duration Cases

The oil production rate and the cumulative oil production in Cases R1, R2 and R3 are shown in **Figures 5.19** and **5.20**. The shorter the ramp-down duration, the larger the initial oil rate and the earlier the peak rate is reached. Conversely, the longer the ramp-down period, the higher the cumulative production at the end of the 3-year period. Thus, at *t* = 3 years, cumulative production in Case R3 is 4% higher than that in Case R1.

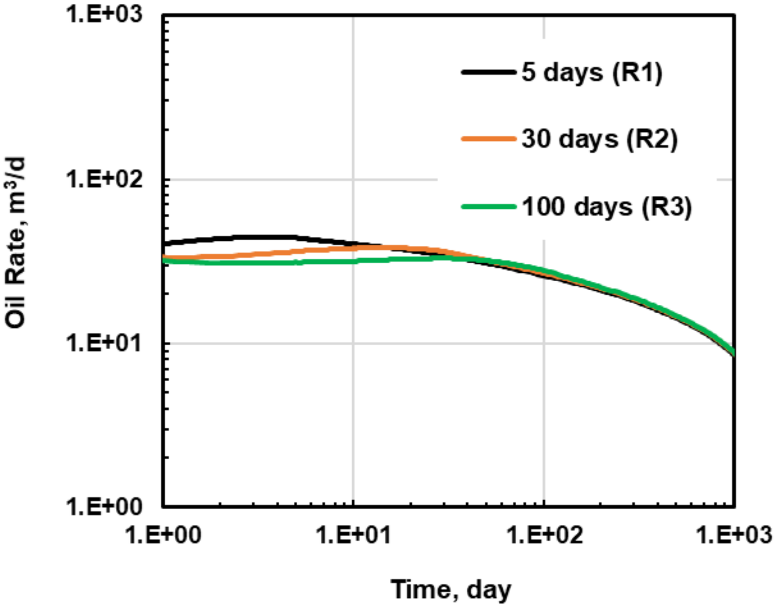

Figure 5.19 Effect of the Duration of Ramp Down on the Oil Production Rate

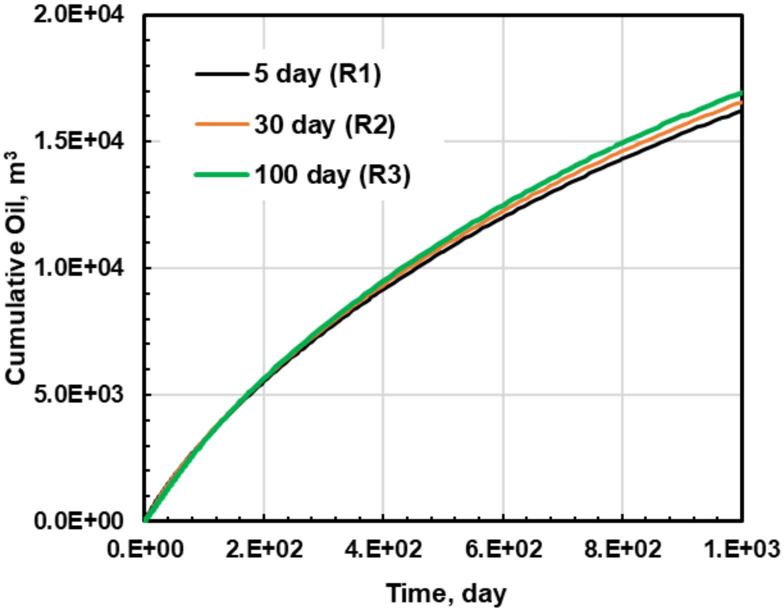

Figure 5.20 Effect of the Duration of Ramp Down on the Cumulative Oil Production

Figure 5.21 displays the evolution of the spatial evolution of pressure in the simulated domains (stencil) in Cases R1, R2 and R3. The differences in the pressure distributions in the three cases are substantial and are discernible at all times. For obvious reasons, the pressure distributions in the cases are most pronounced at t = 30 days and exhibit the smallest differences at t = 3 years.

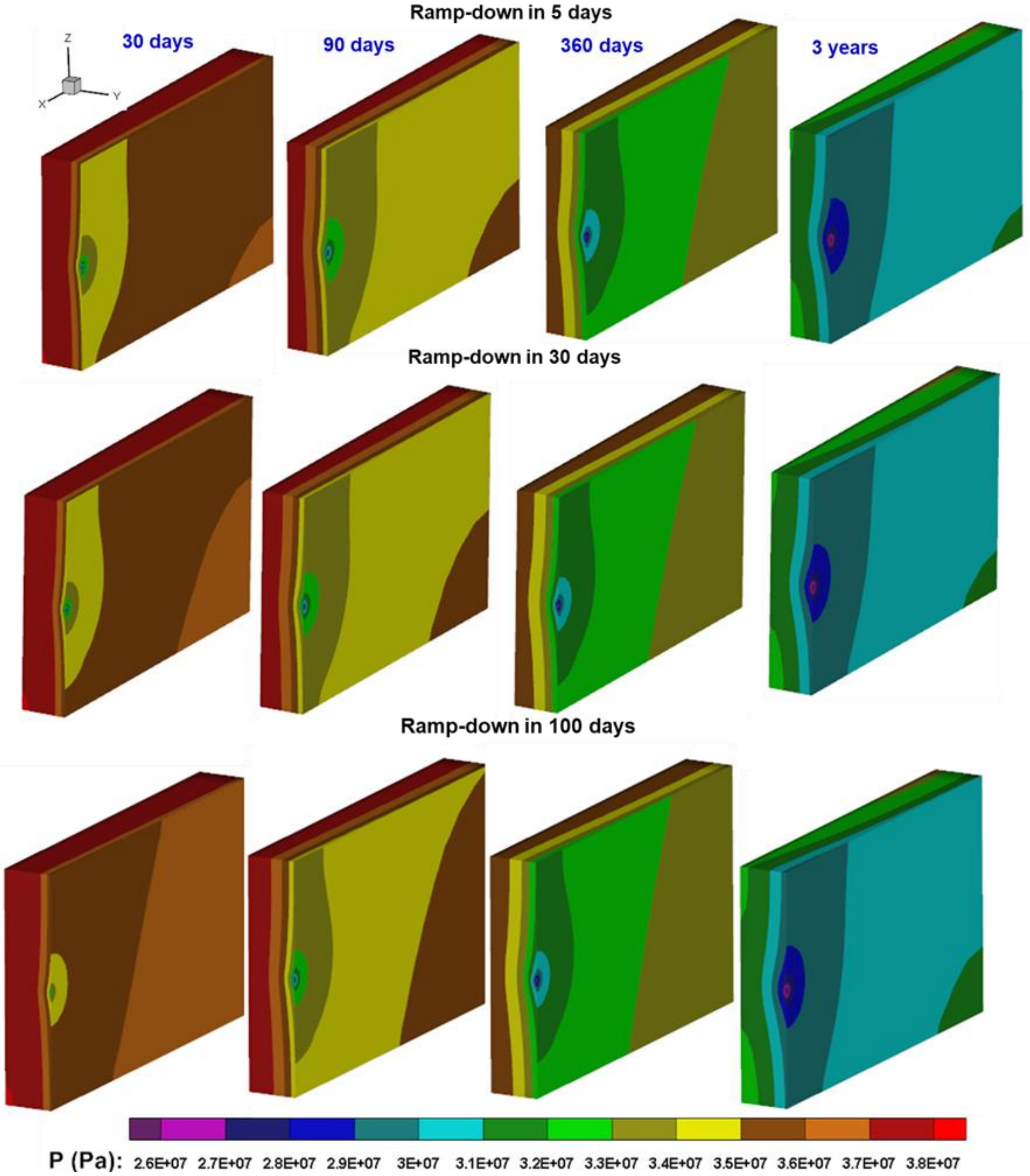

Figure 5.21 Effect of the Duration of Ramp Down on the Pressure Distribution Evolution of the Stencil at 30, 90, 360 Days and 3 Years from Left to Right

Figure 5.22 shows the porosity of the HF element that is located next to well block. The curves show that (a) the earlier declines in the HF porosity correspond to the shorter ramp-down periods and (b) the curves of the declining HF porosities in Cases R1, R2 and R3 coincide for *t* > 100 days. As in all previous cases, the reduction in the HF porosity from its initial value of 0.5 is substantial and continuous as time advances, reaching a level of 0.22 that is common to all three cases at *t* = 3 days. The longer ramp-down period in Case R3 is associated with a higher HF porosity for a longer time, and is preferable because of the potential for larger oil production.

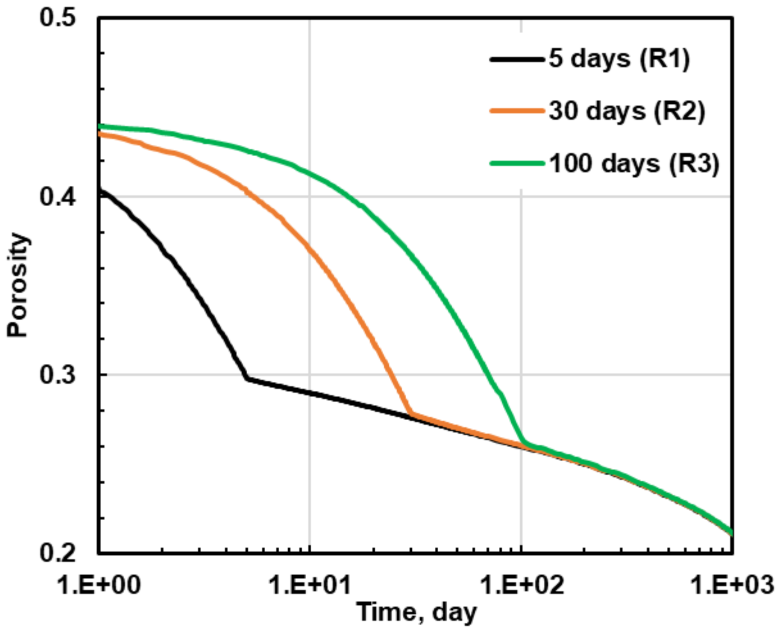

Figure 5.22 Effect of the Ramp Down Duration on the Fracture Porosity

The comparison of the evolution of the HF permeabilities in Cases R1, R2 and R3 in **Figure 5.23** reveals that (a) a shorter ramp-down duration corresponds to a lower initial permeability, (b) the HF permeability continues to decrease with time in all cases, and (c) the permeabilities in the three cases all coincide for *t* > 100 days. The HF permeability in Case R3 is 3.8x10^{-13} m^2 (0.38 Darcy) at *t* = 1 day, at which time the permeabilities in cases R2 and R1 are 3.6x10^{-13} m^2 (0.36 Darcy) and 2.47x10^{-13} m^2 (0.247 Darcy), respectively. Obviously, the longer ramp-down period in Case R3 is associated with a higher HF permeability for a longer time and is preferable because of the potential for larger oil production.

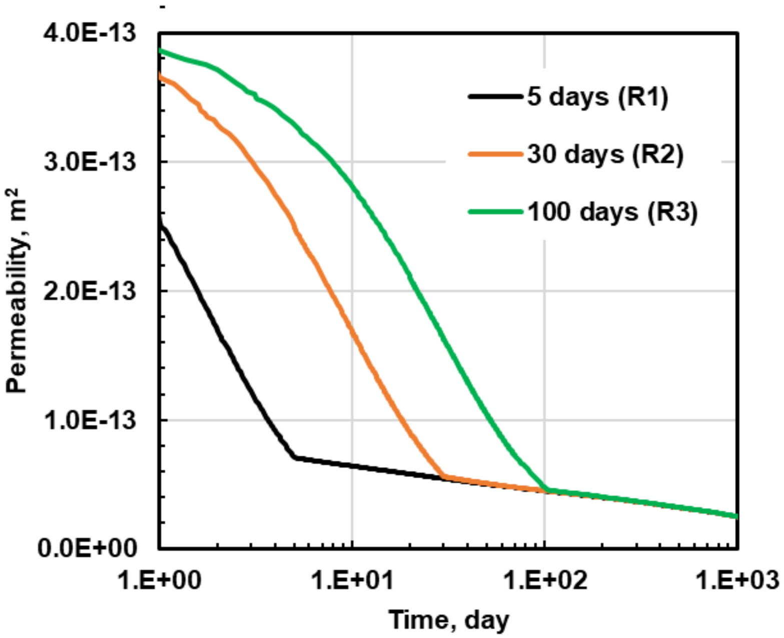

Figure 5.23 Effect of the Ramp Down Duration on the Fracture Permeability

Figure 5.24 shows the evolution of the fracture aperture in Cases R1, R2 and R3. The shorter the ramp-down duration, the larger the early-times HF aperture. However, the early-times HF apertures are not very different from each other in the three cases, and they all coincide for *t* > 100 days.

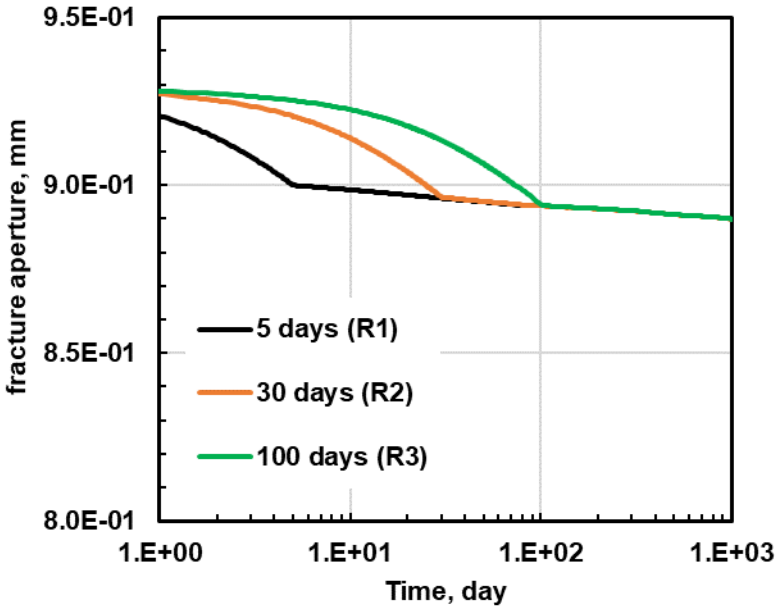

Figure 5.24 Effect of the Ramp Down Duration on the Evolution of the Fracture Aperture

Figure 5.25 shows the changes in the fracture volumetric strain with time in Cases R1, R2 and R3. A longer ramp-down duration is associated with a smaller volumetric strain (in an absolute sense) at early times, although the volumetric strains for the three cases converge for *t* > 100 days. This observation further underlines the preference for longer ramp-down periods as they correspond to larger HF volumes for longer periods that can lead to enhanced oil production.

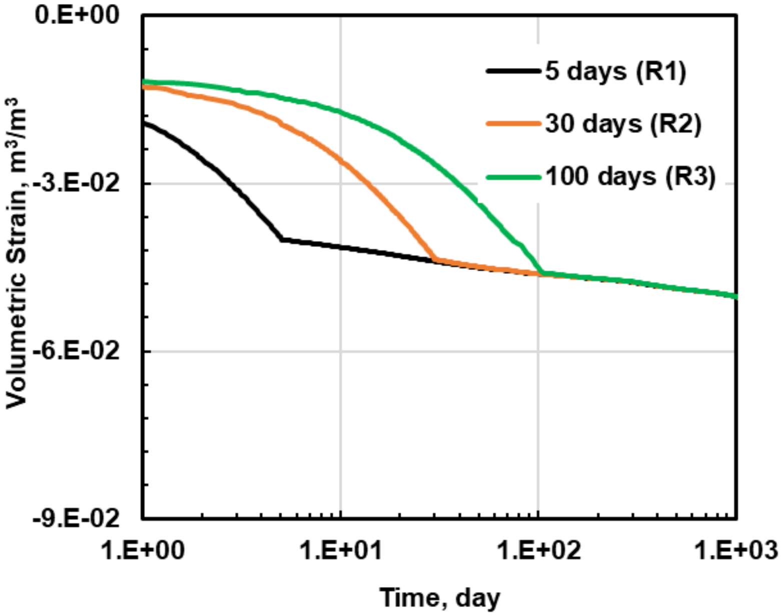

Figure 5.25 Effect of the Ramp Down Duration on the Fracture Volumetric Strain

In conclusion, the effect of the duration of the ramp-down on the production performance is significant. A short ramp-down duration is associated with higher initial (early) oil production, but with lower cumulative oil production in the long run. Conversely, a longer ramp-down period leads to larger cumulative oil production, smaller HF volume reductions and larger HF apertures, permeabilities and porosities for longer times (that coincide with the longer ramp-down periods), all of which are conducive to enhanced oil production.

5.2.4 BHP in Variable–Decline Rate

This study addresses the effects of a variable decline rate in the BHP control on production. The three BHP decline rates that I investigated (Cases V1, V2 and V3) are listed in **Table 5.1**, and they were all applied to the first 100 days of production (= the ramp-down period), after which the BHP was maintained at a constant level of 13.79 MPa (2000 psi). The variable rates in the declining-over-time BHP are described in **Figure 5.26**.

Table 5.1 Bottomhole Pressure Control Schedule

Strategy	Declining (x< 100 days), MPa	(psi)
V 1	$P_w = 33.09 - 3.03\text{x}10^{-4}\ x^{2.4}$	$(4800 – 0.044\ x^{2.4})$
V 2	$P_w = 33.09 - 0.19x$	$(4800 – 28x)$
V 3	$P_w = 33.09 - 1.9x^{0.5}$	$(4800 – 280\ x^{0.5})$

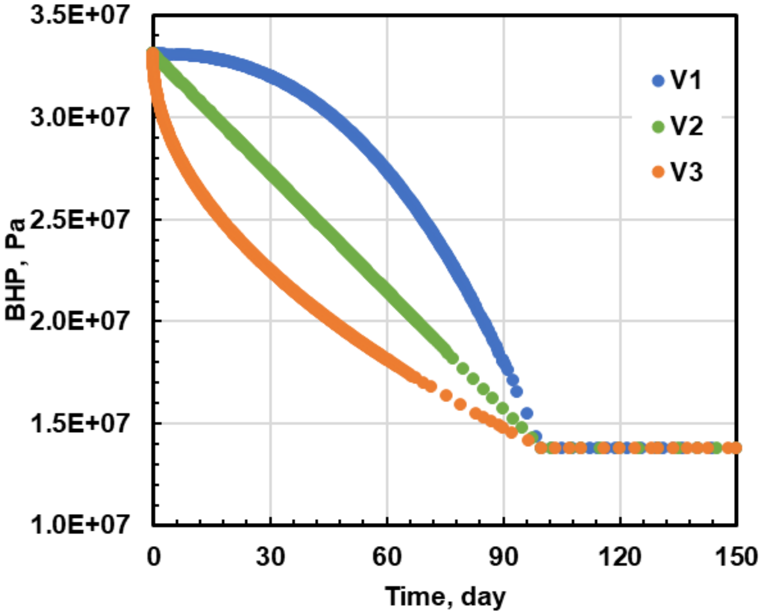

Figure 5.26 Variable BHP Decline Rates

The effect of the variable BHP decline rates in Cases V1, V2 and V3 on the oil production rate is described by **Figure 5.27**, which confirms the expectation: a faster-declining BHP is associated with a higher oil production rate. However, the differences in the oil production rates in the three cases I investigated are not very large and are observed only during the ramp-down period. Actually, the cumulative oil production corresponding to Cases V1, V2 and V3 that are shown in **Figure 5.28**. We observe very small differences at early times and practical coincidence at alter times. Thus, it is not possible to identify a distinct oil production advantage of any of the three cases in this study.

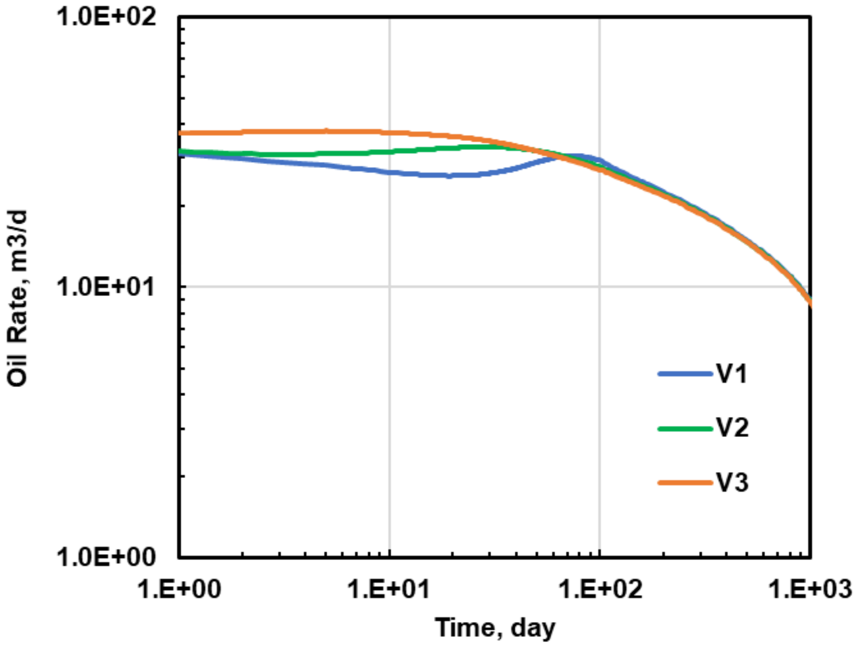

Figure 5.27 Effect of Variably-Declining BHPs on the Oil Production Rate

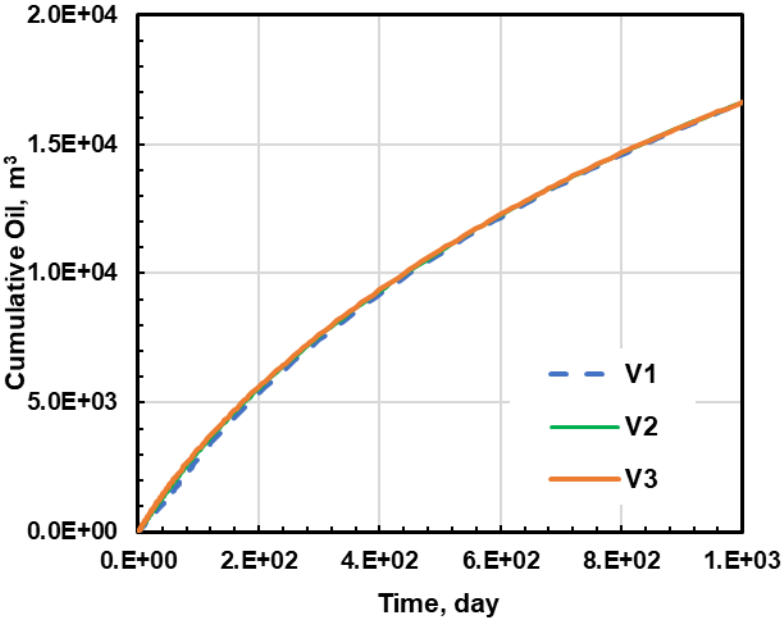

Figure 5.28 Effect of Variably-Declining BHPs on the Cumulative Oil Production

Figure 5.29 shows the pressure distribution of the three cases V1, V2 and V3 at t = 30 days, 180 days, 360 days and 3 years of production. The only time when there are significant differences in the spatial distributions of the pressures in the three cases is at t = 30 days. For t > 30 days, the differences are slight and become less pronounced as time advances. At t = 360 days and 3 years, the pressure distributions of the three cases are very similar, which explains the oil cumulative production for the 3 cases is almost the same at t = 3 years of production.

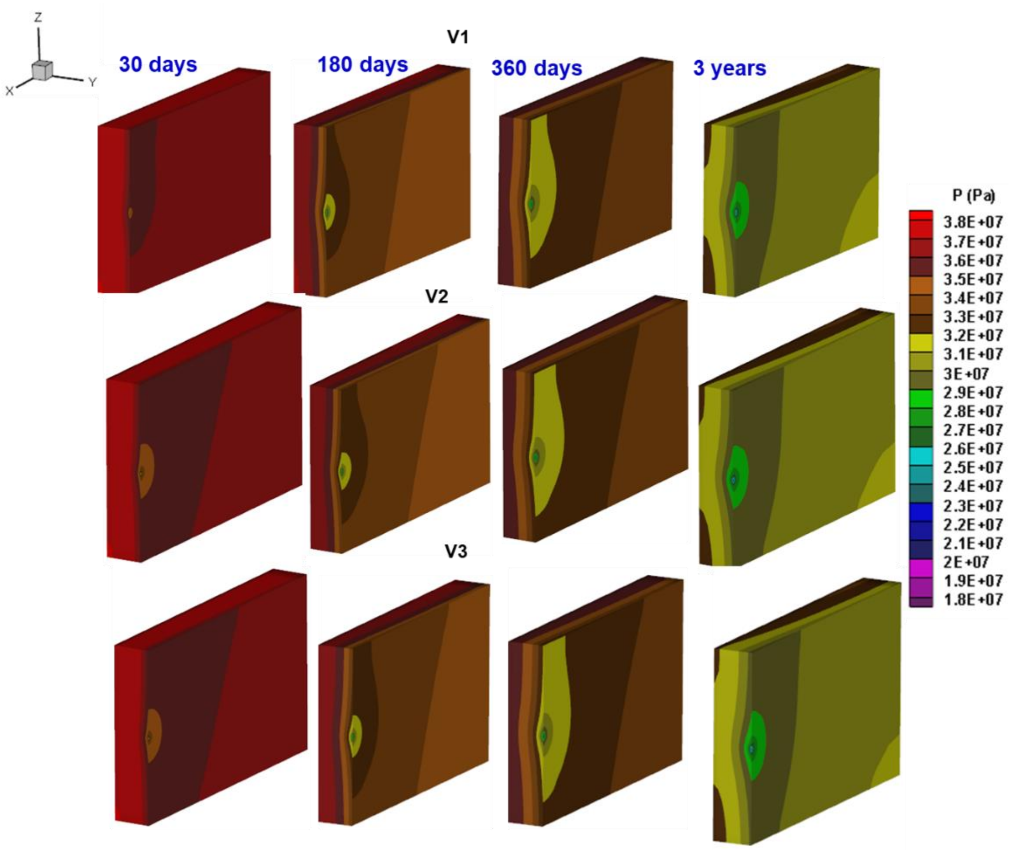

Figure 5.29 Effect of Variably-Declining BHPs on the Pressure Distribution of BHP in Variable-decline Rate Cases at *t*=30, 180, 360 Days and 3 Years from Left to Right

In **Figure 5.30**, the differences in the HF porosity in the three cases are small during the first 100 days of production, after which the HF porosity decreases at practically the same rate. At t = 3 years, the porosity is 0.21, which corresponds to a 58% reduction from its original value of 0.5.

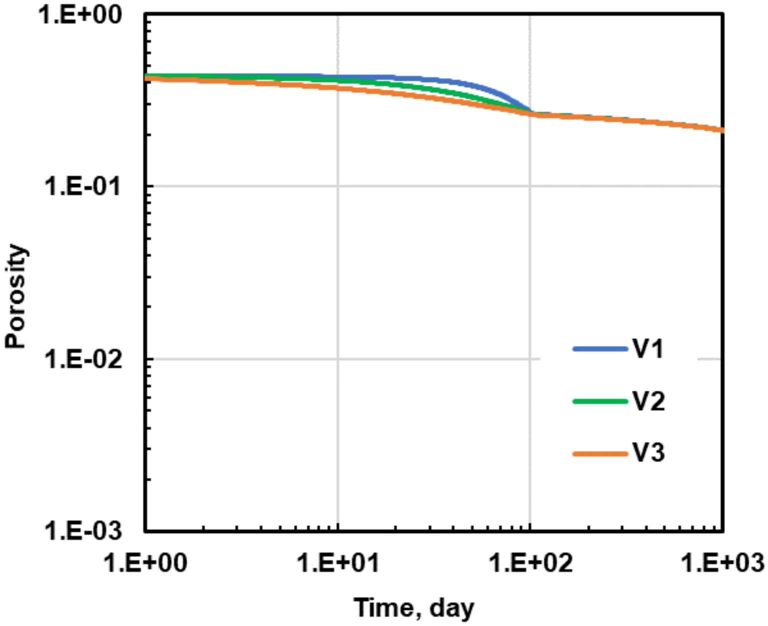

Figure 5.30 Effect of Variably-Declining BHPs on the Fracture Porosity

I also monitored the fracture permeability, shown in **Figure 5.31**. At t = 1 day, the permeability in Cases V1 and V2 are close, while the permeability in Case V3 is lower, consistent with the larger pressure drop associated with this case. The permeability pattern until t = 100 days follows the pressure pattern in the HF: the higher the pressure (*i.e.*, Case V1), the higher the fracture permeability. At t = 100 days, the HF pressures converge, and so do the HF permeabilities. Beyond that point, *i.e.*, for t > 100 days, the HF pressures in all three cases remain constant, but the corresponding HF permeabilities continue to decline and coincide to reach the 2.5×10^{-13} m^2 (0.25 Darcy) level at t = 3 years.

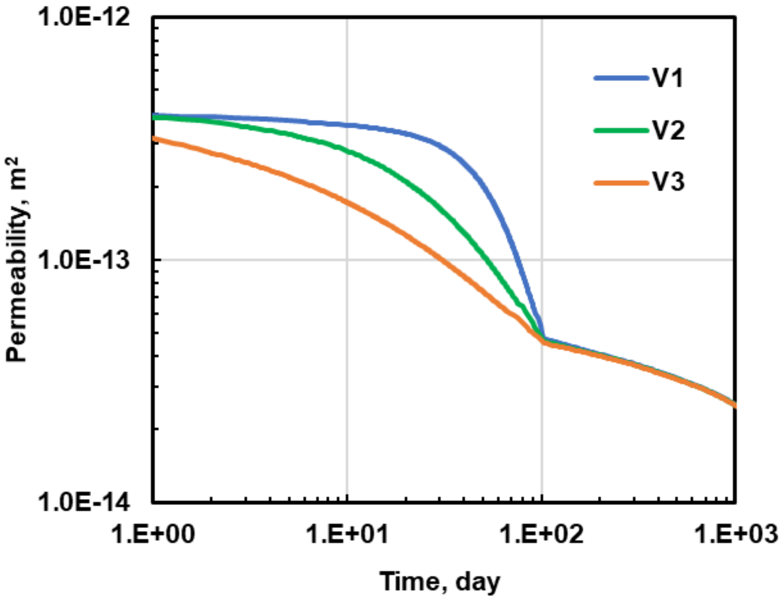

Figure 5.31 Effect of Variably Declining BHPs on the Fracture Permeability

I display the fracture aperture evolution vs. the production time in **Figure 5.32**. The evolution of the fracture apertures follows closely that of the fracture permeabilities in **Figure 5.31**: at t = 1 day the apertures in Case V1 and V2 are the same, but that in Case V3 is smaller because of the lower pressure. The decline in the apertures follows the pattern of pressure reduction (**Figure 5.26**) until the pressures and the HF apertures all coincide at t = 100 days, after which the apertures in all 3 cases continue to shrink and coincide. The strong relationship between apertures and permeability (**Figure 5.31**) is expected: the larger the aperture, the larger the HF permeability and the higher the oil production. This is certainly the case (see **Figure 5.27**) until the apertures and permeabilities in Cases V1, V2 and V3 coincide for t > 100 days, when the oil production rates also coincide. Note that the evolution of the volumetric strains in **Figure 5.33** follows a pattern that hews closely to that in **Figures 5.31** and **5.32** for obvious reasons: the reduction in the apertures is directly related to the reduction in the volumetric strains.

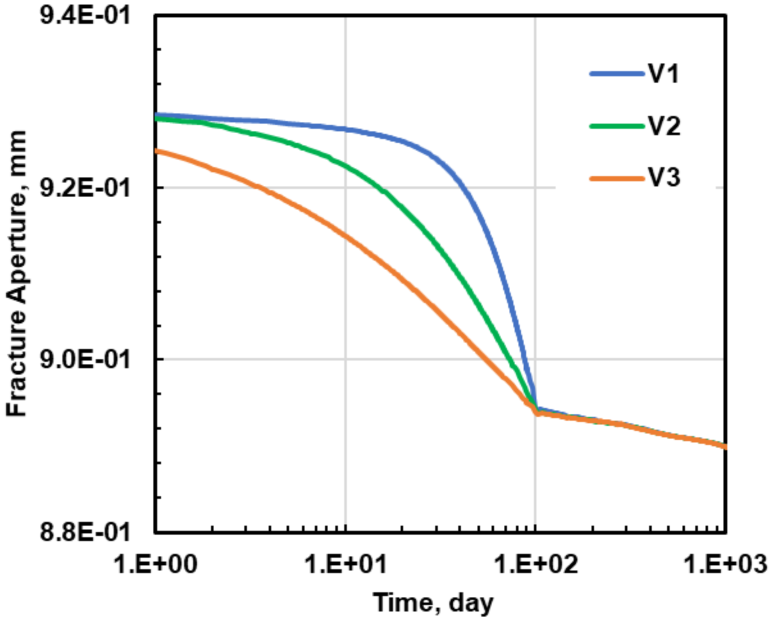

Figure 5.32 Effect of Variably Declining BHPs on the Fracture Aperture

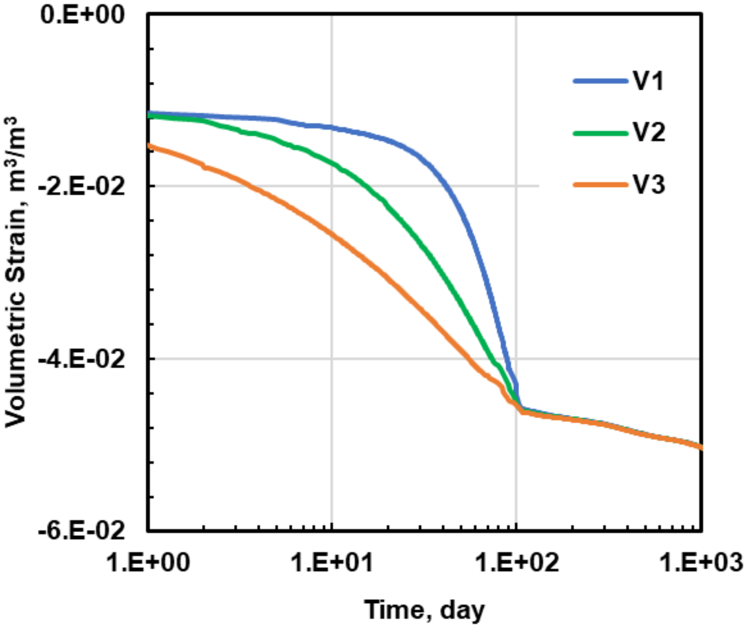

Figure 5.33 Effect of Variably-Declining BHPs on the Volumetric Strain

The conclusion to be drawn from these results is that the time-variable BHPs that I considered in Cases V1, V2 and V3 have minor effects on the long-term cumulative oil production.

5.2.5 Summary

Using high-resolution grids, I investigated numerically the effects of different drawdown strategies on the oil production rate and on the cumulative oil production and monitored the associated evolution of key flow and geomechanical properties over a production period of 3 years. I determined that the time-dependent pattern of the BHP drawdown, the level of the final BHP drawdown and the duration of the ramp-down duration are factors that will affect short- and long-term oil production: a continuous linear reduction in the BHP, a lower final BHP level and a longer duration of the ramp-down period are associated with a higher short- and long-term oil production rate and a larger cumulative oil production, thus defining the optimal production strategy.

5.3 Monitoring

To obtain a deeper understanding of the impact of the production process on the HF and the matrix, I monitored key flow and geomechanical parameters at several locations in the simulated domain. Thus, I monitored the evolution of these parameters at (a) 9 locations in the fracture (3 at the bottom, 3 at the fracture mid-height, 3 at the top) and (b) 27 locations in the matrix (9 on the matrix vertical Plane A next to the fracture, 9 on the matrix vertical Plane B in the middle of the matrix along the *y*-coordinate, 9 on the matrix vertical Plane C near the outer matrix boundary in the *y*-coordinate of the domain, *i.e.*, near the vertical plane of symmetry between 2 successive HFs). Planes A, B and C are located at a distance of 0.001 m, 5.65 m and 10.75 m, respectively, from the fracture plane. Some of the monitoring points and all the vertical planes that contain the monitoring points are shown in **Figure 5.34**. The names and coordinates of the monitoring points are listed in **Table 5.2**. The number of the location point on each plane denote the order in which they are checked and discussed.

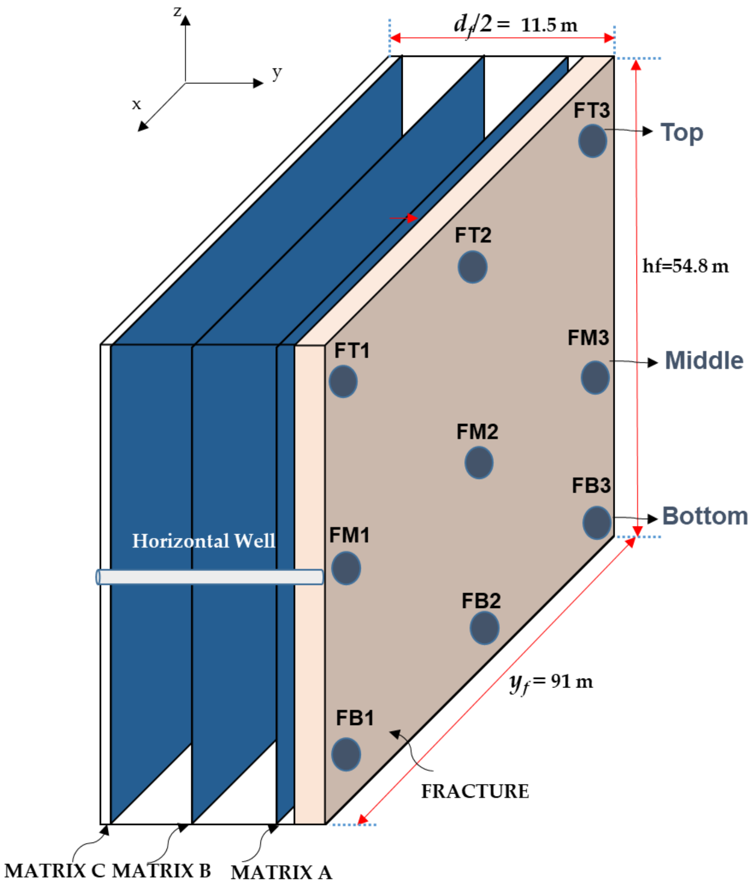

Figure 5.34 Monitoring Points in Hydraulic Fracture and Matrix

Table 5.2 The Coordinates of Monitoring Points

Planes	Points	x, m	y, m	z, m
Fracture (Bottom)	FB1	90.8	11.5	-49.4
	FB2	43.5	11.5	-49.4
	FB3	3.5	11.5	-49.4
Fracture (Middle)	FM1	90.8	11.5	-26.95
	FM2	43.5	11.5	-26.95
	FM3	3.5	11.5	-26.95
Fracture (Top)	FT1	90.8	11.5	-1.5
	FT2	43.5	11.5	-1.5
	FT3	3.5	11.5	-1.5
Matrix A (Bottom)	MAB1	90.8	11.499	-49.4
	MAB2	43.5	11.499	-49.4
	MAB3	3.5	11.499	-49.4
Matrix A (Middle)	MAM1	90.8	11.499	-26.95
	MAM2	43.5	11.499	-26.95
	MAM3	3.5	11.499	-26.95
Matrix A (Top)	MAT1	90.8	11.499	-1.5
	MAT2	43.5	11.499	-1.5
	MAT3	3.5	11.499	-1.5
Matrix B (Bottom)	MBB1	90.8	5.85	-49.4
	MBB2	43.5	5.85	-49.4
	MBB3	3.5	5.85	-49.4
Matrix B (Middle)	MBM1	90.8	5.85	-26.95
	MBM2	43.5	5.85	-26.95
	MBM3	3.5	5.85	-26.95
Matrix B (Top)	MBT1	90.8	5.85	-1.5
	MBT2	43.5	5.85	-1.5
	MBT3	3.5	5.85	-1.5
Matrix C (Bottom)	MCB1	90.8	0.75	-49.4
	MCB2	43.5	0.75	-49.4
	MCB3	3.5	0.75	-49.4
Matrix C (Middle)	MCM1	90.8	0.75	-26.95
	MCM2	43.5	0.75	-26.95
	MCM3	3.5	0.75	-26.95
Matrix C (Top)	MCT1	90.8	0.75	-1.5
	MCT2	43.5	0.75	-1.5
	MCT3	3.5	0.75	-1.5

In this study, the BHP declines linearly from P_w = 33.09 MPa (4800 psi) to P_w = 13.79 MPa (2000 psi) in 30 days, after which time BHP is kept constant at P_w = 13.79 MPa (2000 psi) until the end of production at t = 3 years. The properties and conditions used in these simulations are as listed in **Table 4.1**.

5.3.1 Monitoring Conditions in the Fracture During Production

During production, I monitor the following parameters at the 9 locations in the fracture: pressure, porosity, permeability, and fracture aperture.

Monitoring Points Near the Fracture Bottom

Figure 5.35 displays the pressure evolution at the monitoring points near the HF bottom. The pressure at points FB1, FB2 and FB3 declines from the original level of 38 MPa (5536 psi) to 29.6, 30.6 and 31.0 MPa (4293, 4438 and 4496 psi), respectively, at t = 3 years. This is consistent with expectations, as the largest pressure drop is observed at the location nearest to the horizontal well. As expected, the pressure at these points declines continuously over time: rapidly immediately after the onset of production and slower later, with the pressure decline becoming practically linear for $t \geq 600$ days. The evolution of porosity, fracture permeability and fracture aperture over time in **Figures 5.36, 5.37** and **5.38**, respectively, follow the same trend and general pattern observed in the evolution of pressure in **Figure 5.35**: continuous decline over the 3-year production period, initially rapidly and later at a slower rate. At t = 3 years, the reduction in the porosity, permeability and fracture aperture at these 3 points are significant. The permeability at points FB1, FB2 and FB3 decline from the initial value of 0.8 Darcy to 0.125, 0.156 and 0.173 Darcy, respectively, *i.e.*, a decline that is in the 80% range. The reduction in the fracture at these points is also significant, reaching as low as 0.35 at Point FB1 (closest to the horizontal well) from the original level of 0.5 and being a significant contributor to the significant reduction in the permeability discussed above.

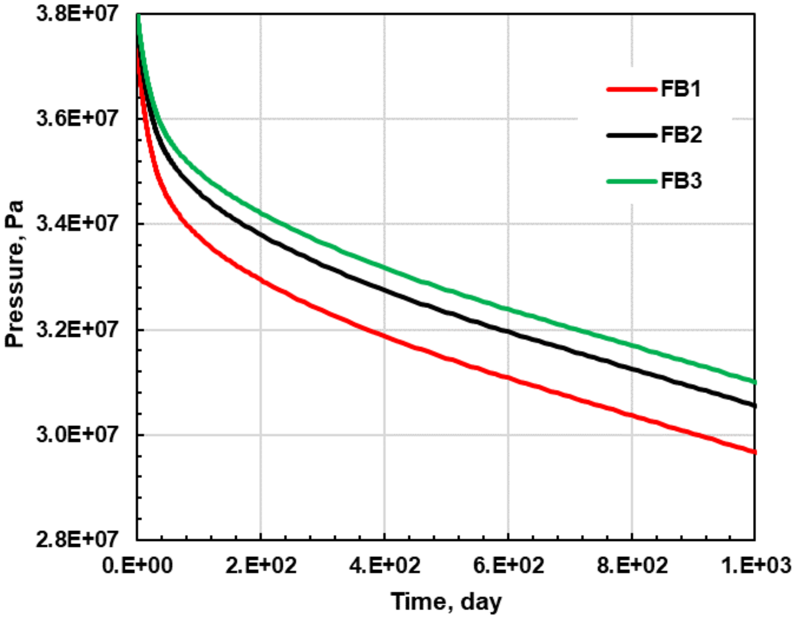

Figure 5.35 Pressure Evolution Over Time at Monitoring Points FB1, FB2 and FB3 Near the Fracture Bottom

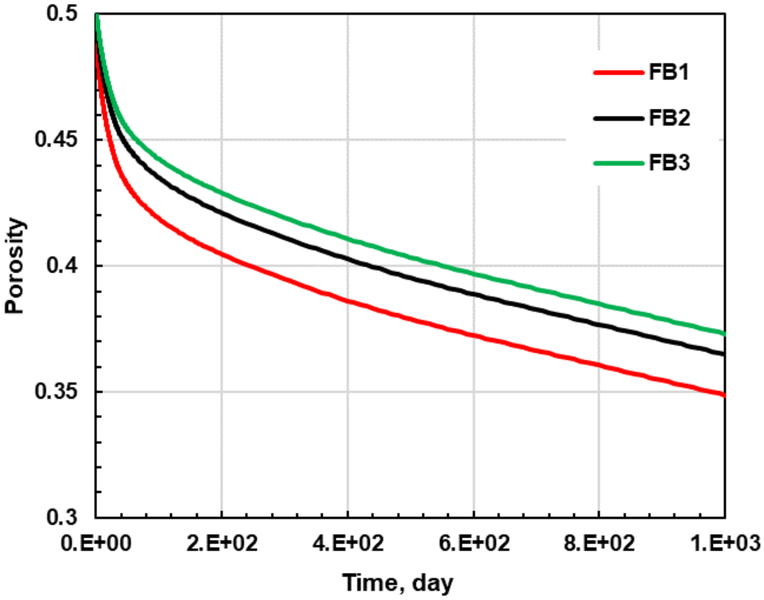

Figure 5.36 Porosity Evolution Over Time at Monitoring Points FB1, FB2 and FB3 Near the Fracture Bottom

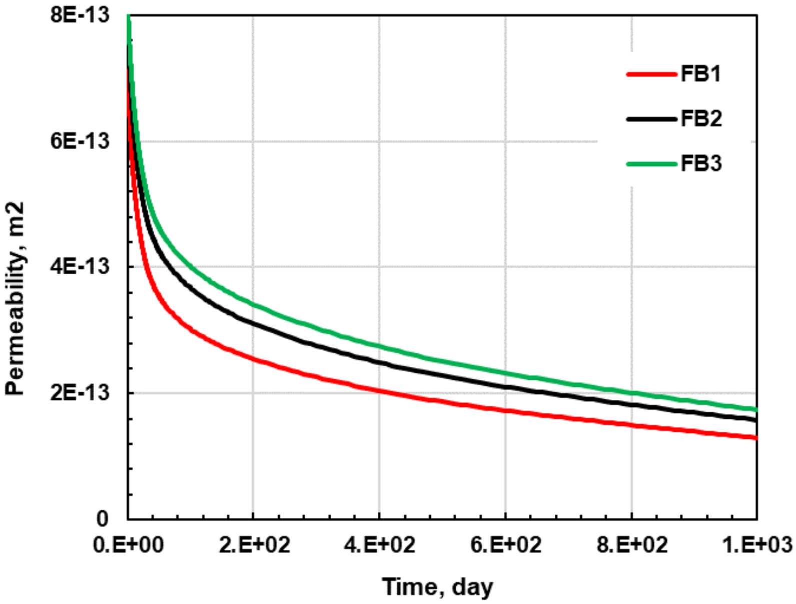

Figure 5.37 Permeability Evolution Over Time at Monitoring Points FB1, FB2 and FB3 Near the Fracture Bottom

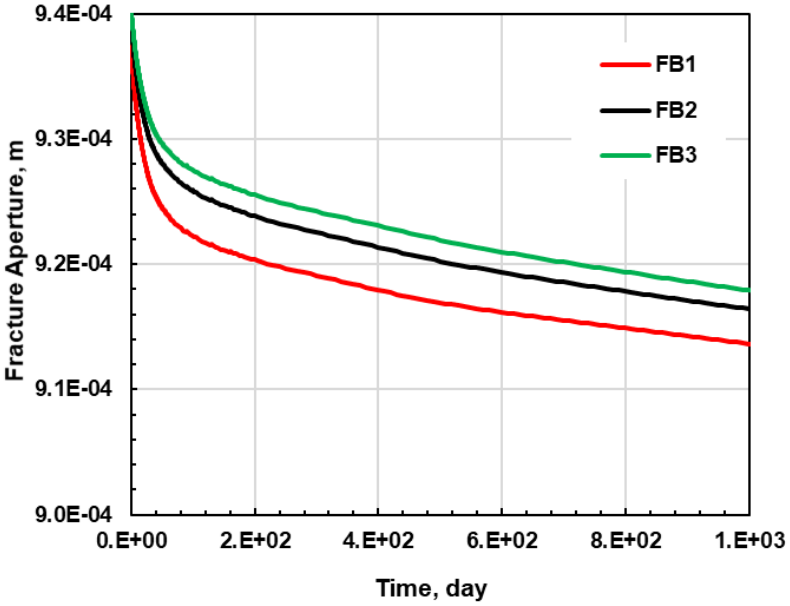

Figure 5.38 Fracture Aperture Evolution Over Time at Monitoring Points FB1, FB2 and FB3 Near the Fracture Bottom

Monitoring Points at the Fracture Mid-Height

These monitoring points (FM1, FM2 and FM3) are at the same horizontal (*x*,*y*) plane with the horizontal well at the fracture mid-height. Consistent with expectations, the evolution of pressures in **Figure 5.39** shows that point FM1, which is located the closest to the horizontal wells of all 9 monitoring locations in the fracture, experiences the largest decline to 22 MPa at t = 3 years. As expected, the pressure drops in **Figure 5.39** (a) are larger than those at the monitoring points near the fracture bottom and (b) increase with a decreasing distance from the horizontal well (although the pressures at points FM2 and FM3 are close). The porosity evolution in **Figure 5.40** shows a decline by almost 60% (from 0.5 to 0.21 at t = 3 years) at point FM1, and smaller reductions (from 0.5 to 0.36-0.37) at the other 2 points. Similarly, the evolution of permeabilities and fracture apertures in **Figures 5.41** and **5.42** show continuous declines over time, with the largest reductions occurring at point FM1, which is the closet to the wall from all 9 points in the fracture. Permeability at FM1 declines to 3x10^{-14} m^2 (0.03 D) at *t* = 3 years, representing a reduction of over 95% (and over an order of magnitude) from its original level of 8x10^{-13} m^2 (0.8 D); the reductions at FM2 and FM3 are about 80% from the original value. The reductions in the fracture apertures at the three monitoring locations in **Figure 5.42** are much smaller than those for the porosity (**Figure 5.40**), indicating that reduction in the porosities rather than in the apertures are the major contributor to the severe reductions in permeability.

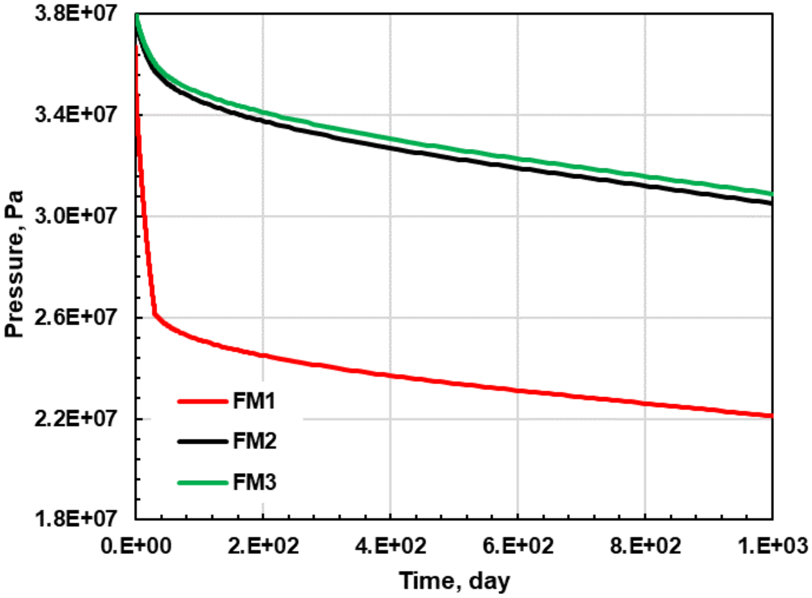

Figure 5.39 Pressure Evolution Over Time at Monitoring Points FM1, FM2 and FM3 at the Fracture Middle

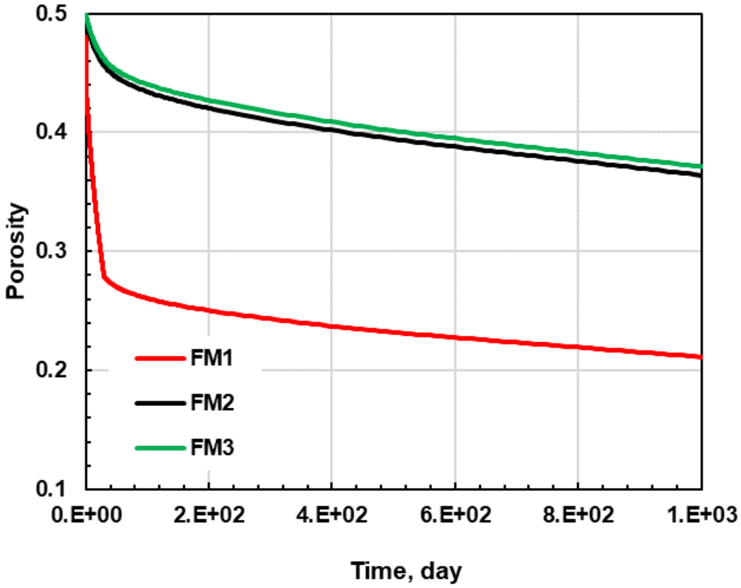

Figure 5.40 Porosity Evolution Over Time at Monitoring Points FM1, FM2 and FM3 at the Fracture Middle

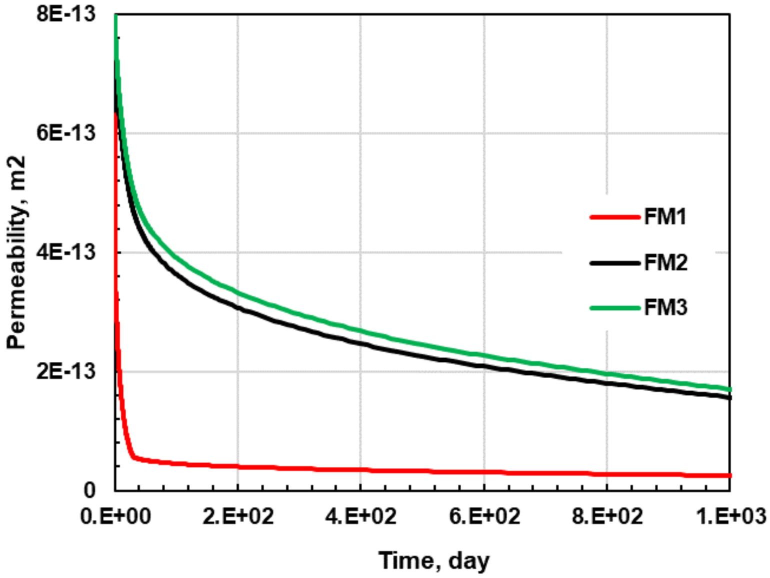

Figure 5.41 Permeability Evolution Over Time at Monitoring Points FM1, FM2 and FM3 at the Fracture Middle

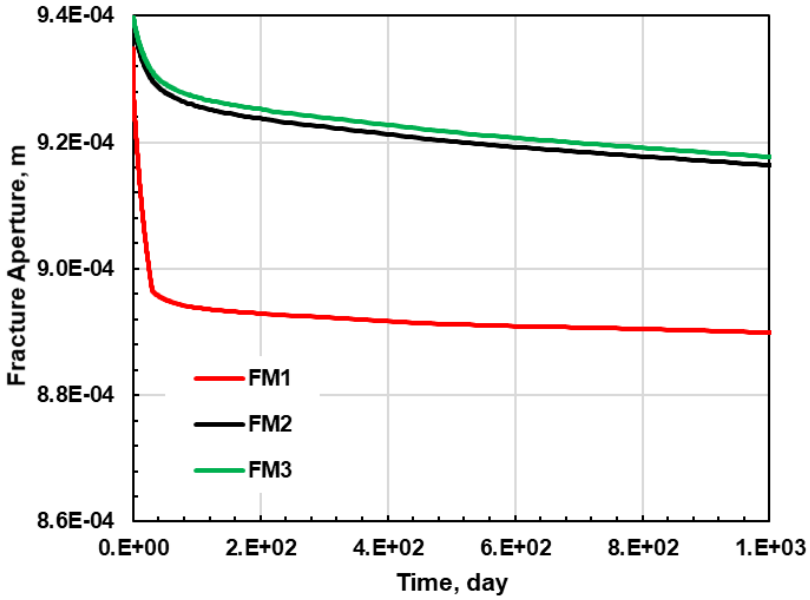

Figure 5.42 Fracture Aperture Evolution Over Time at Monitoring Points FM1, FM2 and FM3 at the Fracture Middle

Monitoring Points Near the Fracture Top

Figure 5.43 displays the pressure evolution at the monitoring points near the HF bottom. The pressure at points FT1, FT2 and FT3 declines from the original level of 38 MPa to 29.3, 30.4 and 30.8 MPa, respectively, at *t* = 3 years. This is consistent with expectations, as the largest pressure drop is observed at the point F1, which is the closest to the horizontal well. The pattern of pressure decline is very similar to the one at the monitoring points near the fracture bottom, and all the observations and conclusions discussed therein apply here. The evolutions of porosity, fracture permeability and fracture aperture over time in **Figures 5.44, 5.45** and **5.46**, respectively, follow the same trend and general pattern observed in the evolution of pressure in **Figure 5.42** (*i.e.*, continuous decline over the 3-year production period, initially rapidly and later at a slower rate) and are very similar in terms of pattern and magnitude to those at points FB1, FB2 and FB3 at the fracture bottom, so they will not be further discussed here. As before, the limited decrease in the fracture aperture leads to the conclusion that the reduction the fracture porosity is the main reason for the significant reduction in permeability at the level.

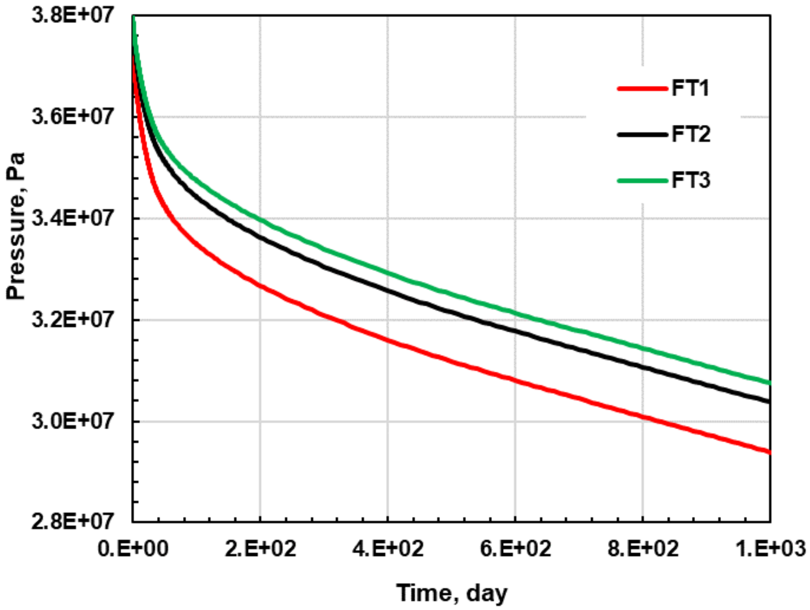

Figure 5.43 Pressure Evolution Over Time at Monitoring Points FT1, FT2 and FT3 Near the Fracture Bottom

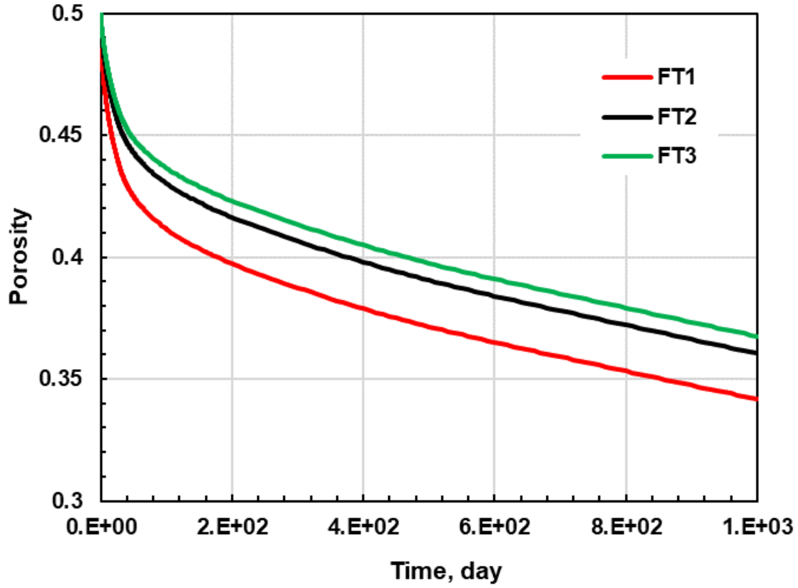

Figure 5.44 Porosity Evolution Over Time at Monitoring Points FT1, FT2 and FT3 Near the Fracture Bottom

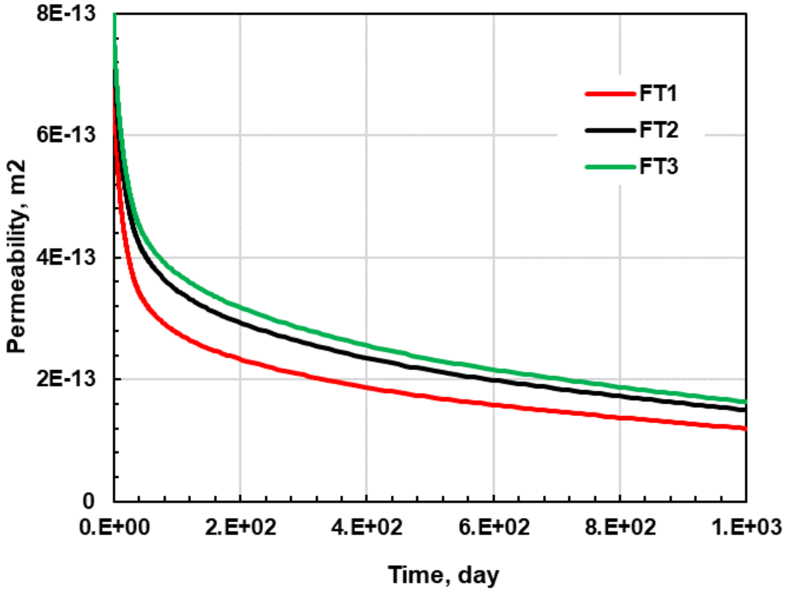

Figure 5.45 Permeability Evolution Over Time at Monitoring Points FT1, FT2 and FT3 Near the Fracture Bottom

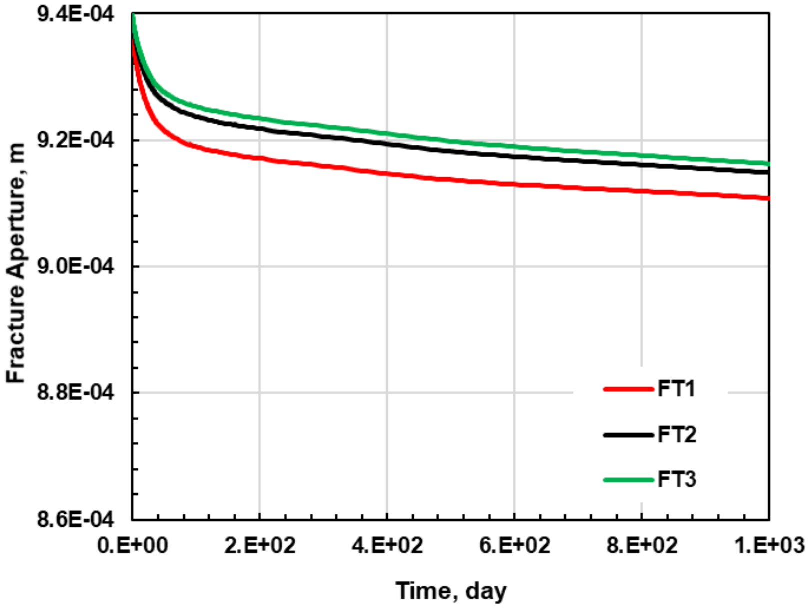

Figure 5.46 Evolution Over Time at Monitoring Points FT1, FT2 and FT3 Near the Fracture Bottom

5.3.2 Monitoring Conditions on Plane A in the Matrix

I monitored the evolution of key parameters and conditions (discussed in Section 5.3.1) at selected locations in the matrix on the vertical Plane A, *i.e.*, at a distance of 0.001m from the fracture face, as shown in **Figure 5.34.** The names and coordinates of the monitoring points are listed in **Table 5.2**.

Monitoring Points Near the Bottom of Plane A

The evolution of pressures, porosities and permeabilities at the monitoring points MAB1, MAB2 and MAB3 near the bottom of Plane B are shown in **Figures 5.47**, **5.48** and **5.49**, respectively. Compared to the corresponding points in the fracture (*i.e.*, points FB1, FB2 and FB3, see **Figures 5.35**, **5.36** and **5.37**, respectively), the inevitable observation is that the continuous decline in pressures, porosities and permeabilities follow the same patterns at the two locations. The pressures at these points in the matrix are almost the same as at the corresponding ones in the matrix, as would be expected by the close proximity of the fracture plane and Plane A (0.0015 m apart). Conversely, the magnitude of the reductions in porosity and permeability on a per-cent basis over the 3-year production period is much smaller in the matrix. This is caused by the much lower pore compressibility and c-factor (see **Eq. (4.11)**) in the matrix, which lead to milder reductions in the porosity (maximum 2%) in the and, consequently, in the permeability (maximum 11%) at these locations.

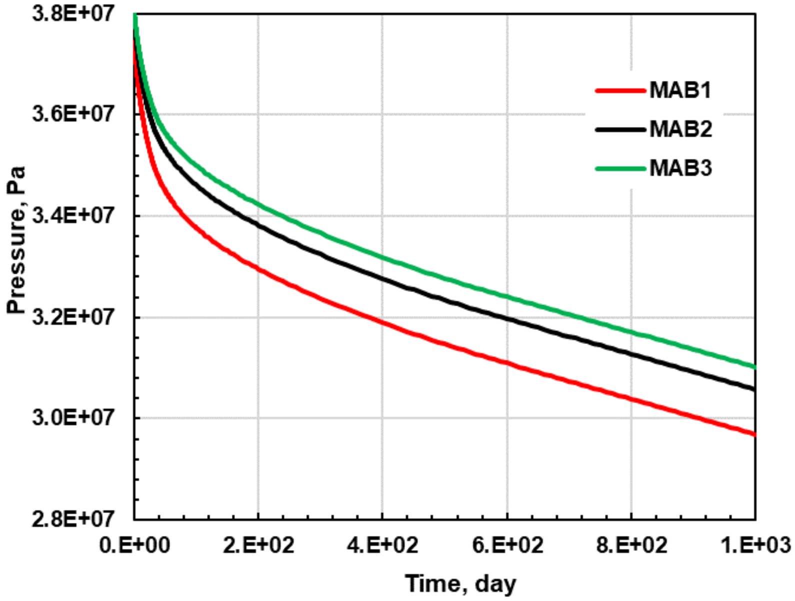

Figure 5.47 Pressure Evolution Over Time at Monitoring Points MAB1, MAB2 and MAB3 Near the Bottom of Plane A

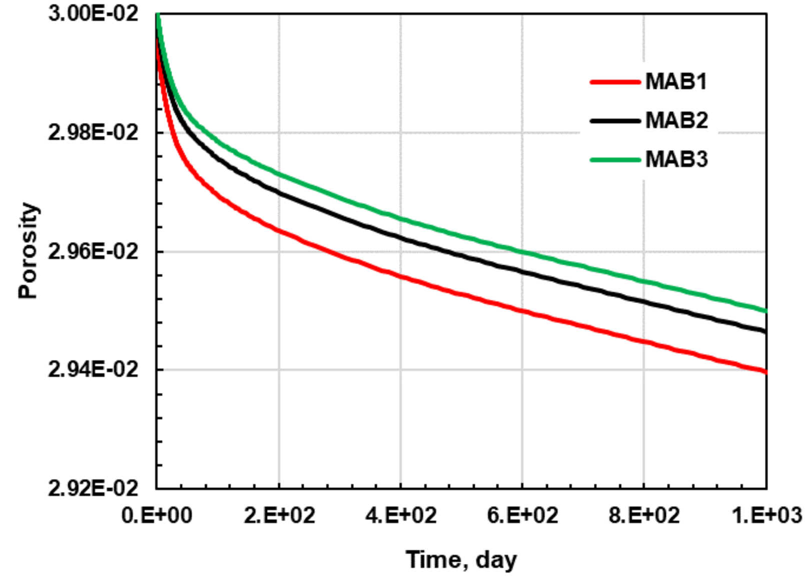

Figure 5.48 Porosity Evolution Over Time at Monitoring Points MAB1, MAB2 and MAB3 Near the Bottom of Plane A

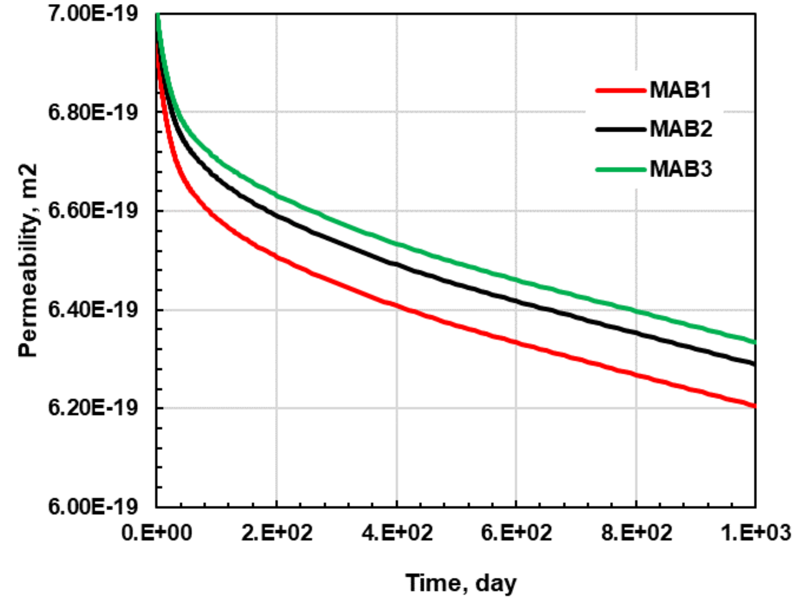

Figure 5.49 Permeability Evolution Over Time at Monitoring Points MAB1, MAB2 and MAB3 Near the Bottom of Plane A

The evolution of pressures, porosities and permeabilities at the monitoring points MAM1, MAM2 and MAM3 at the mid-height of Plane B are shown in **Figures 5.50**, **5.51** and **5.52**, respectively. Compared to the corresponding points in the fracture (*i.e.*, points FM1, FM2 and FM3, see **Figures 5.39**, **5.40** and **5.41**, respectively), the inevitable observation is that the continuous decline in pressures, porosities and permeabilities follow the same patterns at the two locations. The pressures at these points in the matrix are almost the same in pattern and values as at the corresponding ones in the matrix, and exhibit the largest pressure drop of all matrix points because of their proximity to the horizontal well. The similarity (if not coincidence) of the pressures at these monitoring locations on Plane A and the fracture plane was almost inevitable, given the minimal separation of the planes (0.0015 m). As was the case at the base of Plane A, the reductions in the porosity and permeability on a per-cent basis over the 3-year production period was much smaller at these locations in the matrix for reasons already explained, but larger than those at points MAB1, MAB2 and MAB3. Thus, the maximum porosity reduction at point MAM1 was by 3.6% compared to the original, and the maximum reduction in permeability at the same point was by almost 20%. These results and those from the bottom of Plane A appear to indicate that the permeability changes in the matrix are very mild despite low BHPs, and that the main culprit for possible reduction in production from shale oil reservoirs would be the very significant reduction in the fracture permeability caused by the BHP imposed at the horizontal well. The obvious conclusion is that strategies to maximize production from these reservoirs should aim to minimize the effect of depressurization on the permeability of the proppant-filled hydraulic facture, either by means of BHP management or (if possible) through appropriate stimulation methods that yield low-compressibility proppant-filled hydraulic fractures.

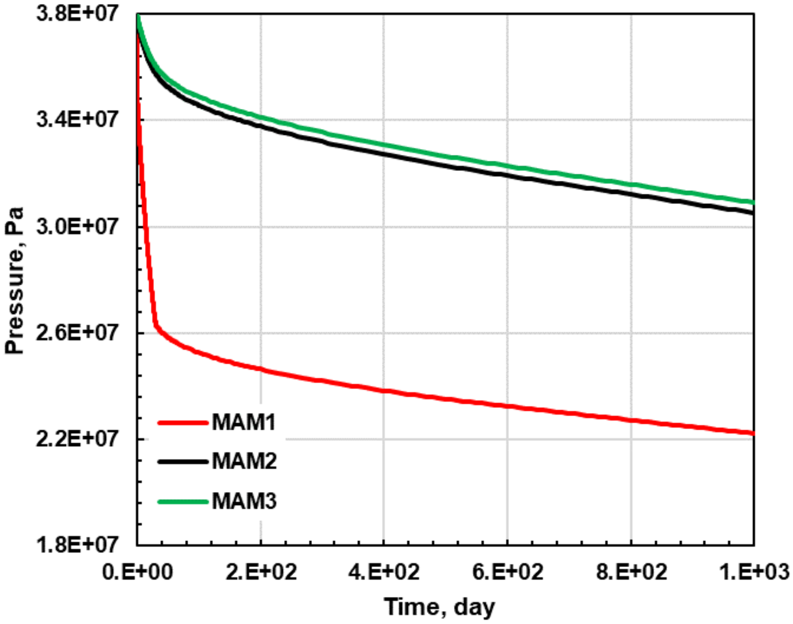

Figure 5.50 Pressure Evolution Over Time at Monitoring Points MAM1, MAM2 and MAM3 at the Mid-Height of Plane A

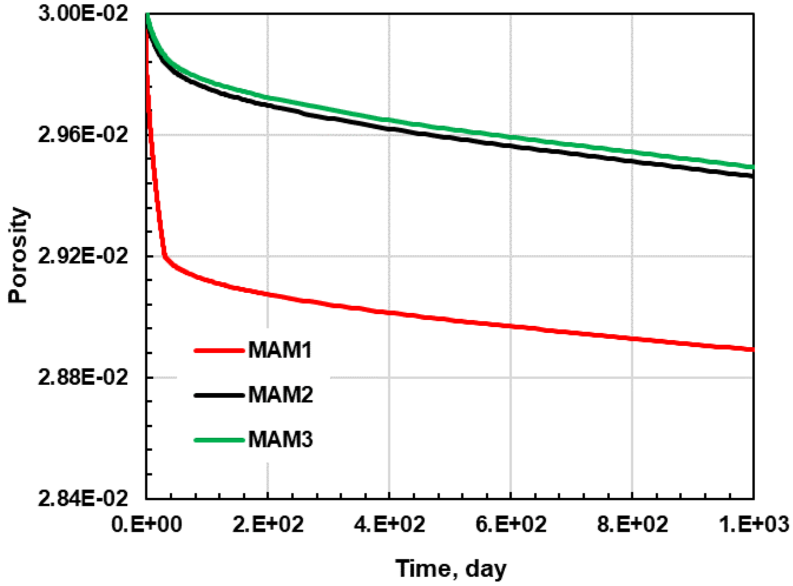

Figure 5.51 Porosity Evolution Over Time at Monitoring Points MAM1, MAM2 and MAM3 at the Mid-Height of Plane A

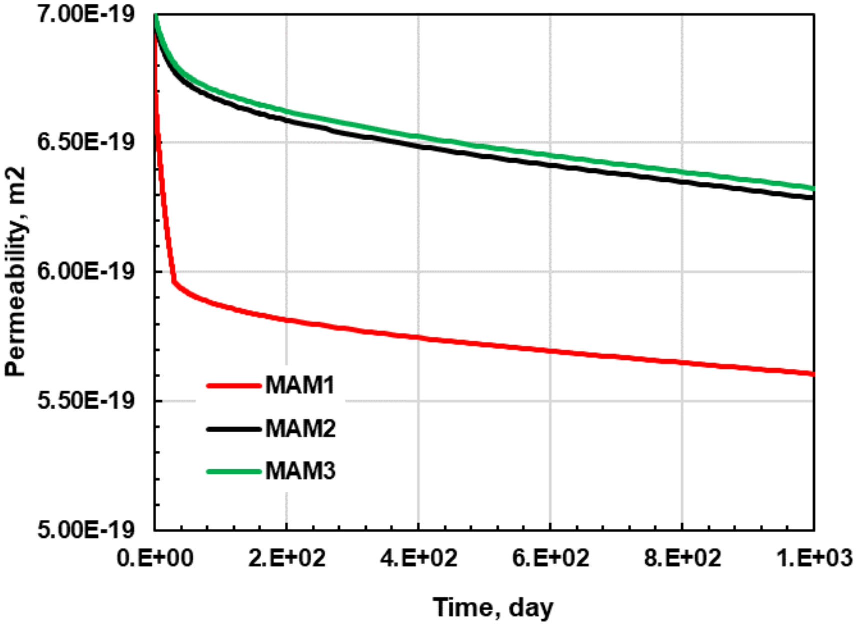

Figure 5.52 Permeability Evolution Over Time at Monitoring Points MAM1, MAM2 and MAM3 at the Mid-Height of Plane A

Monitoring Points Near the Top of Plane A

As for the top part of matrix next to fracture, the declining rates of grid 7, 8 and 9 are slower than grid 4. **Figure 5.53** exhibits the pressure evolution of top part of matrix next to fracture. The grid 7 is closer to the well grid. We observe the pressure of grid 7 declines more quickly than two other grids. At 3 years, the pressure of grid 7 is 29.4 MPa and the two other values are 30.4 and 30.7 MPa. **Figures 5.54** and **5.55** show the porosity and permeability evolution of top part of matrix next to fracture. During 3 years of production, porosity and permeability decreases less than that of middle part of matrix next to fracture. The porosity of grid 7, 8, 9 are 0.0293, 0.0294 and 0.095, respectively. And the permeability of grid 7, 8, 9 are 614, 619 and 625 nano Darcy at 3 years.

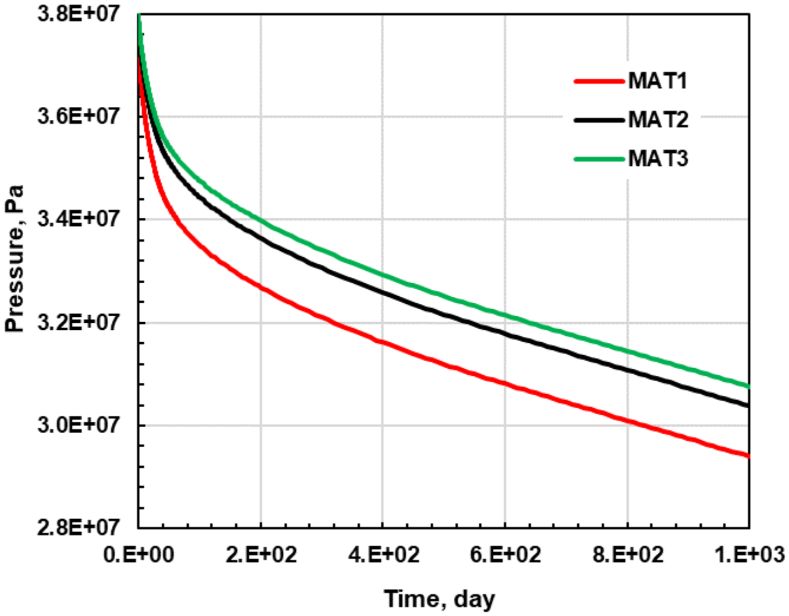

Figure 5.53 Pressure Evolution Over Time at Monitoring Points MAT1, MAT2 and MAT3 at the Mid-Height of Plane A

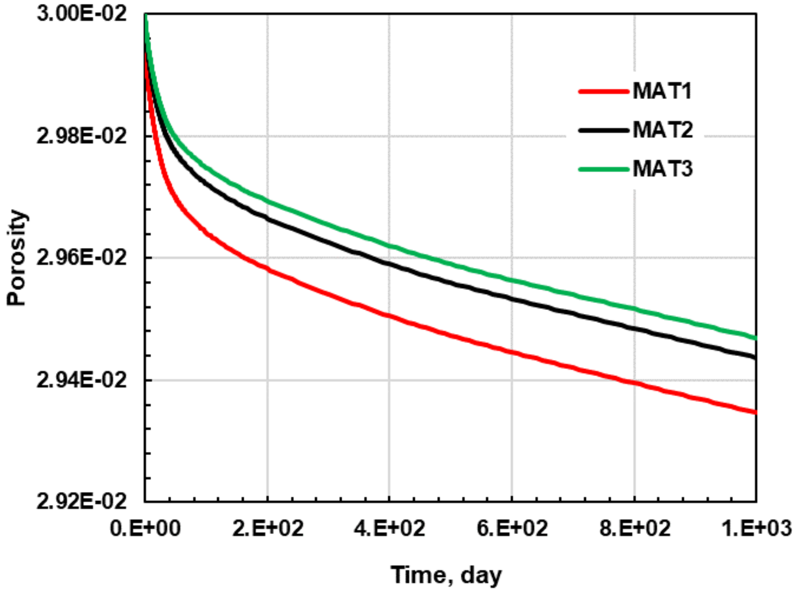

Figure 5.54 Porosity Evolution Over Time at Monitoring Points MAT1, MAT2 and MAT3 at the Mid-Height of Plane A

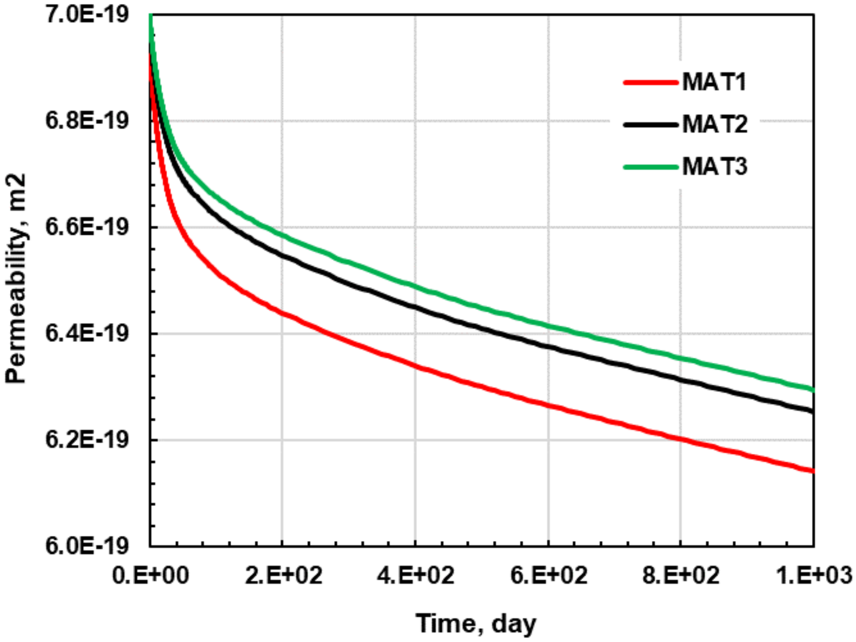

Figure 5.55 Permeability Evolution Over Time at Monitoring Points MAT1, MAT2 and MAT3 at the Mid-Height of Plane A

5.3.3 Monitoring Conditions on Plane B in the Matrix

I monitored the evolution of key parameters and conditions (discussed in Section 5.3.1) at selected locations in the matrix on the vertical Plane B, located at a distance of 5.559 m from the fracture face, as shown in **Figure 5.34**. The names and coordinates of the monitoring points are listed in **Table 5.2**.

Monitoring Points Near the Bottom of Plane B

The evolution of pressures, porosities and permeabilities at the monitoring points MBB1, MBB2 and MBB3 near the bottom of Plane B are shown in **Figures 5.56**, **5.57** and **5.58**, respectively. The evolution of pressures over time follow a predictable and expected pattern: despite the BHP-induced depressurization and continuous production, the pressure did not change from its initial level for about 20-30 days because of the distance of these points from the HW. After that time, the pressure began to decline as depressurization and production continued. The maximum pressure drop (to 31.6 MPa, *i.e.,* a 16.8% reduction from the original) was observed at point MBB1, which was closest to the HW; the closer to the well, the larger the pressure drop at any time after the initial delay. The pattern of the declines in the porosities and permeabilities (**Figures 5.57** and **5.58**) at the 3 observation points followed very closely the pressure decline patterns in **Figure 5.56**. The declines in porosity and permeability were very mild: the minimum porosity at point MBB1 at t = 3 years was 0.0295 (*i.e.,* a reduction by 1.7% from the original), and the minimum permeability at the same point and time was

6.38×10^{-19} m^2 (638 nD, *i.e.*, a reduction by 8.9% from the original). Such reductions are not expected to have a pronounced effect on production.

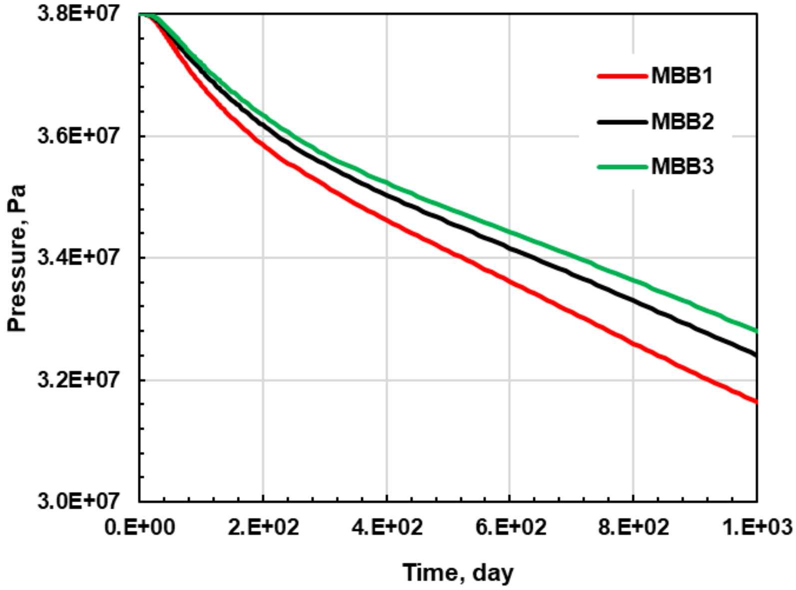

Figure 5.56 Pressure Evolution Over Time at Monitoring Points MBB1, MBB2 and MBB3 Near the Bottom of Plane B

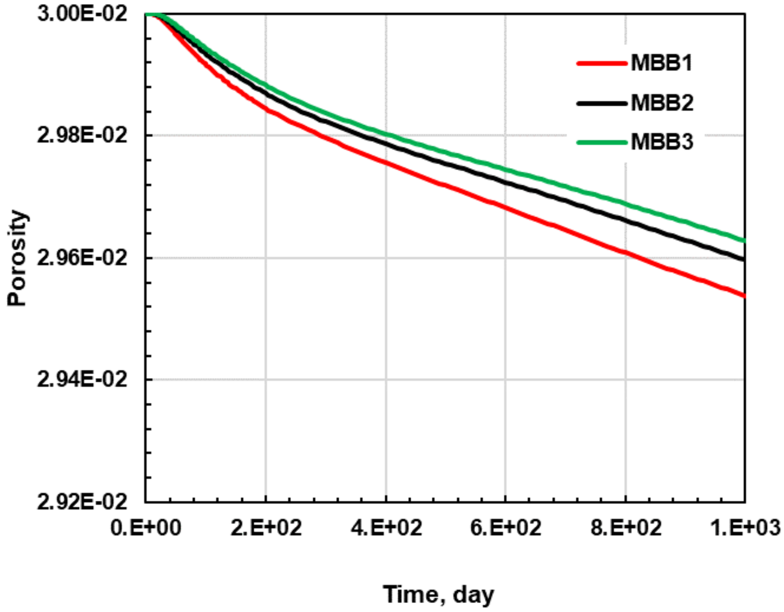

Figure 5.57 Porosity Evolution Over Time at Monitoring Points MBB1, MBB2 and MBB3 Near the Bottom of Plane B

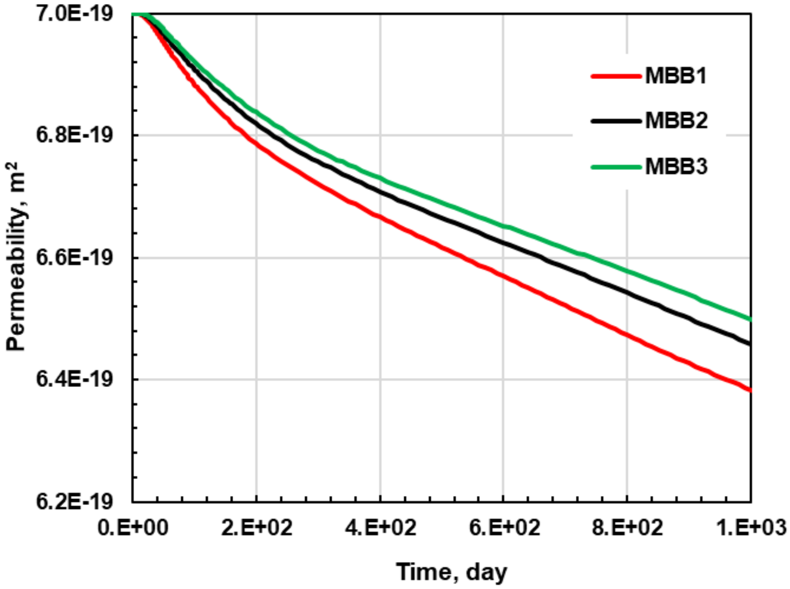

Figure 5.58 Permeability Evolution Over Time at Monitoring Points MBB1, MBB2 and MBB3 Near the Bottom of Plane B

Monitoring Points at Mid-Height of Plane B

The same general observations made in the discussion of the monitoring results at the base of Plane B apply to the evolution of pressures, porosities and permeabilities at the monitoring points MBM1, MBM2 and MBM3 at the mid-height of Plane B (shown in **Figures 5.59**, **5.60** and **5.61**, respectively). There were delays in the onset of pressure decline at these points, but these were shorter than those at the base of Plane B because of the shorter distance of these points from the HW. After the initial delay, at any time (a) all the observed pressures declined continuously and (b) the closer to the well, the larger the pressure drop. Because of its shortest distance from the horizontal well, point MBM1 showed the largest pressure drop (to 30.8 MPa, by 18.9% from the original) of all the points on Plane B. As in every case in this study, the pattern of the declines in the porosities and permeabilities (**Figures 5.60** and **5.61**) at the monitoring points MBM1, MBM2 and MBM3 followed very closely the pressure decline patterns in **Figure 5.59**. The declines in porosity and permeability were again mild: the minimum porosity at point MBM1 at t = 3 years was 0.0295 (*i.e.*, a reduction by 1.7% from the original), and the minimum permeability at the same point and time was 6.30×10^{-19} m^2 (630 nD, *i.e.*, a reduction by 10.0% from the original). Such reductions are not expected to have a pronounced effect on production.

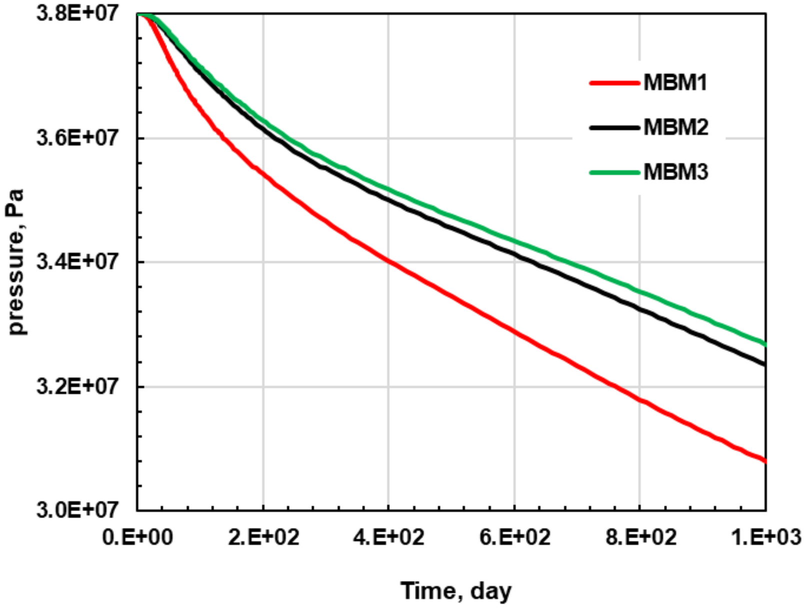

Figure 5.59 Pressure Evolution Over Time at Monitoring Points MBM1, MBM2 and MBM3 at the Mid-Height of Plane B

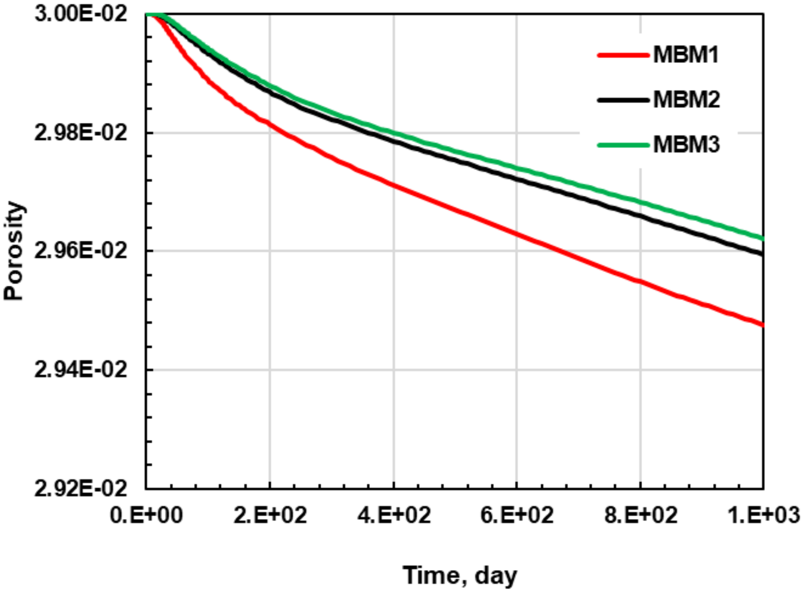

Figure 5.60 Porosity Evolution of Over Time at Monitoring Points MBM1, MBM2 and MBM3 at the Mid-Height of Plane B

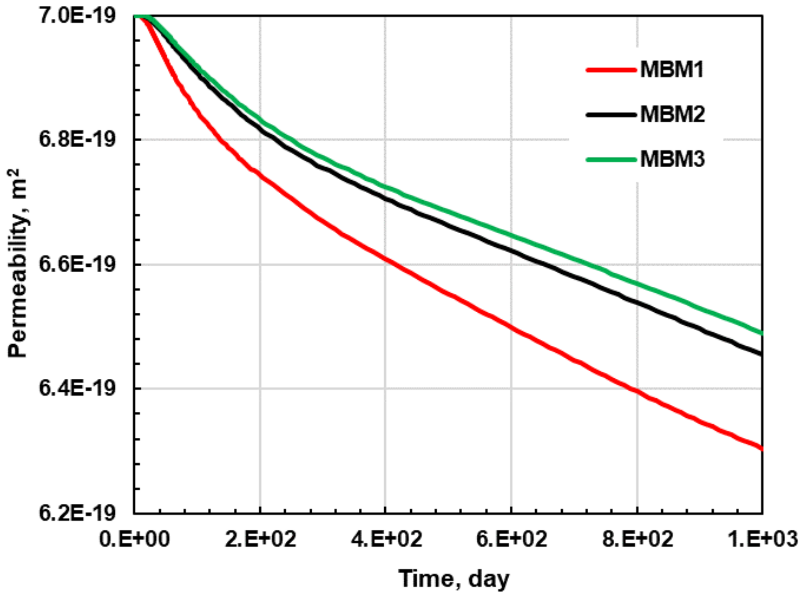

Figure 5.61 Permeability Evolution Over Time at Monitoring Points MBM1, MBM2 and MBM3 at the Mid-Height of Plane B

Monitoring Points Near the Top of Plane B

The same general observations made in the discussion of the monitoring results at the base and at the mid-height of Plane B apply to the evolution of pressures, porosities and permeabilities at the monitoring points MBT1, MBT2 and MBT3 near the top of Plane B (shown in **Figures 5.62**, **5.63** and **5.64**, respectively). There were delays in the onset of pressure decline at these points that are similar to, but slightly lower than, those near the base of Plane B. The lower pressures that were observed consistently at the monitoring points near the top of all observation planes (HF, A, B and C) are consistent with the effects of gravity. After the initial delay, at any time (a) all the observed pressures declined continuously and (b) the pressure drop decreased with an increasing distance from the HW. Thus, the largest pressure drop (to 31.4 MPa, *i.e.*, by 17.4% from the original) was observed at point MBT1, which was the closest to the HW. As in every case in this study, the pattern of the declines in the porosities and permeabilities (**Figures 5.63** and **5.64**) at the monitoring points MBT1, MBT2 and MBT3 followed very closely the pressure decline patterns in **Figure 5.62**. The declines in porosity and permeability are again mild: the minimum porosity at point MBT1 at t = 3 years is 0.0295 (*i.e.*, a reduction by 1.7% from the original), and the minimum permeability at the same point and time is 6.34×10^{-19} m^2 (634 nD, *i.e.*, a reduction by 9.4% from the original). As indicated earlier, such reductions are not expected to have a pronounced effect on production.

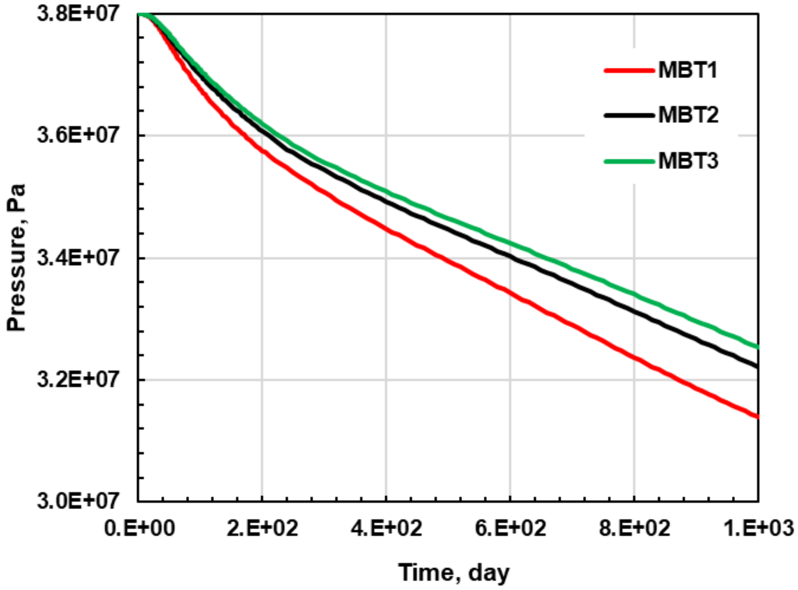

Figure 5.62 Pressure Evolution Over Time at Monitoring Points MBT1, MBT2 and MBT3 Near the Top of Plane B

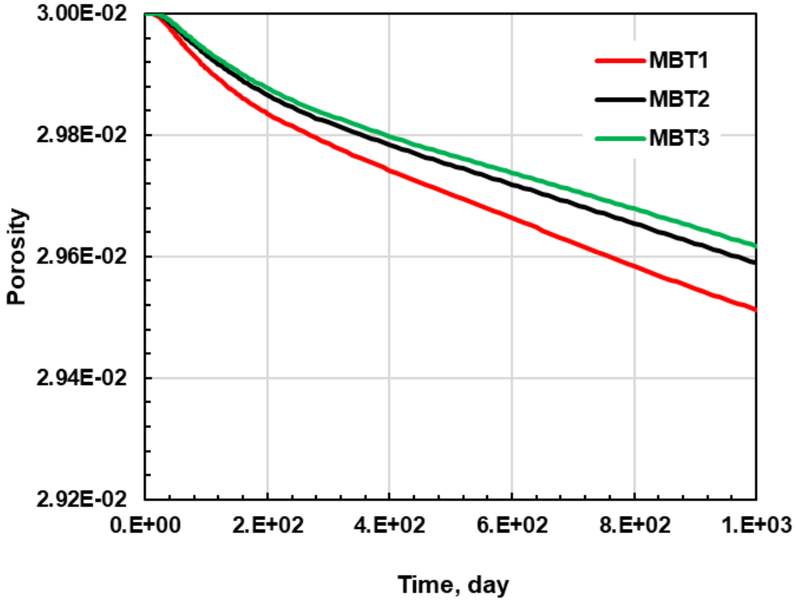

Figure 5.63 Porosity Evolution Over Time at Monitoring Points MBT1, MBT2 and MBT3 Near the Top of Plane B

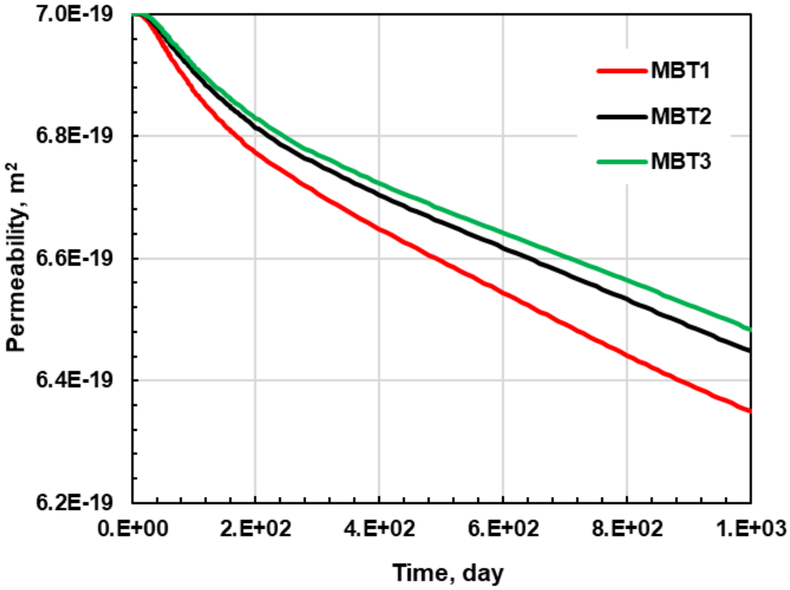

Figure 5.64 Permeability Evolution Over Time at Monitoring Points MBT1, MBT2 and MBT3 Near the Top of Plane B

5.3.4 Monitoring Conditions on Plane C in the Matrix

I monitored the evolution of key parameters and conditions (discussed in Section 5.3.1) at selected locations in the matrix on the vertical Plane C, located at a distance of 11.49 m from the fracture face, as shown in **Figure 5.34**. The names and coordinates of the monitoring points are listed in **Table 5.2**

Monitoring Points Near the Bottom of Plane C

The evolution of pressures, porosities and permeabilities at the monitoring points MCB1, MCB2 and MCB3 near the bottom of Plane C are shown in **Figures 5.65**, **5.66** and **5.67** respectively. The evolution of pressures over time follow a predictable and expected pattern: despite the BHP-induced depressurization and continuous production, the pressure did not change from its initial level for about 50-60 days because of the distance of these points from the HW. After that time, the pressure began to decline as depressurization and production continued, but the pressure drop occurs at a much slower rate and results in significantly higher final pressures at *t* = 3 years because of the larger distance of plane C from the HW (compared to all the HF, A and B planes) and the very low permeability of the matrix. The maximum pressure drop (to 32.4 MPa, *i.e.*, a 14.7% reduction from the original) was observed at point MCB1, which was closest to the HW; the closer to the well, the larger the pressure drop at any time after the initial delay. Note the change in the slope of the pressure vs. time curves at *t* = 316, 400 and 420 days at points MCB1, MCB2 and MCB3, respectively, denoting a transition of the flow regime as the pressure wave arrives at the non-flow boundary of the domain. The pattern of the declines in the porosities and permeabilities (**Figures 5.66** and **5.67**) at the 3 observation points followed closely the pressure decline patterns in Figure 5.65. The declines in porosity and permeability were very mild: the minimum porosity at point MBB1 at *t* = 3 years was 0.0296 (*i.e.*, a reduction by 1.3% from the original), and the minimum permeability at the same point and time was 6.44x10^{-19} m^2 (644 nD, *i.e.*, a reduction by 7.9% from the original).

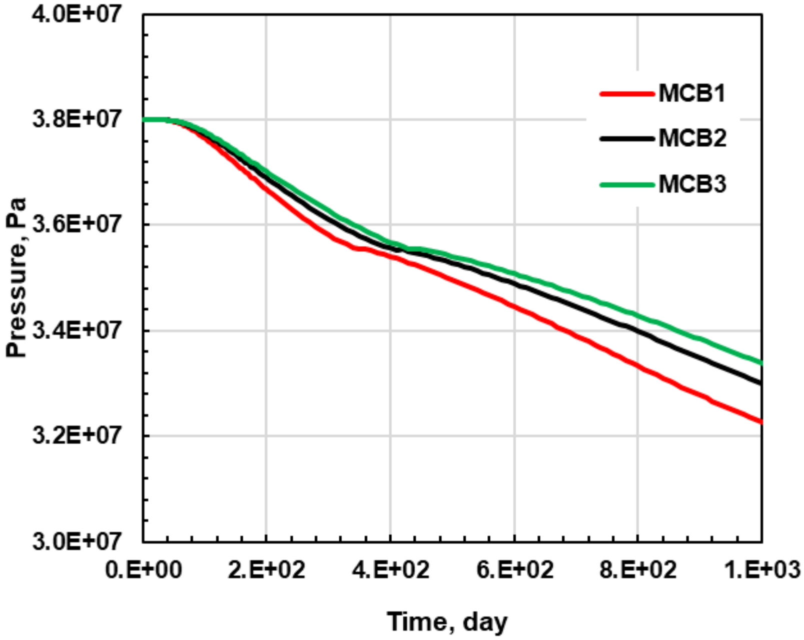

Figure 5.65 Pressure Evolution Over Time at Monitoring Points MCB1, MCB2 and MCB3 Near the Bottom of Plane C

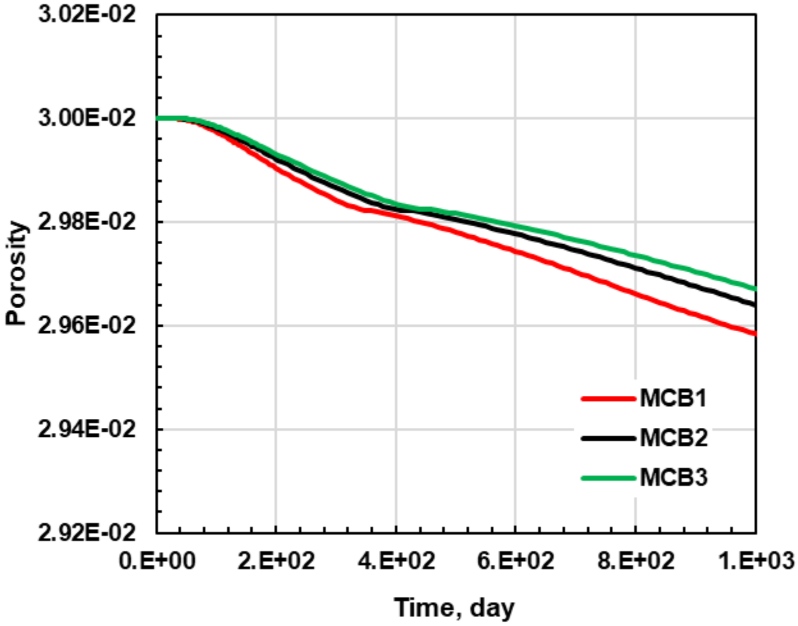

Figure 5.66 Porosity Evolution Over Time at Monitoring Points MCB1, MCB2 and MCB3 Near the Bottom of Plane C

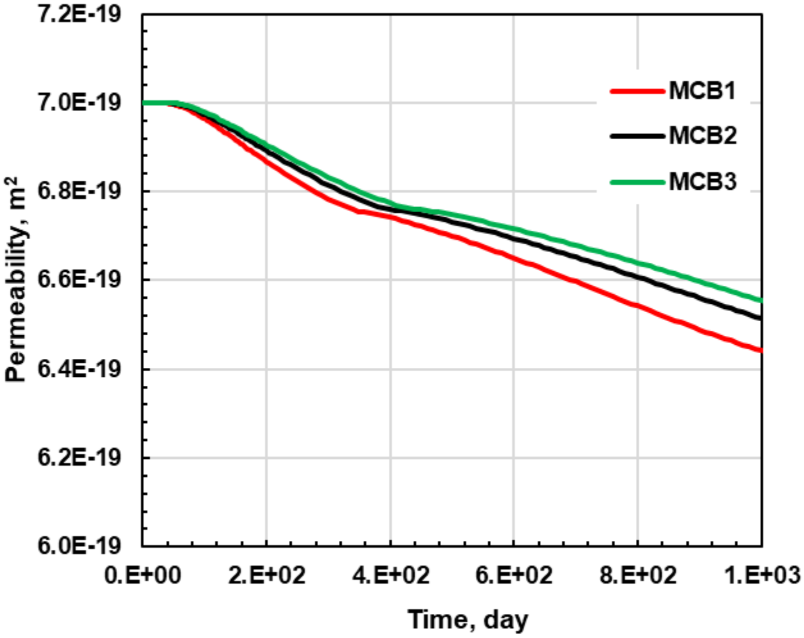

Figure 5.67 Permeability Evolution Over Time at Monitoring Points MCB1, MCB2 and MCB3 Near the Bottom of Plane C

Monitoring Points at the Mid-Height of Plane C

The same general observations made in the discussion of the monitoring results at the base of Plane C, as well as at the mid-height of all planes, apply to the evolution of pressures, porosities and permeabilities at the monitoring points MCM1, MCM2 and MCM3 at the mid-height of Plane C (shown in **Figures 5.68**, **5.69** and **5.70**, respectively). Consistent with the observations of the monitoring points at the mid-height on all planes, the pressure drop at point MCM1 is the largest of all points on this plane (to 31.6 MPa, *i.e.*, a 16.8% reduction from the original) because of its shortest distance from the HW. Because the distance of Plane C from the HW is the largest of the 4 planes, the reductions in all the monitored parameters (pressures, porosities and permeabilities) at points MCM1, MCM2 and MCM3 are the smallest of all points at the same elevation. For reasons already discussed, the reductions in porosity and permeability were again mild: the minimum porosity at point MBM1 at t = 3 years was 0.0295 (*i.e.*, a reduction by 1.7% from the original), and the minimum permeability at the same point and time was 6.40×10^{-19} m^2 (640 nD, *i.e.*, a reduction by 8.6% from the original).

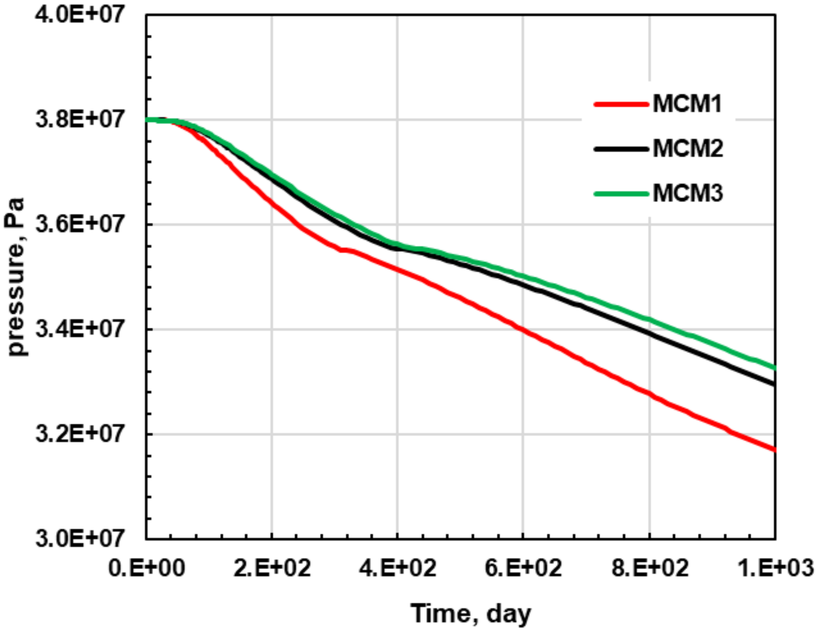

Figure 5.68 Pressure Evolution Over Time at Monitoring Points MCM1, MCM2 and MCM3 at the Mid-Height of Plane C

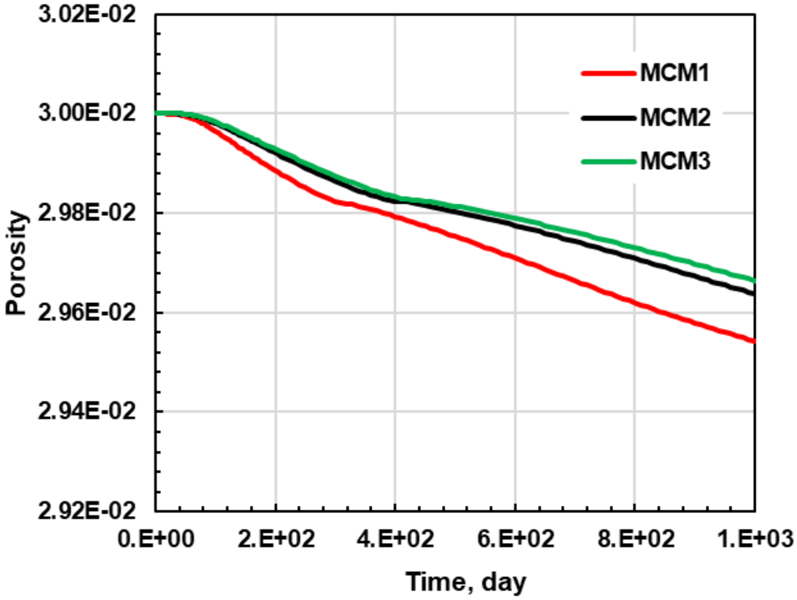

Figure 5.69 Porosity Evolution Over Time at Monitoring Points MCM1, MCM2 and MCM3 at the Mid-Height of Plane C

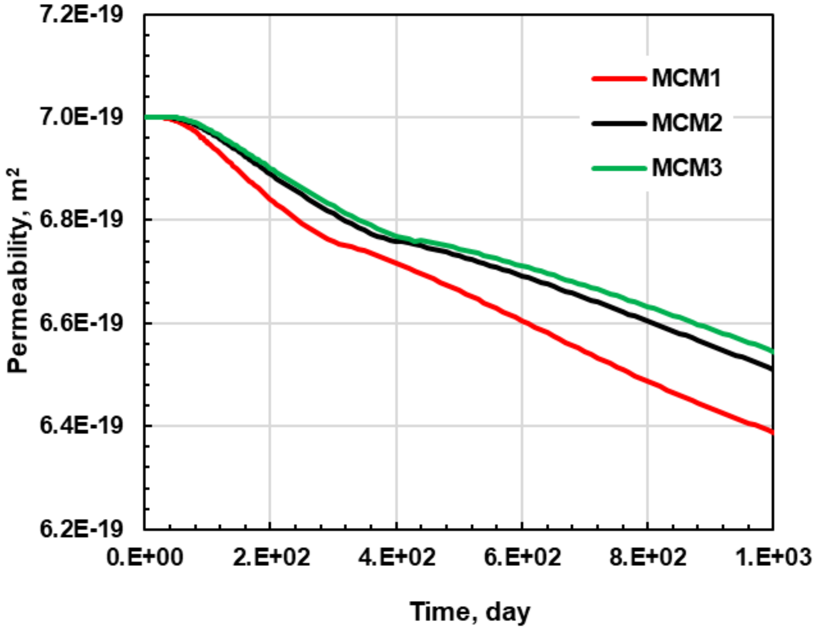

Figure 5.70 Permeability Evolution Over Time at Monitoring Points MCM1, MCM2 and MCM3 at the Mid-Height of Plane C

Monitoring Points Near the Top of Plane C

The same general observations made in the discussion of the monitoring results at the base and at the mid-height of Plane C apply to the evolution of pressures, porosities and permeabilities at the monitoring points MCT1, MCT2 and MCT3 near the top of Plane B (shown in **Figures 5.71**, **5.72** and **5.73**, respectively). These figures are very similar to those obtained at the monitoring points MCB1, MCB2 and MCB3 near the base of Plane C (see **Figures 5.65**, **5.66** and **5.67**, respectively) for reason already explained, with the only difference being the slightly larger pressure drops, and, consequently, the marginally larger decline in the porosity and permeabilities at these points. Because of the similarity of the results and figures, the discussion on the analysis of these results and observations will not be repeated here.

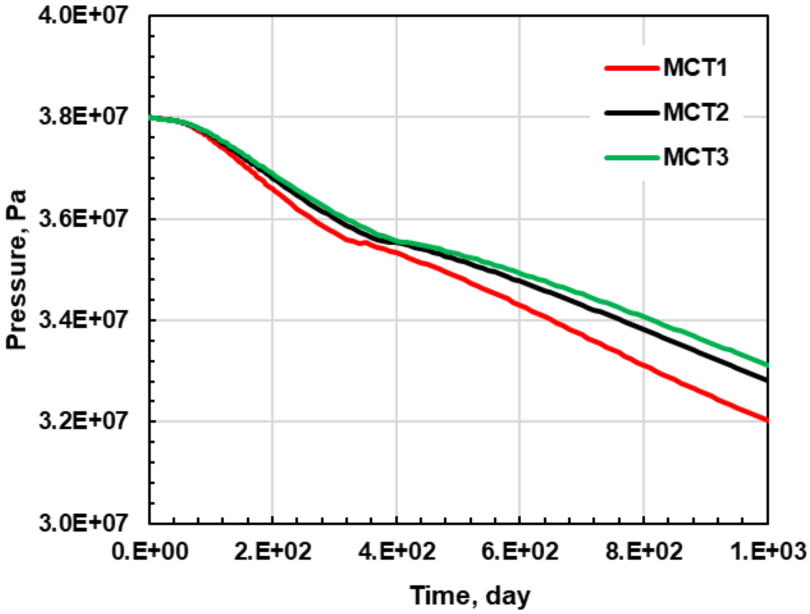

Figure 5.71 Pressure Evolution Over Time at Monitoring Points MCT1, MCT2 and MCT3 Near the Top of Plane C

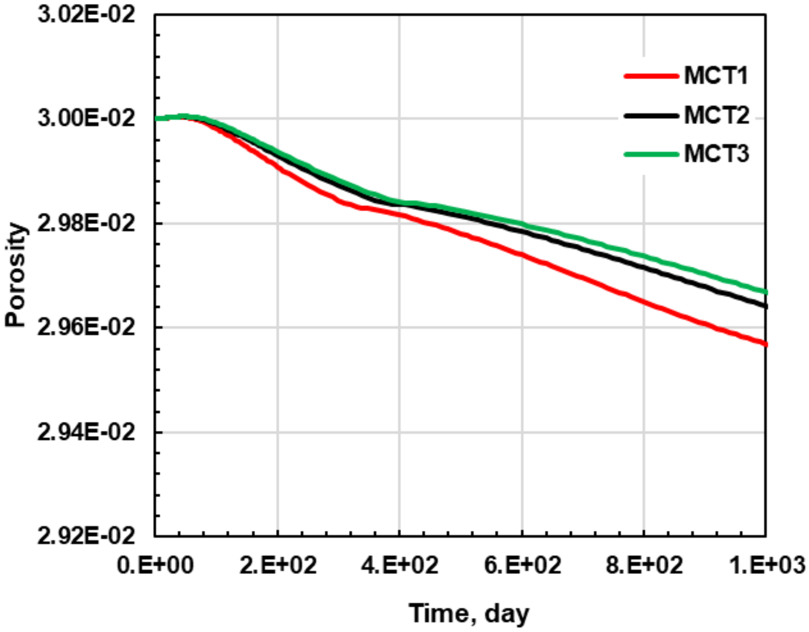

Figure 5.72 Porosity Evolution Over Time at Monitoring Points MCT1, MCT2 and MCT3 Near the Top of Plane C

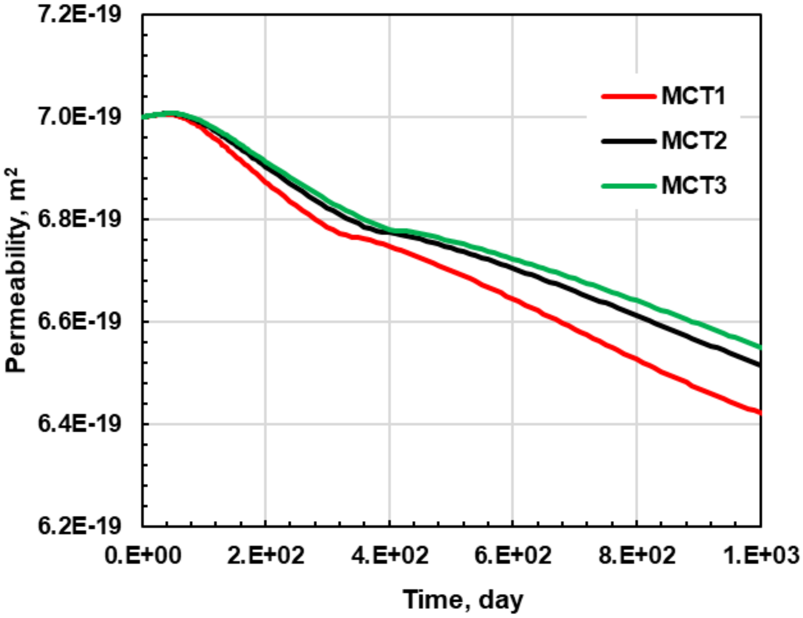

Figure 5.73 Permeability Evolution Over Time at Monitoring Points MCT1, MCT2 and MCT3 Near the Top of Plane C

5.4 Sensitivity Analysis

The sensitivity analysis focuses on the effect of the geomechanical properties because, unlike the estimates of the flow properties of the system under investigation that were fairly reliable, there was considerable uncertainty in the estimates of the geomechanical properties. I investigated the sensitivity of production to variations in the following geomechanical properties of the matrix and of the (far more uncertain and data-poor) fracture: the Poisson Ratio ν, the Young modulus of elasticity E, and the Biot coefficient b. In these sensitivity analysis studies, the mode of the BHP was linear-decline from 33.09 MPa (4800 psi), the final BHP was 13.79 MPa (2000 psi), kept constant after 30 days of decline, and the duration of the ramp-down period was 30 days. All other system conditions, properties and parameters were as listed in **Table 4.1**.

5.4.1 Matrix Geomechanical Parameters

Matrix Poisson's Ratio ν

Poisson's ratio ν is defined as a measure of the expansion of a material perpendicular to the applied stress, and provides a measure of the corresponding compaction. I tested the sensitivity of oil production to the following matrix ν values: 0.2, 0.25 (the base value used in the simulations), 0.3, and 0.35.

Figure 5.74 shows the effects of the value of the matrix ν on the oil production rate during a 3-year long production period, and shows that an increasing matrix ν leads to a decreasing oil production rate. Note that under the production conditions discussed above, the oil rate increases the first 30 days, and then decreases continuously during the rest of the production period.

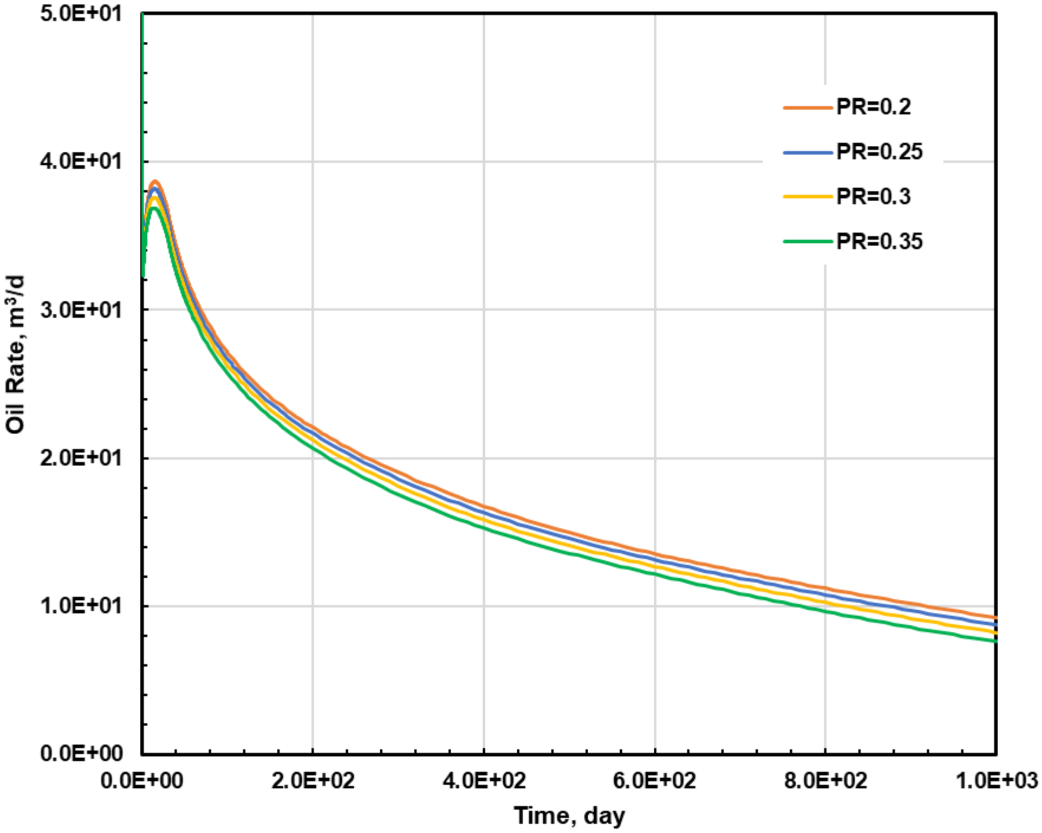

Figure 5.74 Sensitivity of the Oil Production Rate to the Matrix Poisson's Ratio ν

Figure 5.75 shows effect of the matrix ν on the cumulative oil production during the 3 years of production. As the consistent results of **Figure 5.74** dictate, a lower matrix ν corresponds to a higher cumulative oil production. At t = 3 years, the total oil production for $\nu = 0.2$ is 106 thousand barrels, which is 8.4 thousand barrels more to that obtained for $\nu = 0.35$. The roughly 10% deviation between the cumulative oil productions for the minimum and maximum ν is rather moderate, and easily within the margin of uncertainty expected in a natural system. Thus, obtaining an accurate estimate of the matrix ν in the preparatory course of the design of production from shale oil reservoirs is desirable, but not critical. Note that the effect of ν on oil production is directly related to the combined effects of the changes in the matrix porosity and permeability, which have already been shown in the previous sections to be minor and, as expected, in agreement with the impact of ν.

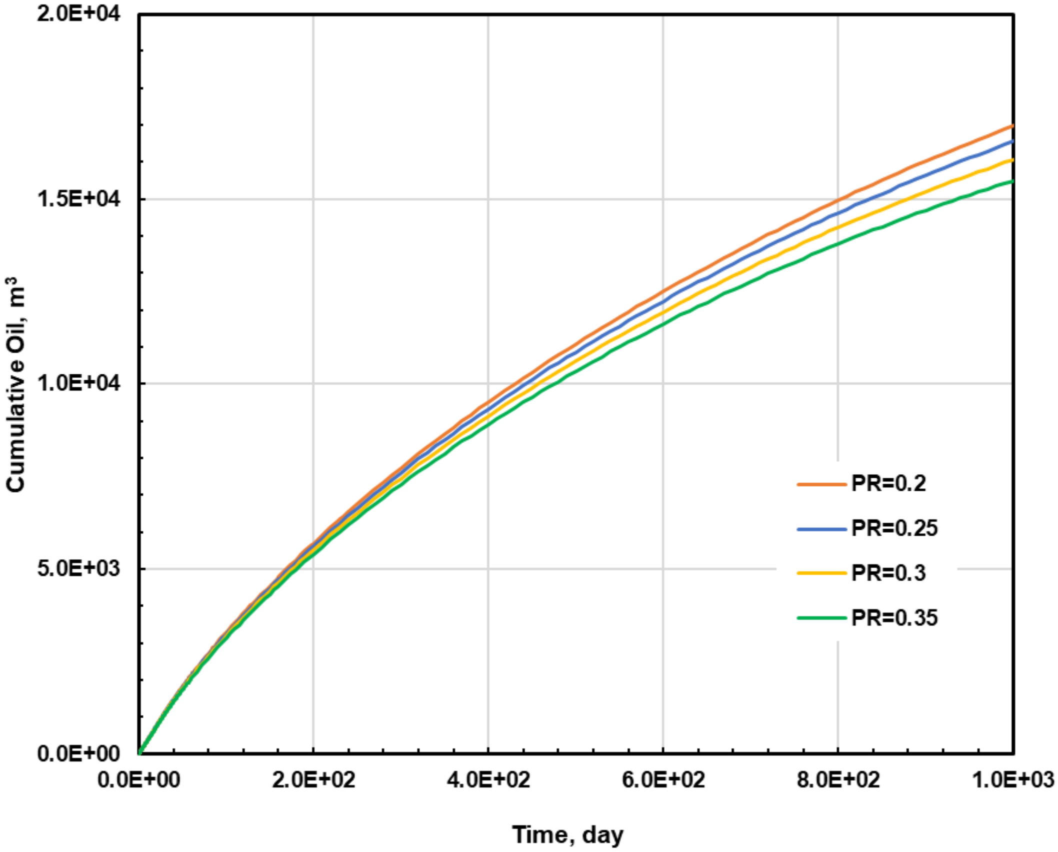

Figure 5.75 Sensitivity of the Cumulative Oil Production to the Matrix Poisson's Ratio ν

Figure 5.76 shows the evolution of the spatial distributions of pressure for the 4 different matrix ν values. Comparison of the plots in each column (corresponding to pressure distributions for different ν at the same time) shows moderate (but easily discernible) differences in the pressure distributions, with the higher ν values corresponding to consistently higher matrix pressures. This is consistent with expectations: a higher ν corresponds to a higher deformation of the medium, leading to a lower porosity and, consequently, a lower permeability (see **Eq. 4.11**), which is associated with slower depressurization. The higher pressures at the four observation times for the higher ν values in **Figure 5.76** are consistent with the expectations. **Figure 5.77** shows the stress distribution for the different matrix Poisson's Ratios, which is consistent with pressure evolution.

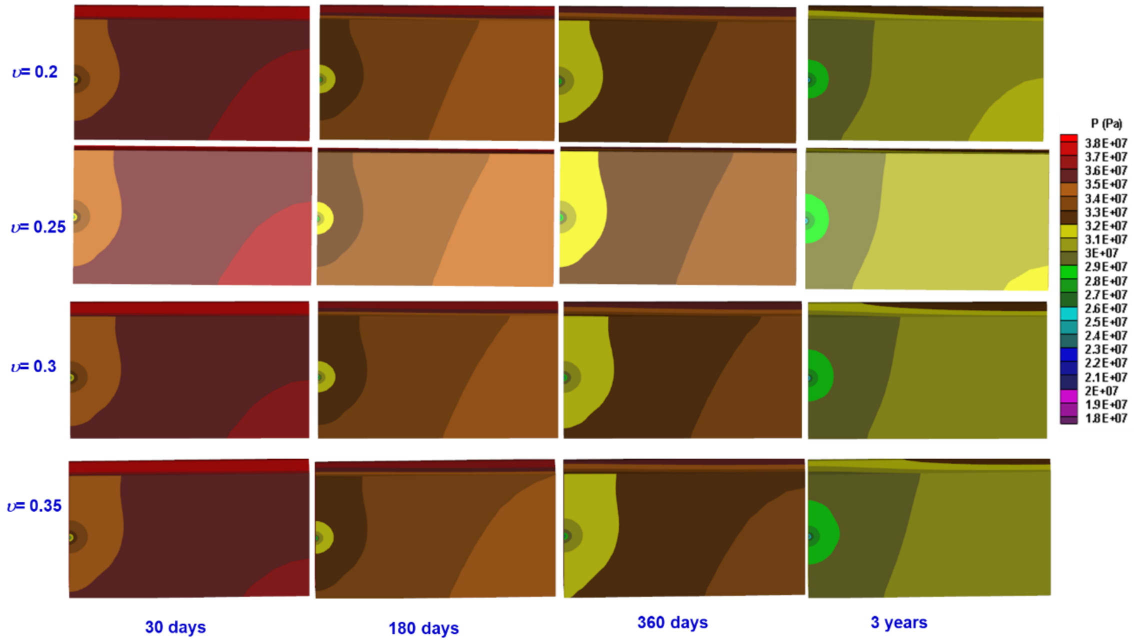

Figure 5.76 Pressure Distribution for the Different Matrix Poisson's Ratios ν

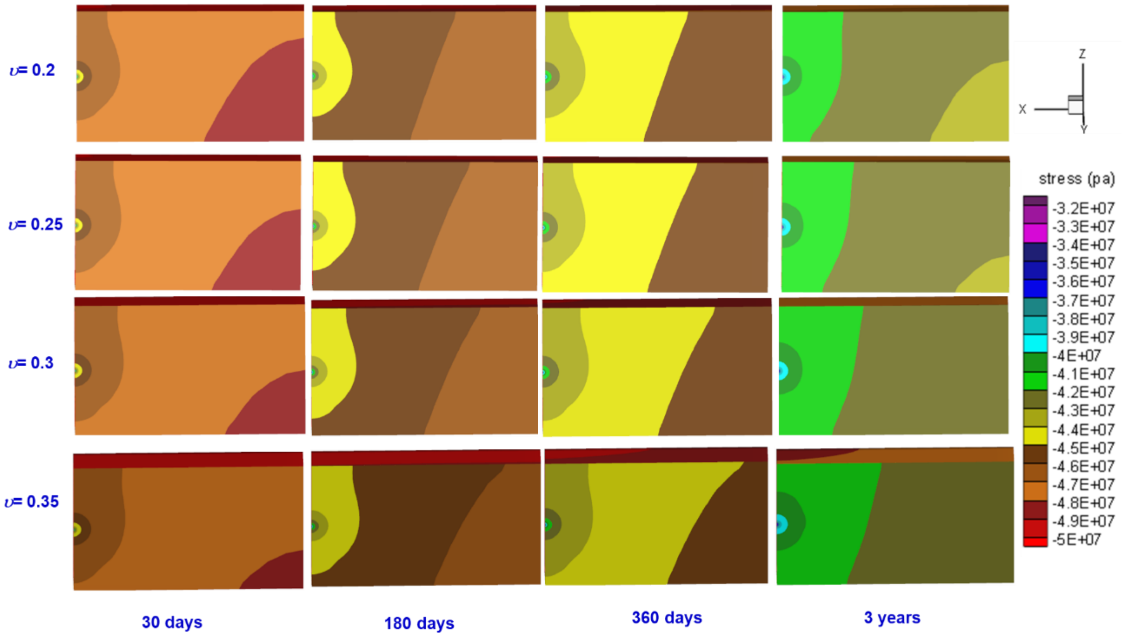

Figure 5.77 Stress Distribution for the Different Matrix Poisson's Ratios ν

Figure 5.78 displays the evolution of the fracture aperture for the different matrix ν values. As expected, the larger matrix deformation described by a larger ν value leads to a decrease in the fracture aperture. However, the difference between the fracture apertures obtained for the minimum and maximum ν values is only about 6% and its effect on the fracture permeability is similar (see **Eq. 4.12**), confirming the earlier realization that the effect of the matrix ν on the oil production is minor and acquisition of an accurate estimate of ν may not be a priority.

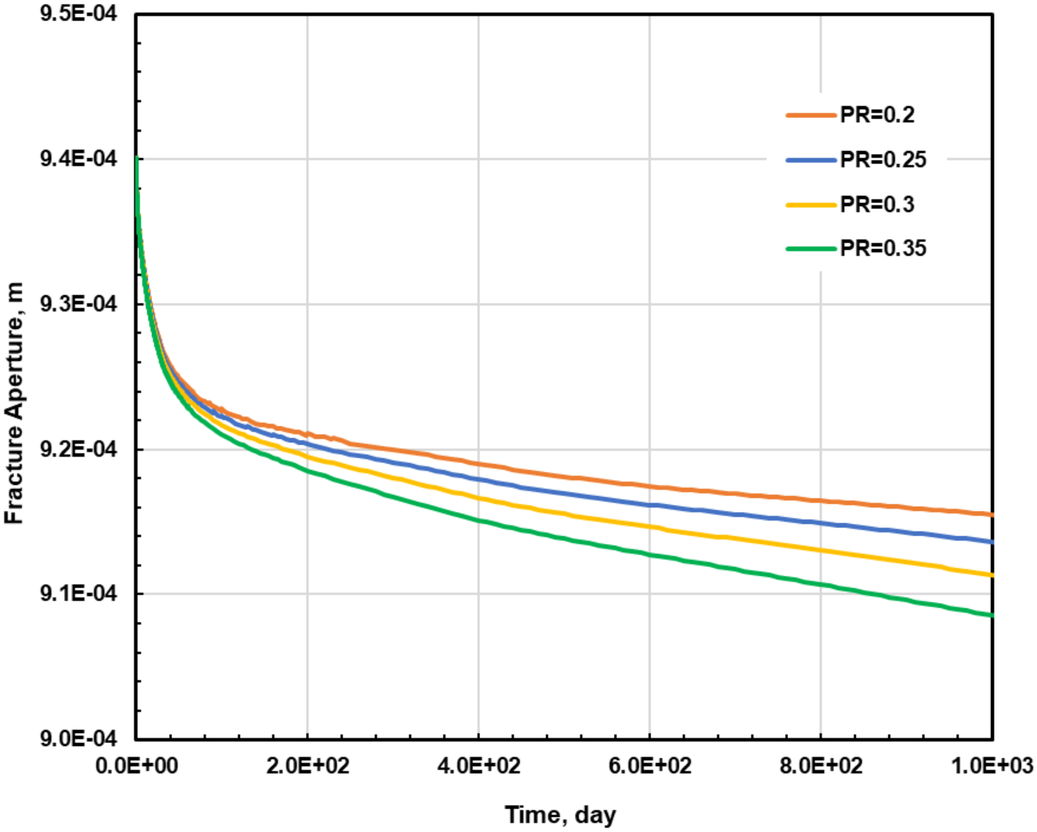

Figure 5.78 Effect of the Matrix Poisson's Ratio ν on the Fracture Aperture

Matrix Young's Modulus of Elasticity *E*

The Young modulus of elasticity *E* provides a measure of the stiffness of a solid material and is one of its most important mechanical properties. I investigated the sensitivity of oil production to the following four values of the matrix *E*: 8, 10, 20 (the base value), and 30 GPa.

Figure 5.79 presents the effect of the matrix *E* on the oil production rate during the 3-year long production period, and shows that the oil production rate increases inversely with the matrix *E*. The effect of the matrix *E* on the cumulative oil production follows (inevitably) in **Figure 5.80** the trend identified in **Figure 5.79** and shows an increasing cumulative oil production for a decreasing E value. At t = 3 years, the difference in the cumulative oil production estimates for the minimum and the maximum E values, is 3305 m^3 (20,800 STB), corresponding to about 20+% of the average production. This is not negligible and indicates that a solid estimate of the matrix E prior to the production design for a given reservoir is desirable.

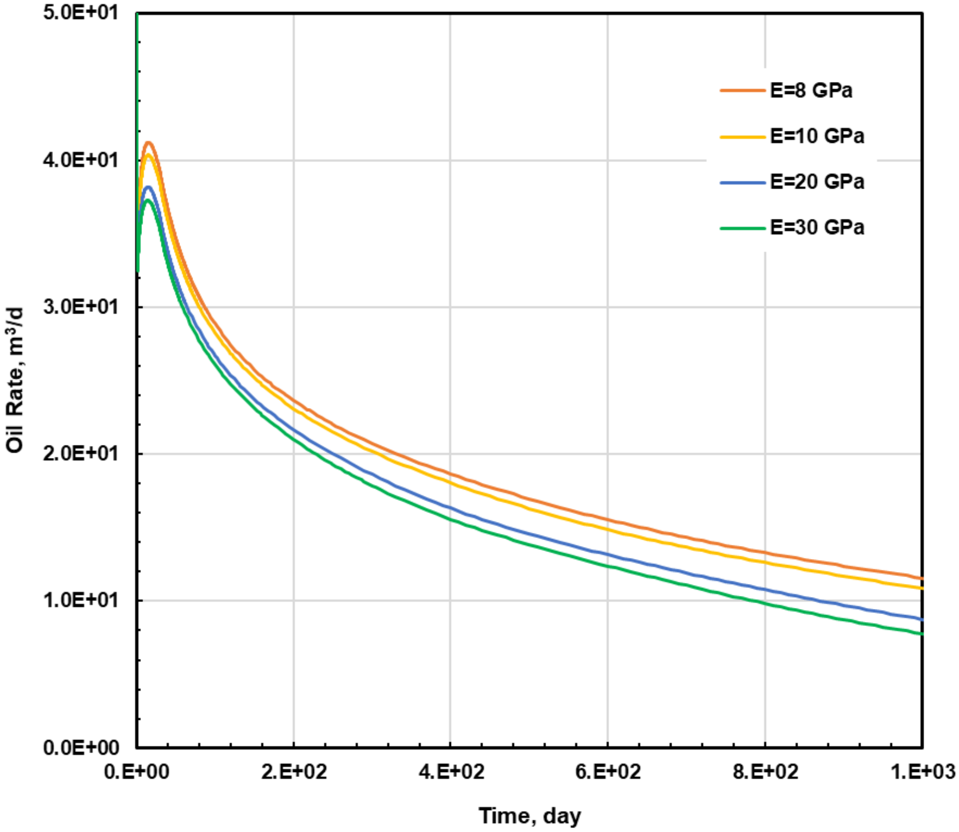

Figure 5.79 Sensitivity of the Oil Production Rate on the Matrix Young's Modulus of Elasticity *E*

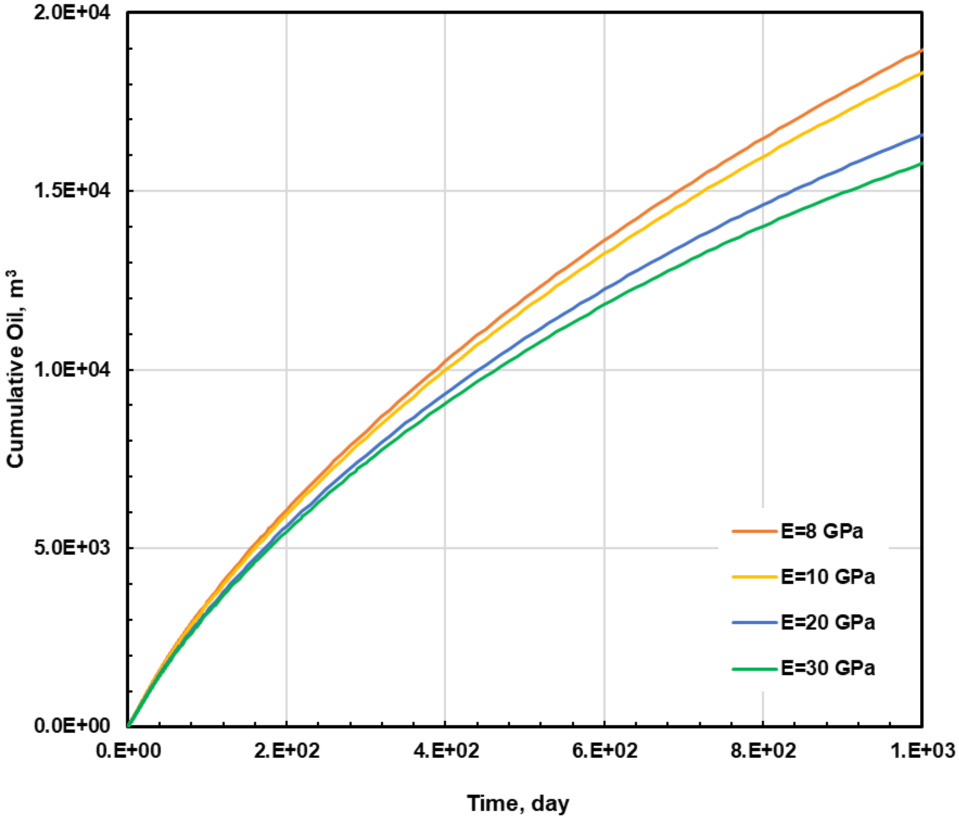

Figure 5.80 Sensitivity of the Cumulative Oil Production on the Matrix Young's Modulus of Elasticity *E*

Figure 5.81 shows the evolution of the spatial distributions of pressure for the different values of the matrix *E*. Comparison of the plots in each column (corresponding to pressure distributions for different *E* values at the same time) shows significant differences in the pressure distributions, with the higher *E* values corresponding to consistently higher matrix pressures. This is consistent with the production results in **Figures 5.79** and **5.80**. Thus, the matrix *E* value has a substantial impact on the reservoir short- and long-term production. **Figure 5.82** displays the stress distribution for different matrix Young's modulus, which is consistent with the pressure evolution.

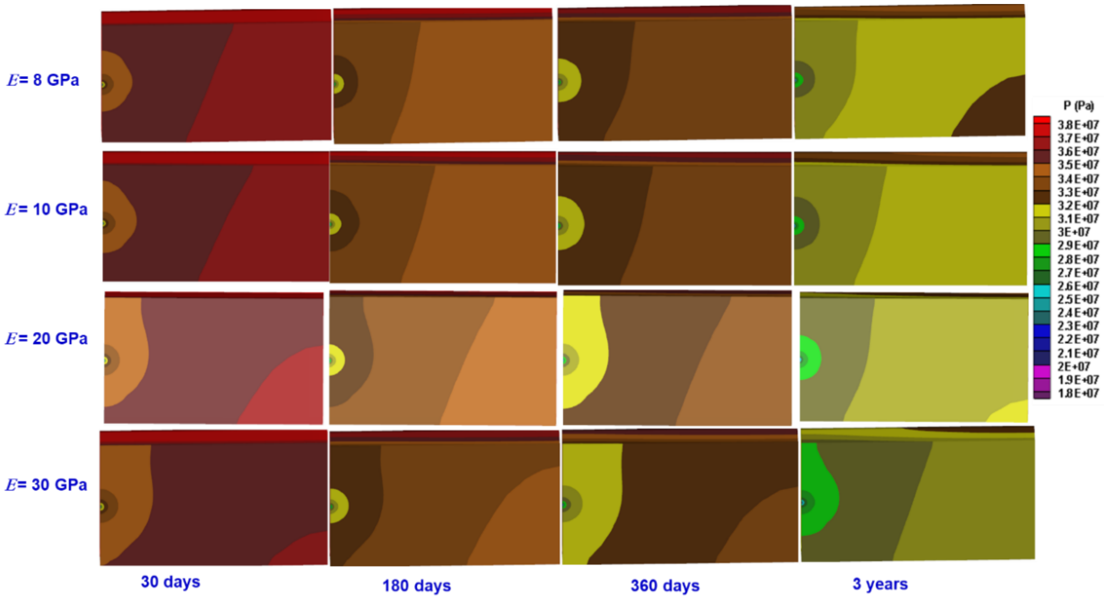

Figure 5.81 Pressure Distribution for Different Values of the Matrix Young's Modulus of Elasticity *E*

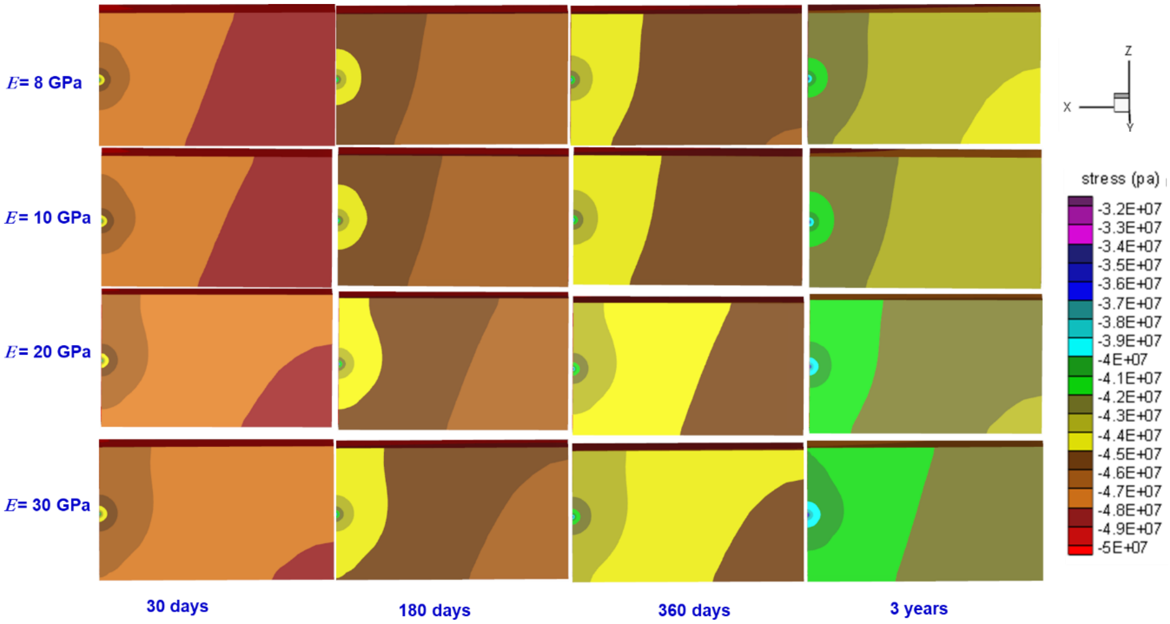

Figure 5.82 Stress Distribution for Different Values of the Matrix Young's Modulus of Elasticity *E*

Figure 5.83 displays the fracture aperture evolution for the four matrix *E* values. The fracture aperture increases with a decreasing matrix *E* value, but the effect is relatively minor over the 3 years of production.

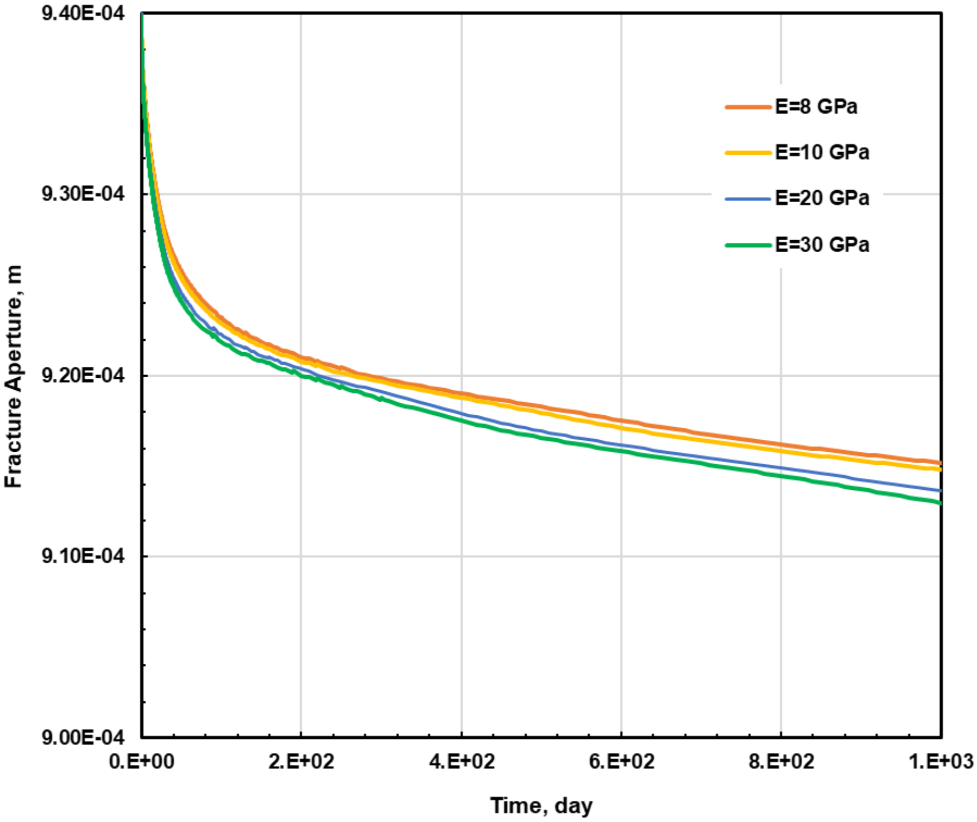

Figure 5.83 Sensitivity of the Fracture Aperture on the Matrix Young's Modulus of Elasticity *E*

Matrix Biot Coefficient *b*

The Biot coefficient *b* is defined as the change of fluid volume induced by bulk volume change in the drained condition. It is one of the key variables in describing the change of rock properties resulting from the reservoir depletion. I tested the sensitivity of oil production to the following four matrix *b* values: 0.65, 0.70, 0.75 and 0.8.

The evolution of the oil production rate and of the cumulative oil production for the four matrix Biot coefficient *b* values during the 3 years of production is presented in **Figures 5.84** and **5.85**, respectively. The two figures show that (a) the production rate and, consequently, the cumulative oil production rate, increase with an increasing *b*, but (b) the effect of the *b* value appears to be minor -- about 635.6 m^3 (4,000 STBs) between cumulative production estimates for the maximum and minimum *b* values, when the base production is 16525.6 m^3 (104,000 STBs). This leads to a conclusion that there is no overriding need to obtain an accurate estimate of the value of the matrix *b* for the preliminary production design studies.

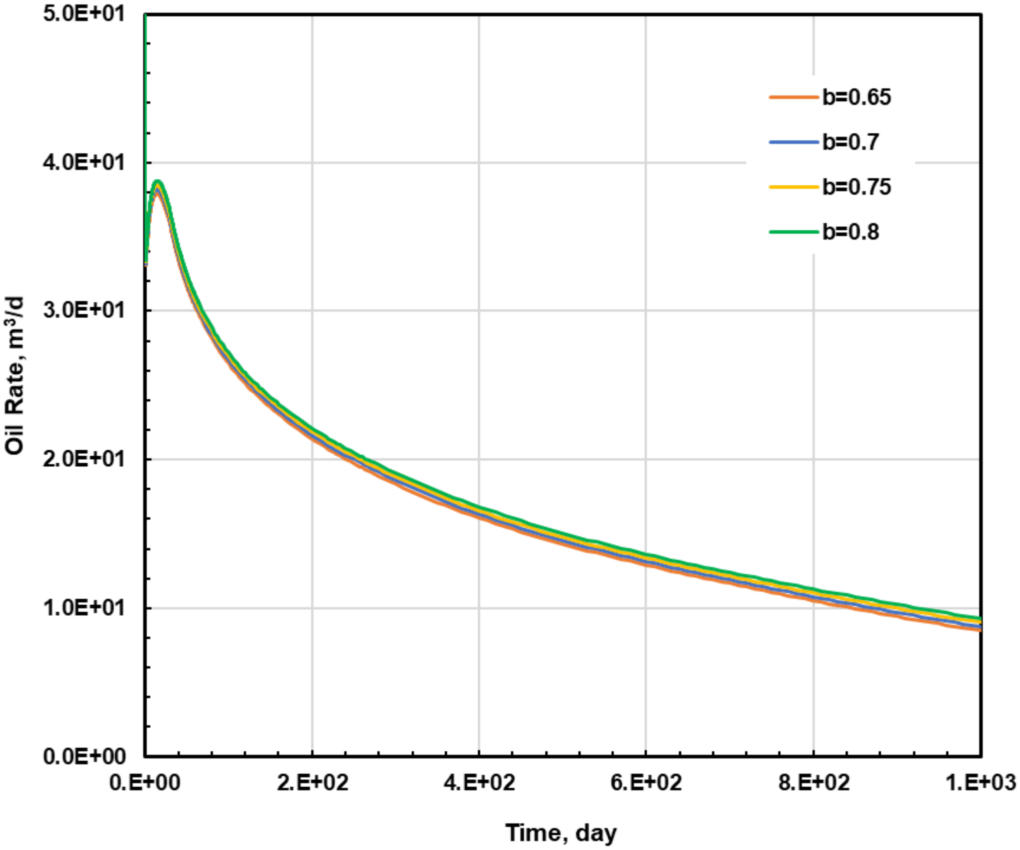

Figure 5.84 Sensitivity of the Oil Production Rate to the Matrix Biot Coefficient *b*

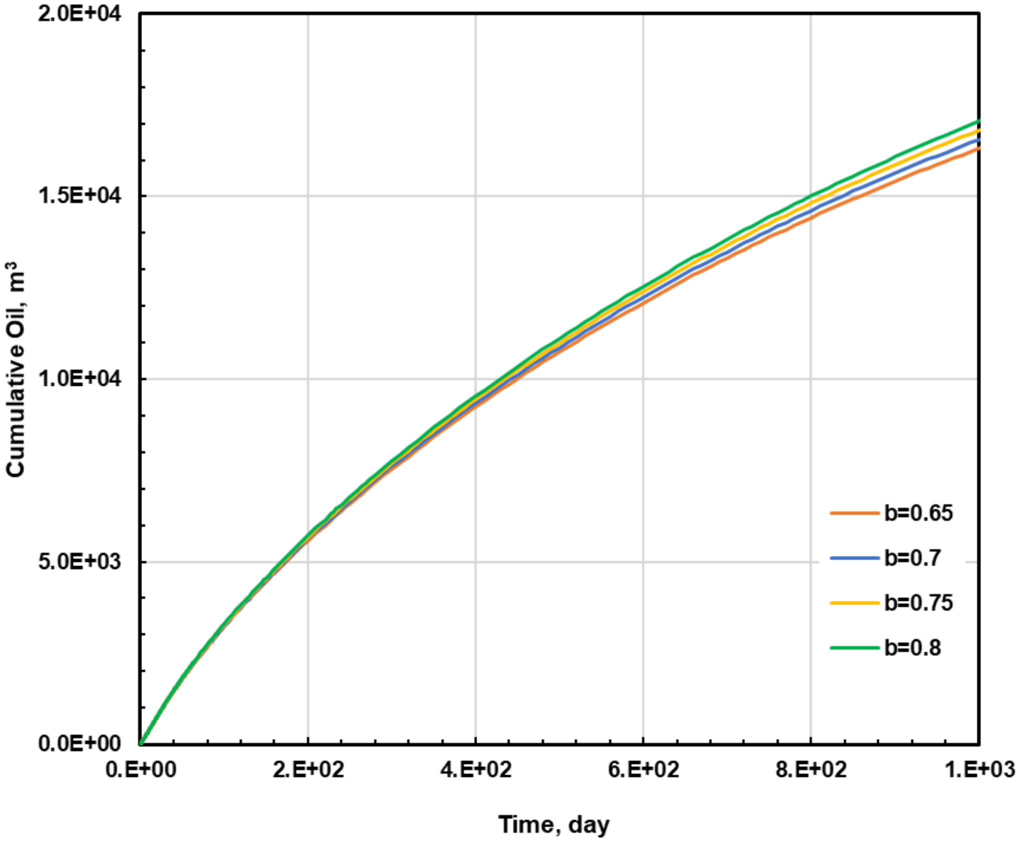

Figure 5.85 Sensitivity of the Cumulative Oil Production to the Matrix Biot Coefficient *b*

Figure 5.86 shows the evolution of the spatial distributions of pressure for the 4 different matrix *b* values. Comparison of the plots in each column (corresponding to pressure distributions for different *b* at the same time) shows practically no differences in the pressure distributions at the first 3 observation times (*i.e.*, until *t* = 360 days), and discernible but slight differences at *t* = 3 years. These results are consistent with the results in **Figures 5.84** and **5.85** that show a weak dependence of oil production on the matrix Biot coefficient. **Figure 5.87** shows the stress evolution of different matrix Biot coefficient, which is consistent with the pressure evolution.

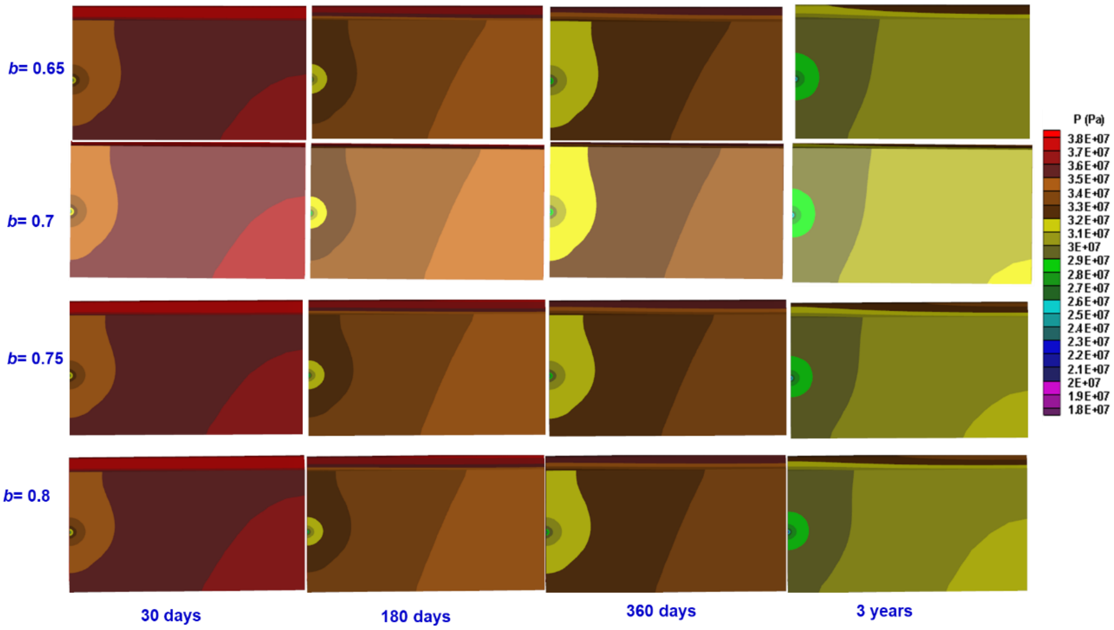

Figure 5.86 Pressure Distribution of Different Matrix Biot Coefficients *b*

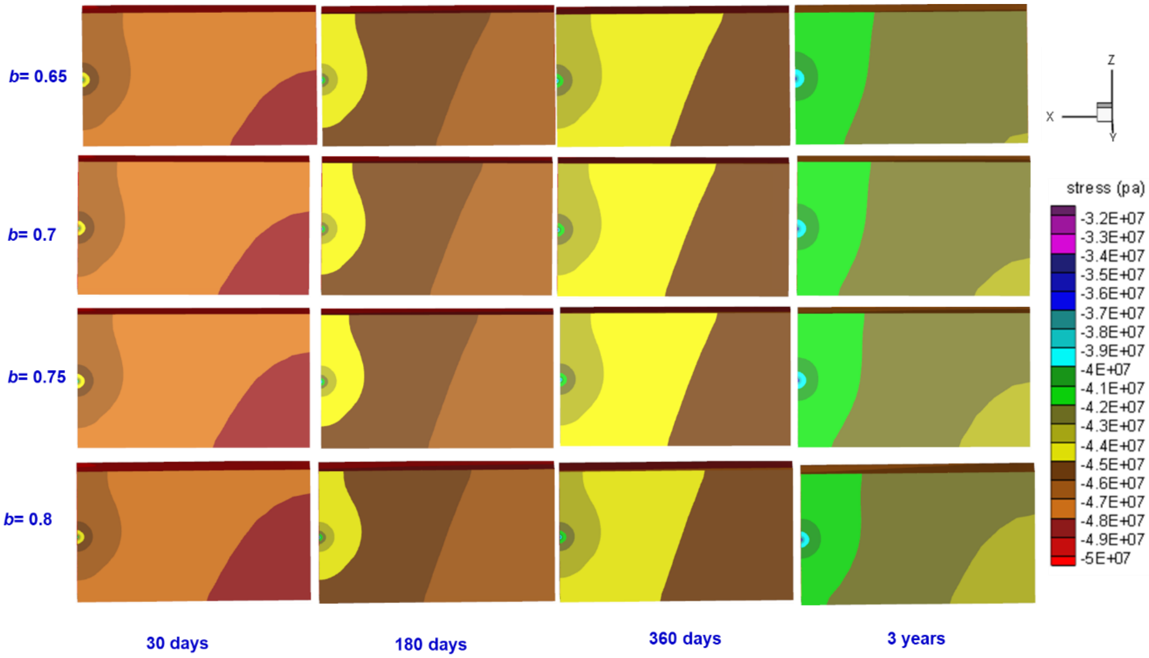

Figure 5.87 Stress Distribution of Different Values of the Matrix Biot Coefficients *b*

The effect of the matrix Biot coefficient *b* on the fracture aperture over time in **Figure 5.88** shows that (a) the aperture increases with an increasing value of *b* and (b) the dependence of the fracture aperture on the value of *b* (and, consequently, on the fracture permeability) appears to be weak.

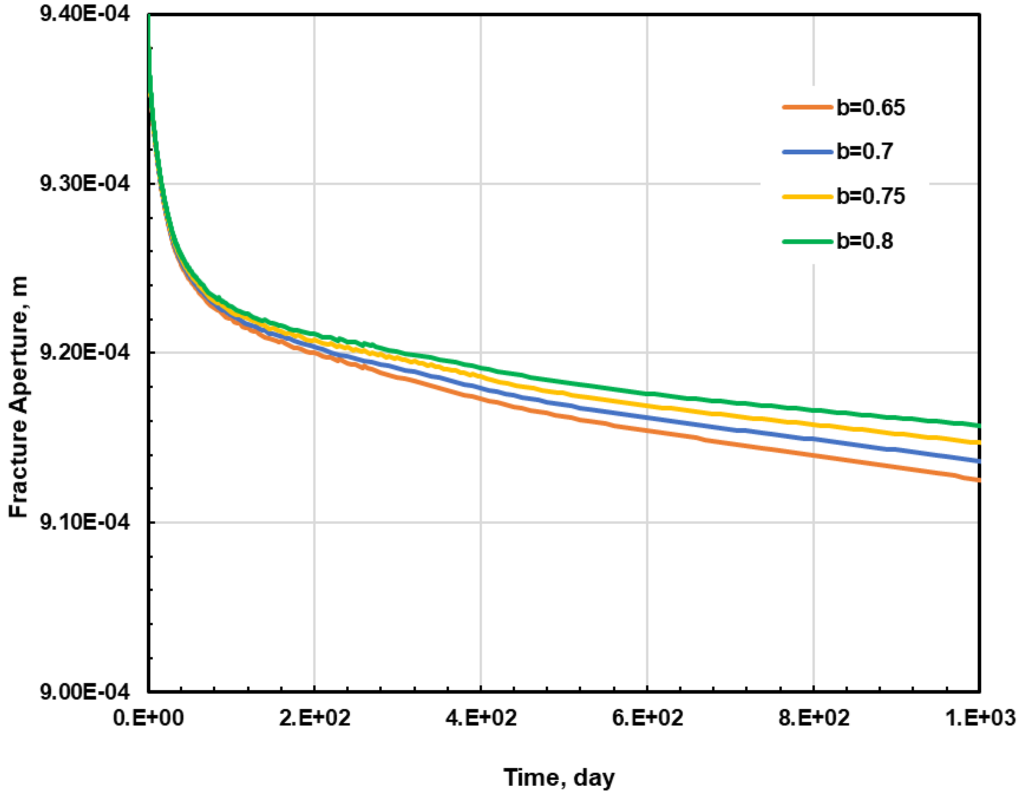

Figure 5.88 Sensitivity of the Fracture Aperture to the Matrix Biot Coefficient *b*

5.4.2 Fracture Geomechanical Parameters

Similar to matrix, fracture geomechanical parameters, including Poisson's ratio, Young's modulus and Biot's coefficient, also have effects on oil cumulative production, even though the geomechanics effects become less with a lower in-situ stress.

Fracture Poisson's Ratio ν_f

The fracture Poisson's ratio ν_f is a key variable in the analysis of the fracture geomechanics. I tested the sensitivity of oil production to the following four values of the fracture ν_f: 0.0 (the base value in the simulations), 0.05, 0.1, and 0.15. Figure 5.89 displays the effects of the fracture ν_f on the oil production rate during the 3 years of production, and indicates that (a) the production rate increases with an increasing fracture ν_f, (b) the largest ν_f value yields a significant early production peak, (c) there is a strong early dependence of the production oil rate on the fracture ν_f, which (d) weakens with time, with the production rates for the various ν_f values converging for $t \geq 880$ days.

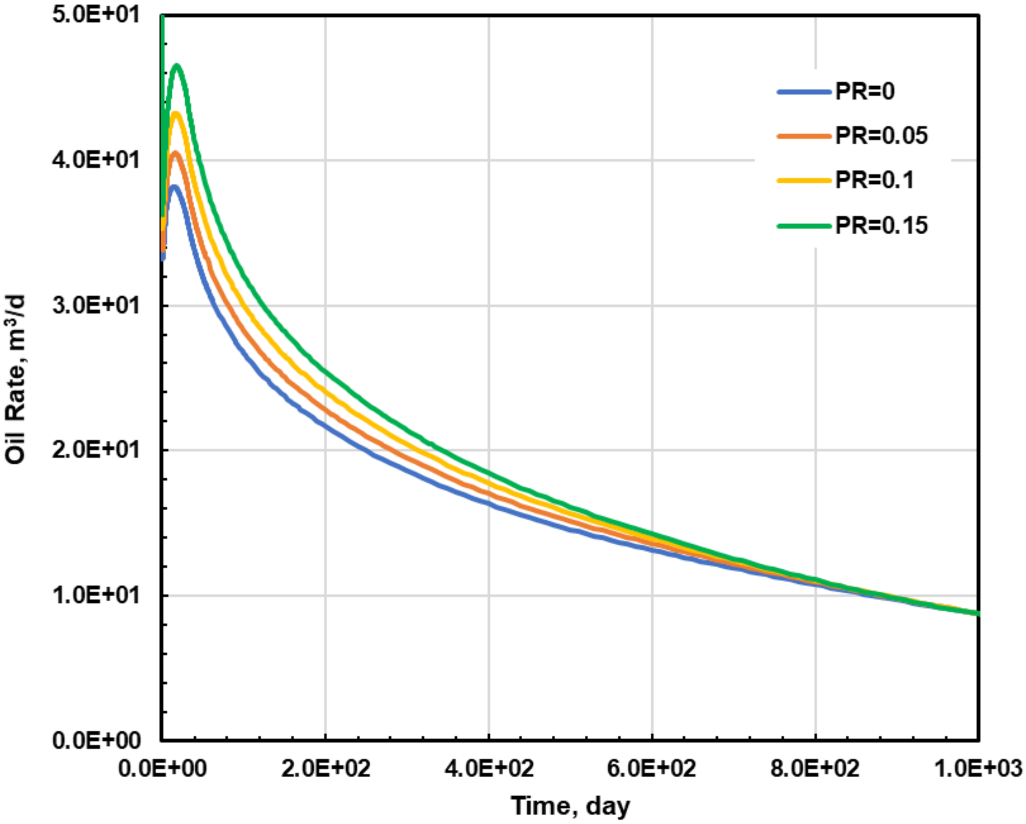

Figure 5.89 Sensitivity of the Oil Production Rate on the Fracture Poisson's Ratio ν_f

The evolution of the cumulative oil production over time for the four fracture Poisson's values ν_f is shown in **Figure 5.90** and shows that, (a) as expected from the known effect of the fracture ν_f on the oil production rate, the cumulative production increases with an increasing ν_f value but (b) the overall effect during the 3 years of production is rather moderate, with the maximum ν_f value resulting in an increase in production by about 12% over that for the base case at the end of production. However, this level of increase is easily within the margin of uncertainty expected in a natural system.

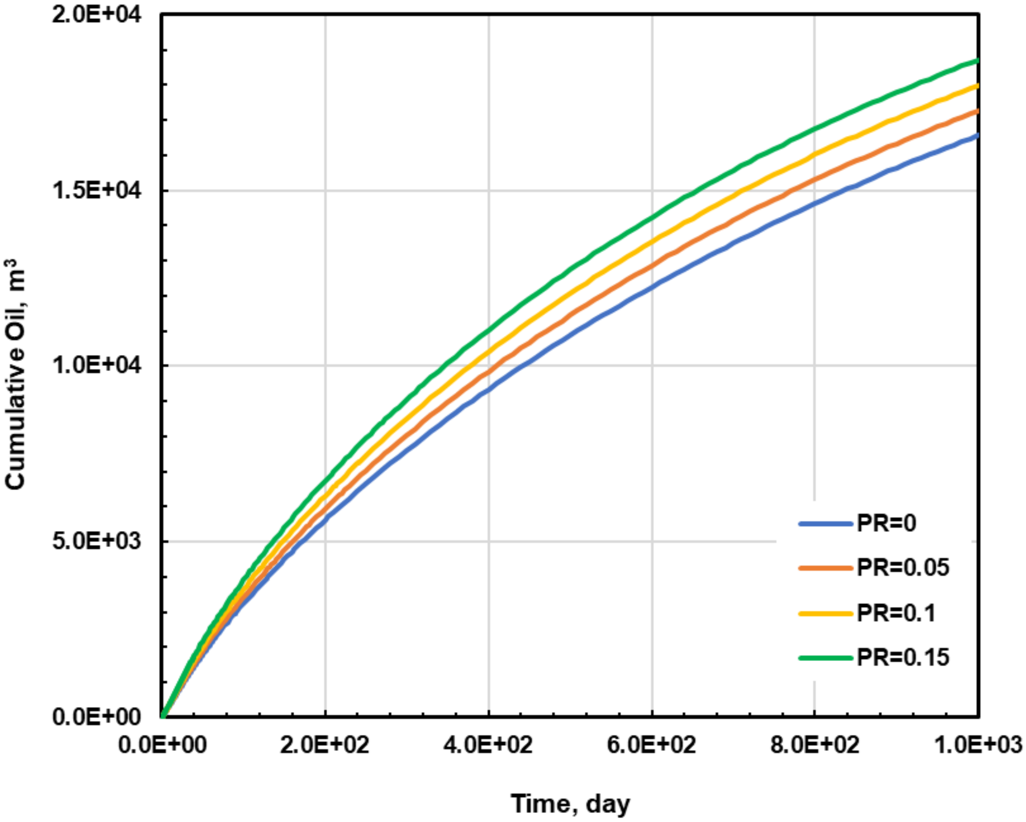

Figure 5.90 Sensitivity of the Cumulative Oil Production on the Fracture Poisson's Ratio ν_f

Figure 5.91 shows the evolution of the spatial distributions of pressure for the 4 different fracture ν_f values. Comparison of the plots in each column (corresponding to pressure distributions for different ν_f at the same time) shows significant differences in the pressure distributions at all times, consistent with the results in **Figures 5.89** and **5.90**. Higher fracture ν_f values correspond to lower pressures in the spatial distributions in the simulation domain that are depicted in each set of panels at the same times. These results tend to indicate that obtaining an accurate estimate of the fracture Poisson's ratio ν_f is important for accurate predictions of production from shale oil reservoirs. **Figure 5.92** shows the stress distribution of different values of the fracture Poisson's ratio. The evolution is similar with pressure change.

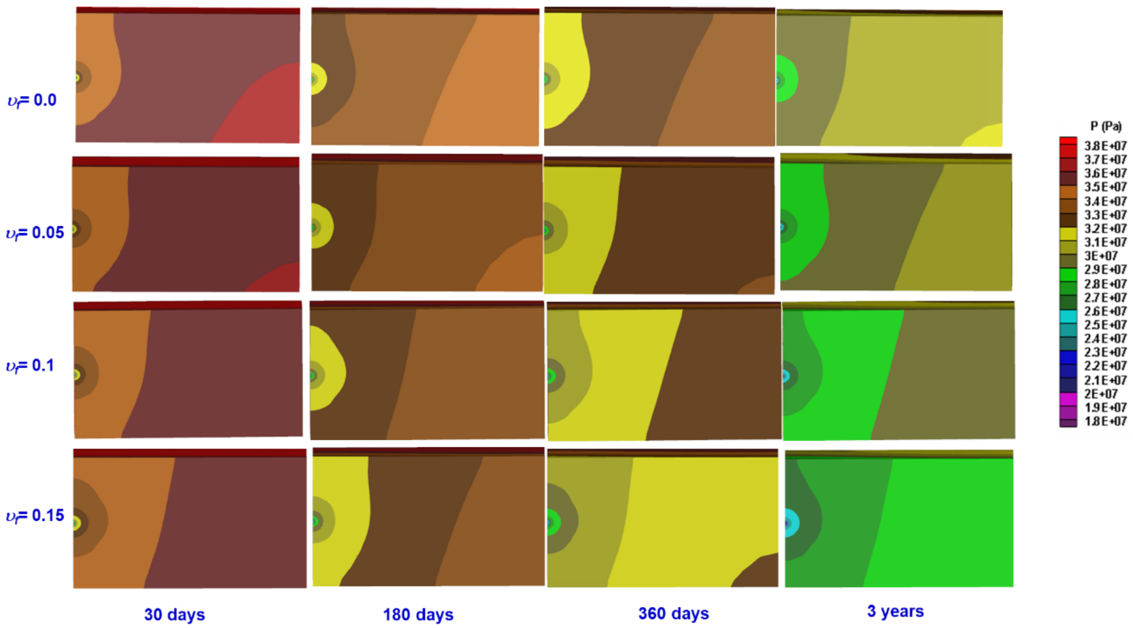

Figure 5.91 Pressure Distribution for Different Values of the Fracture Poisson's Ratio ν_f

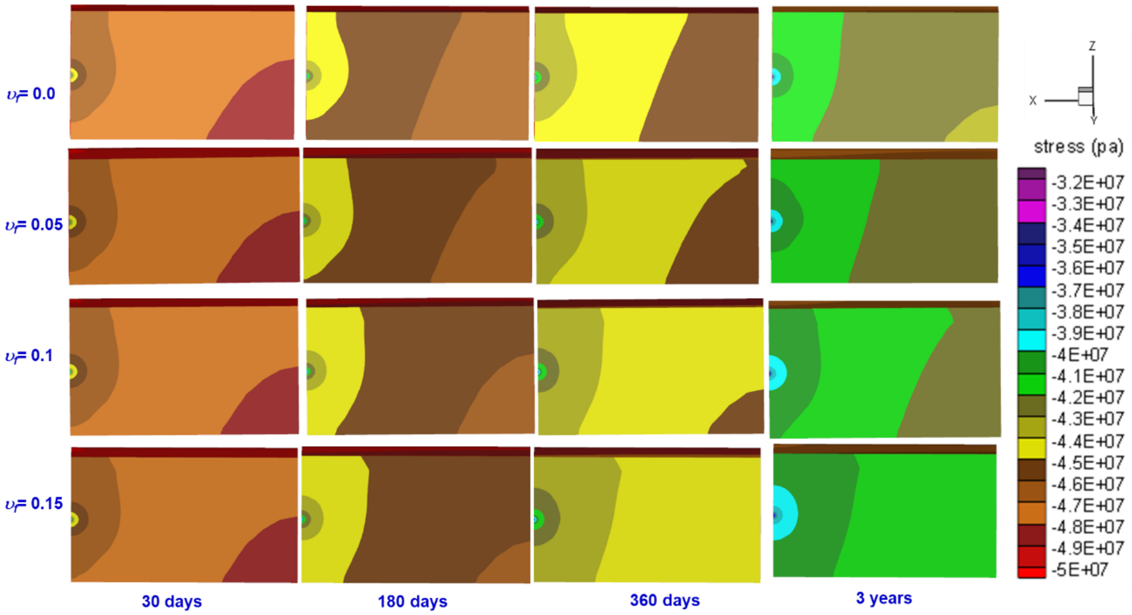

Figure 5.92 Stress Distribution of Different Values of the Fracture Poisson's Ratio ν_f

The evolution of the fracture aperture over time as a function of the fracture Poisson's ratio ν_f in **Figure 5.93** shows that (a) as expected, an increasing ν_f (which indicates a tendency for easier deformation) leads to a decreasing fracture aperture, but (b) the overall effect is almost negligible, as the difference in aperture for the largest ν_f tested value results in a difference of less than 1% from that obtained for the base case at t = 3 years.

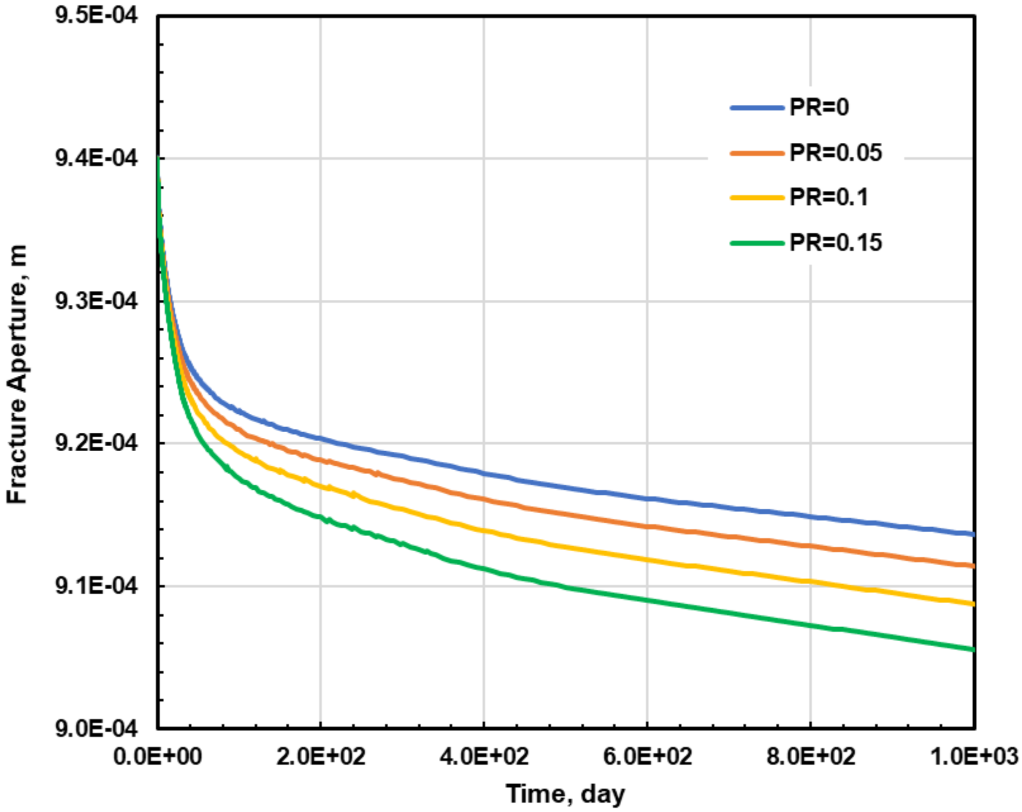

Figure 5.93 Effect of the Fracture Poisson's Ratio ν_f on the Fracture Aperture

Fracture Young's Modulus of Elasticity E_f

The fracture Young modulus of elasticity E_f is one of its most important mechanical properties, if not the most important one. I investigated the sensitivity of oil production to the following four values of the fracture E_f: 80, 100, 200 (the base value), and 300 MPa.

Figure 5.94 presents the effect of the fracture E_f on the oil production rate during the 3-year long production period, and shows that the oil production rate increases with the fracture E_f. This is the opposite effect of that caused by the matrix E. Additionally, the effect of the fracture E_f (a) is most pronounced during the early production, (b) is very significant, but (b) the effect weakens over time and appears to lead to convergence (or, possibly, to inversion) of the production rates at later times.

The effect of the fracture E_f on the cumulative oil production in **Figure 5.95** clearly indicates that (a) the cumulative production increases with an increasing E_f (as the trend in the production rate would dictate) and (b) the effect is very significant during the entire production period. Thus, a 20% decrease in E_f from its base-case level of 100 MPa to 80 MPa results in a decrease in the cumulative oil production from 16525.6 m^3 (104,000 STBs) to 8262.8 m^3 (52,000 STBs), *i.e.,* a 50% reduction. **Figure 5.95** provides clear evidence of the necessity to acquire an accurate estimate of the fracture Young's modulus of elasticity in order to obtain reliable estimates of both the short- and long-term production from shale oil reservoirs.

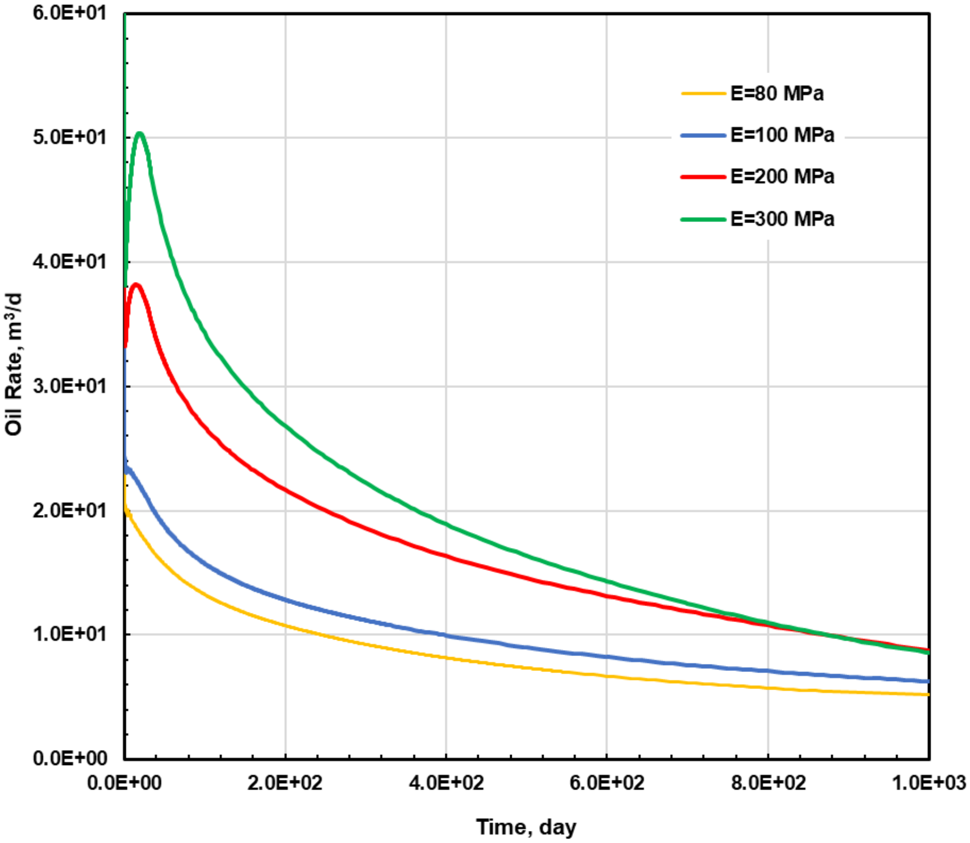

Figure 5.94 Sensitivity of the Oil Production Rate on the Fracture Young's Modulus of Elasticity E_f

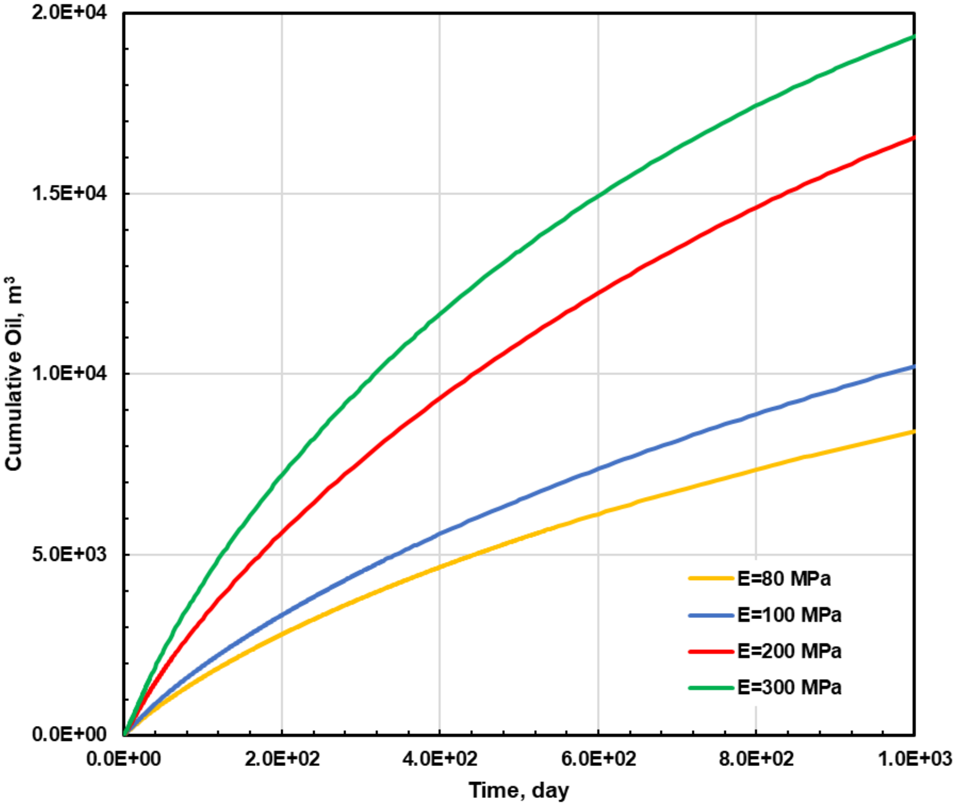

Figure 5.95 Sensitivity of the Cumulative Oil Production on the Fracture Young's Modulus of Elasticity E_f

Figure 5.96 shows the evolution of the spatial distributions of pressure for the different values of the fracture E_f. Comparison of the plots in each column (corresponding to pressure distributions for different E values at the same time) shows very significant differences in the pressure distributions corresponding to the various E_f values at all times: the higher E_f values correspond to consistently lower matrix pressures, indicating larger depressurization and, consequently, larger production. This is consistent with the production results in **Figures 5.94** and **5.95**. The results in **Figure 5.96** further underline the substantial impact of the fracture E_f value on the reservoir short- and long-term production. **Figure 5.97** displays the pressure evolution of different values of the fracture Young's modulus of Elasticity, which is consistent with the evolution of pressure.

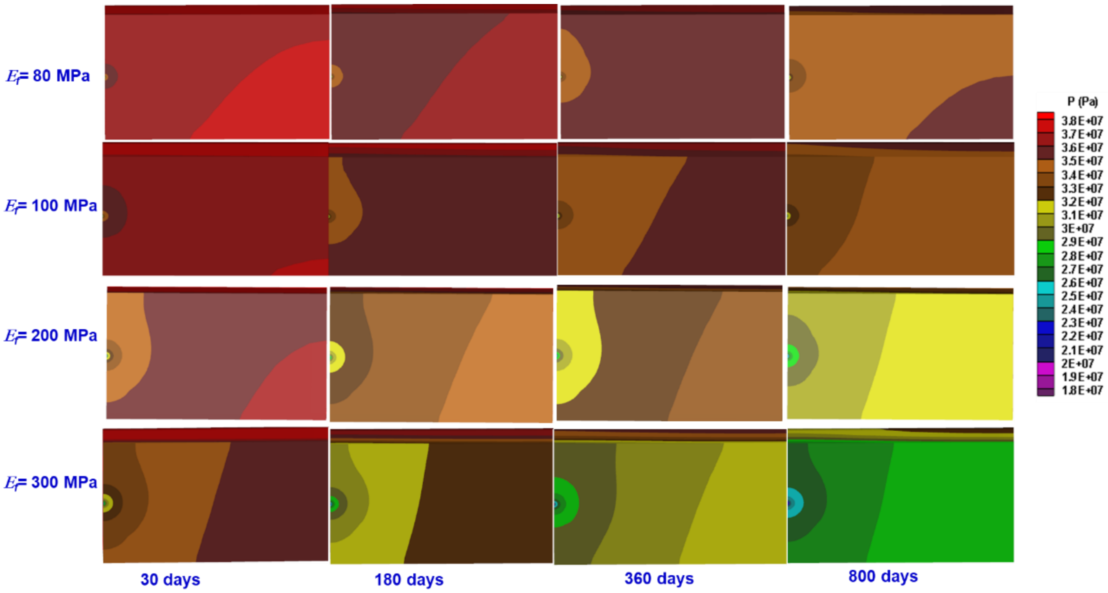

Figure 5.96 Pressure Distribution for Different Values of the Fracture Young's Modulus of Elasticity E_f

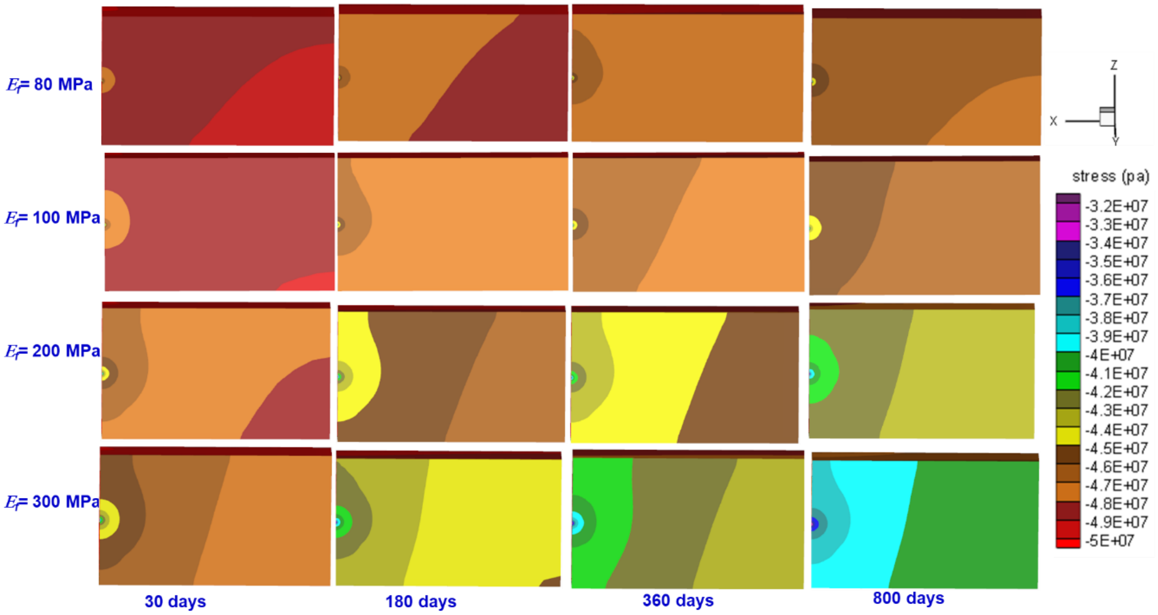

Figure 5.97 Stress Distribution of Different Values of the Fracture Young's Modulus of Elasticity E_f

The evolution of the fracture aperture over time for the four values of the fracture E_f is shown in **Figure 5.98** and further confirms the critical importance of this parameter. **Figure 5.98** clearly indicates the very significant impact of the fracture E_f on the fracture aperture, with larger E_f values corresponding to consistently larger apertures (and, consequently, correspondingly larger fracture permeabilities, see **Eq. 4.11**) during both short- and long-term production.

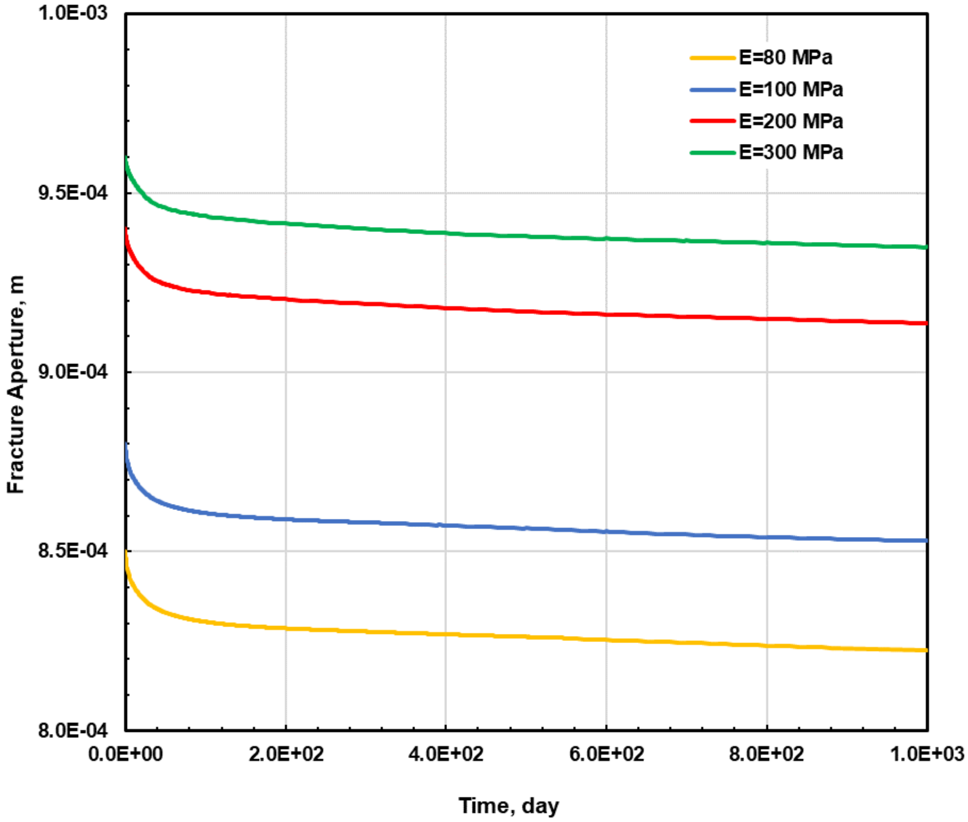

Figure 5.98 Fracture Aperture of Different Fracture Young's Modulus E_f

Fracture Biot Coefficient b_f

I tested the sensitivity of oil production to the following four values of the fracture Biot coefficient b_f: 1.0 85 (the base value in the simulations), 0.95, 0.90 and 0.85. **Figure 5.99** displays the effects of the fracture b_f on the oil production rate during the 3 years of production, and indicates that (a) the production rate increases with a decreasing fracture b_f, (b) the smallest b_f value yields a significant early production peak, (c) there is a strong early dependence of the production oil rate on the fracture b_f, which (d) weakens with time, with the production rates for the various ν_f values converging for $t \geq 900$ days.

The evolution of the cumulative oil production over time for the four fracture Biot coefficients b_f values is shown in **Figure 5.100** and shows that, (a) as expected from the known effect of the fracture b_f on the oil production rate, cumulative oil production increases with a decreasing b_f but (b) the overall effect during the 3 years of production is rather moderate, with the minimum b_f value resulting in an increase in production by about 12% over that for the base case at the production end. However, this level of increase is easily within the margin of uncertainty expected in a natural system.

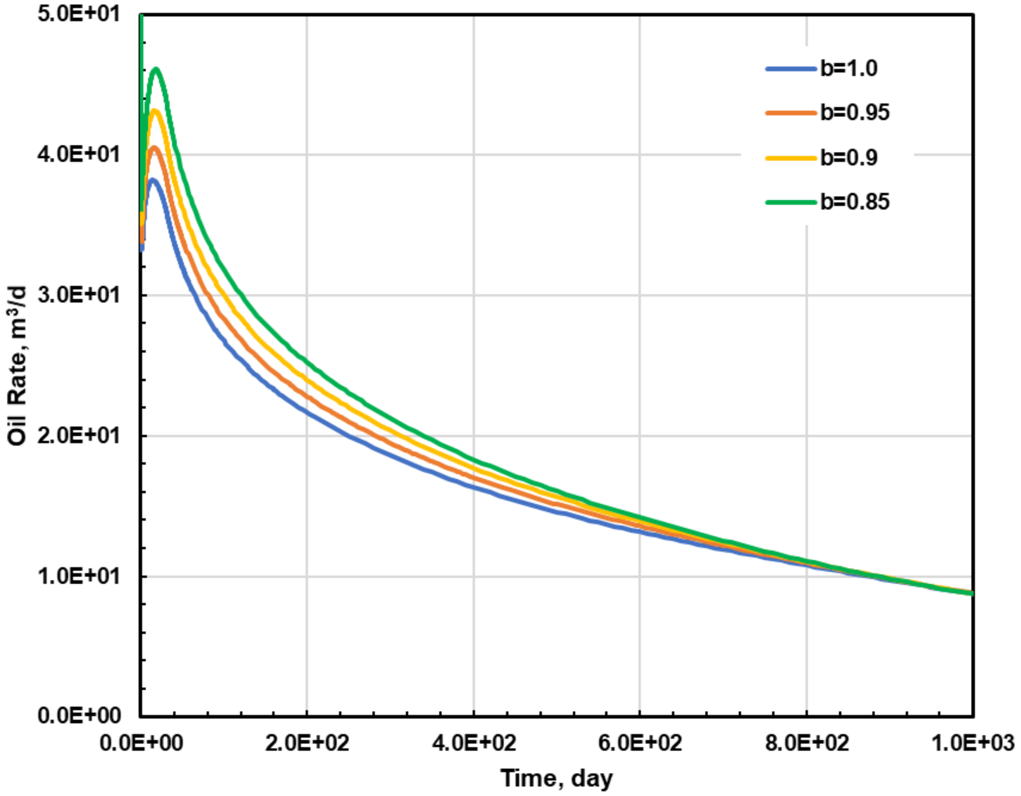

Figure 5.99 Sensitivity of the Oil Production Rate on the Fracture Biot Coefficient b_f

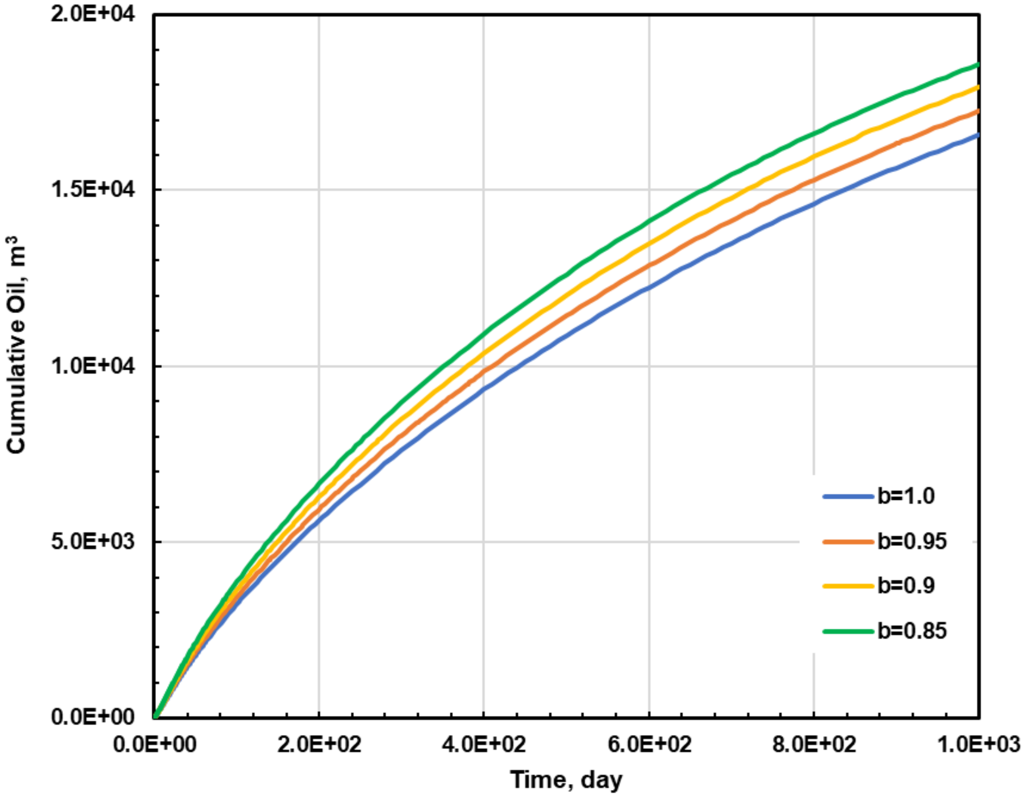

Figure 5.100 Sensitivity of the Cumulative Oil Production on the Fracture Biot Coefficient b_f

Figure 5.101 shows the evolution of the spatial distributions of pressure for the 4 different fracture Biot coefficient b_f values. Comparison of the plots in each column (corresponding to pressure distributions for different b_f at the same time) shows significant differences in the pressure distributions at all times, consistent with the results in **Figures 5.99** and **5.100**. Higher fracture b_f values correspond to higher pressures in the spatial distributions in the simulation domain that are depicted in each set of panels at the same times: this is because of the lower depressurization at higher fracture b_f and the correspondingly lower oil production, consistent with the results in

Figures 5.99 and **5.100**. These findings tend to indicate that obtaining an accurate estimate of the fracture Biot coefficient b_f is important for accurate predictions of production, and especially at early times. **Figure 5.102** shows the stress evolution of different values of the fracture Biot coefficient, which is consistent with pressure evolution.

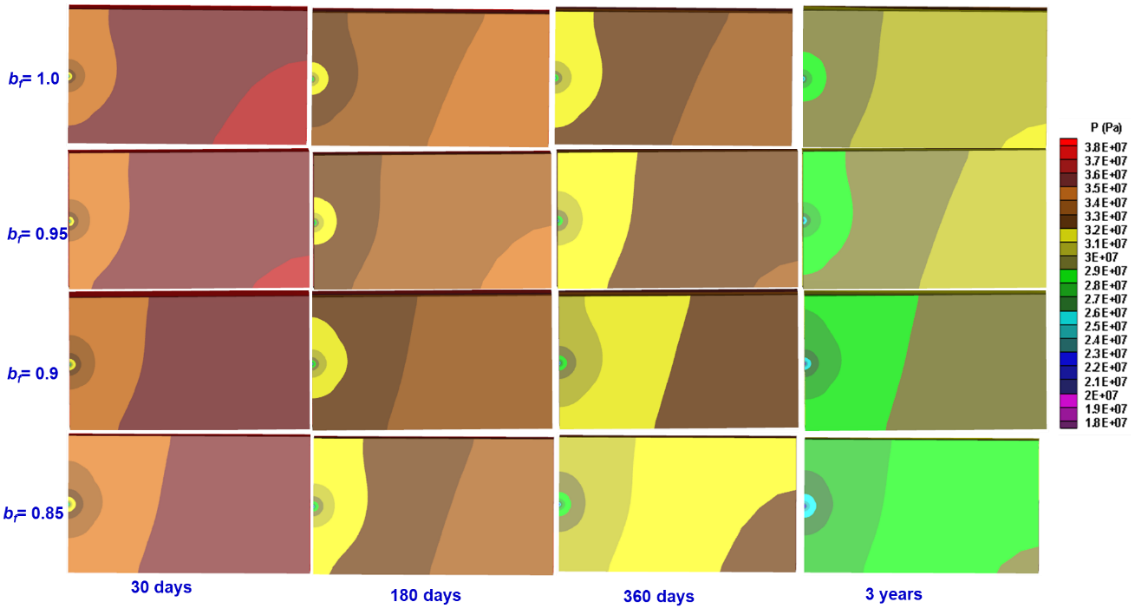

Figure 5.101 Pressure Distribution of Different Values of the Fracture Biot Coefficient b_f

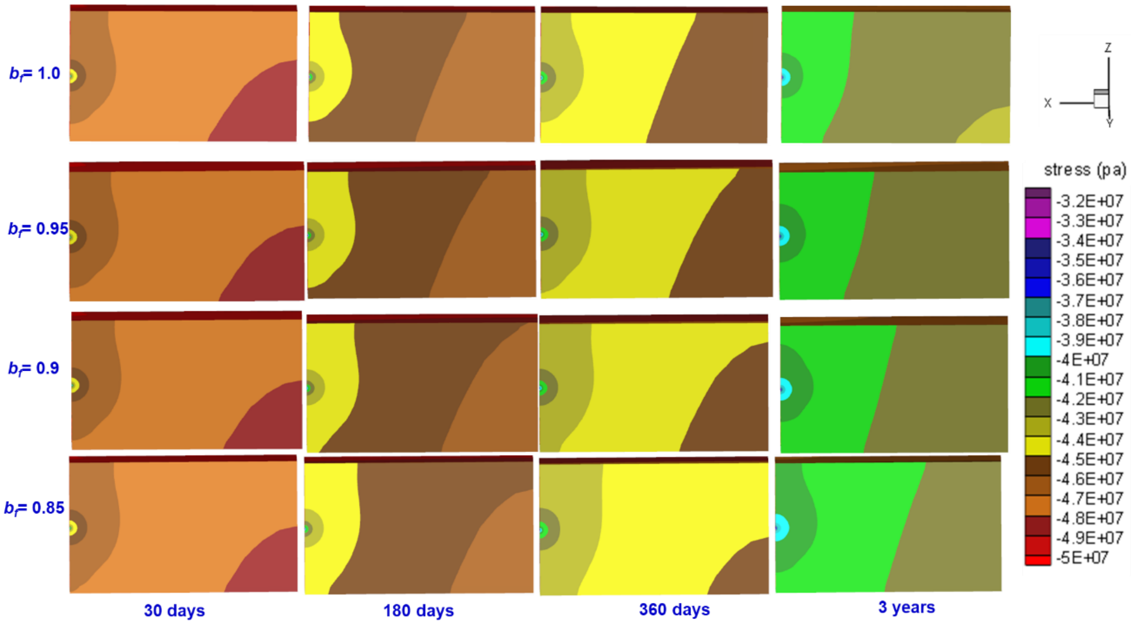

Figure 5.102 Stress Distribution of Different Values of the Fracture Biot Coefficient b_f

The evolution of the fracture aperture over time as a function of the fracture evolution of b_f in **Figure 5.103** shows that (a) as expected, an increasing b_f leads to an increasing fracture aperture, but (b) the overall effect is almost negligible, as the difference in aperture for the smallest b_f tested value results in a difference of less than 1% from that obtained for the base case at t = 3 years.

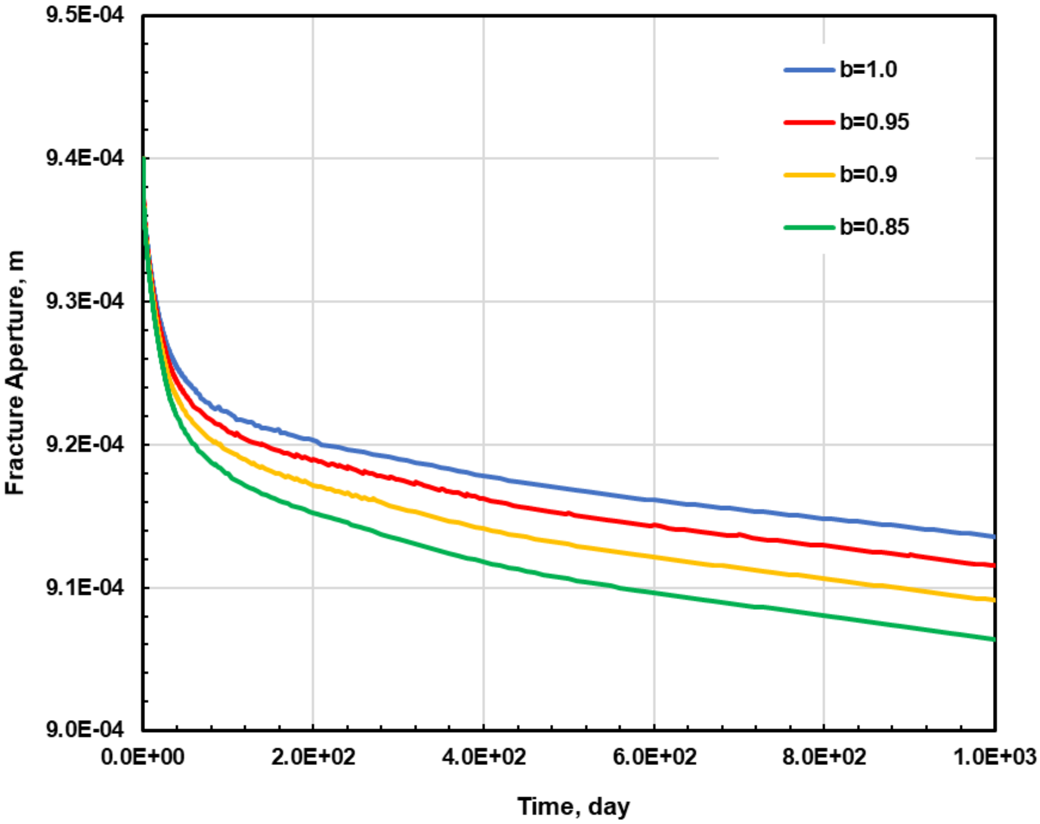

Figure 5.103 Sensitivity of the Fracture Aperture on the Fracture Biot Coefficient b_f

5.4.3 Sensitivity Analysis Summary and General Conclusions

In this section I investigated the sensitivity analysis of (a) the oil production rate, (b) the cumulative oil production, (c) the pressure spatial distributions over time and (d) the fracture aperture to the following geomechanical parameters of the matrix and the fracture: the Poisson's ratio, the Young modulus of elasticity and the Biot coefficient.

In general, the fracture geomechanical parameters appear to be far more important than the matrix parameters, and this should be the focus of geomechanical data acquisition. Among the fracture geomechanical properties, the Young modulus of elasticity has by far the largest impact, with the effects of the Poisson's ratio and the Biot coefficient being less pronounced and similar in magnitude. Of the matrix geomechanical properties, the Young modulus of elasticity appears to have the largest effect on oil production, with the effects of the Poisson's ratio and the Biot coefficient being moderate to minor.

CHAPTER VI

SUMMARY AND CONCLUSIONS

6.1 Summary

The goal of this thesis is to use field data (production and other supporting information) in order to (a) extract important parameters describing the relationship between choke management and production, to be used (b) to investigate BHP management practices and production strategies that maximize production without adversely affecting the geomechanical status of the producing multi-fractured horizontal wells under consideration.

The thesis is comprised of two parts. The first part of this work focuses on the analysis of production data by means of rate transient analysis (RTA) in an effort to determine reservoir and well parameters (e.g., permeability, fracture half-length, skin factor(s), etc). The software Topaze (Kappa Engineering) was used. The consistency of the history matches confirms the validity of the approach and provides confidence in the estimated parameters. The production rates and pressures are considered accurate and relevant, and we note that we used an external software (Prosper) to estimate the bottomhole pressure profile upon advice from the operator.

The second part of the thesis involved the development and applications of a simulator involving coupled flow and geomechanics codes written in FORTRAN 95. The geomechanical code was based on the fixed-stress method, and this was sequentially coupled to the flow simulator. The two-way coupling ensured continuous updating of the interdependent flow and geomechanical parameters and conditions. The simulation domain was based on the concept of stencil, *i.e.*, the smallest repeatable subdomain that can accurately represent the behavior of the entire multi-fractured horizontal well system. The coupled simulator was first used to determine key matrix and fracture properties and attributes through a history-matching optimization process that minimizes the deviations between phase production data and their numerical predictions. These data were used as input values in the ensuing simulations that attempted to determine the optimum BHP management and production strategy for the well and formation of interest. I accomplished this task by investigating several key parameters, such as the manner of reduction in the BHP, the final BHP level and the duration of the ramp-down period.

Finally, I conducted several simulations to determine the sensitivity of oil productions to key geomechanical properties (Poisson's ratio, Young's modulus of elasticity, and the Biot coefficient) of the matrix and fracture of the well system in the reservoir of interest, in an effort to identify the parameters on which the data acquisition process needs to focus if reliable predictions of the system behavior and production are to be obtained during the preliminary process of the design of the production system and operation.

6.2 Conclusions

The following conclusions were drawn from this study:

- The field history data utilized in this work were generally acceptable as initial inputs to the simulation analysis.
- The RTA analysis provided usable information on the BHP relationship to operational practices and data, as well as fracture and matrix reservoir properties that were consistent with the reference data provided by the well operator.
- The coupled flow and geomechanical simulator that I developed and used was an effective tool for (a) capturing the coupled flow and geomechanical behavior of the investigated system, (b) determining the flow properties and parameters by means of history matching using production data, and (c) determining parameters determining optimal well operation for maximal production.
- I used the coupled flow and geomechanics simulator to investigate the system behavior during various production scenarios that involved (a) variable methods of reducing the BHP to the desirable level (continuous linear decline, step-wise decline and instantaneous decline), (b) the final BHP level and (c) different durations of the ramp-down period to the final BHP. The analysis covered a production period of 3 years and determined that maximal oil production is attained by using a continuous, linearly-declining BHP to reach the lowest possible pressure level after the longest-possible ramp-down period. However, the system appeared quite resilient in terms of the effects of geomechanics on production, and it could be produced aggressively for larger early production without significantly compromising the long-term cumulative production by adversely affecting the fracture integrity and production performance.

- The main conclusions that can be reached from the observations at the monitoring points on the four planes (HF, A, B and C) are that:
  - Reductions in production over time can be attributed — excluding the effect of the continuously declining driving force of production, caused by the decreasing difference between the BHP and the system pressure as time advances — mainly to reductions in the permeability of the fracture.
  - Of the two possible reasons responsible for the reduction in the fracture permeability, the main cause appears to be the reduction in the fracture porosity, as the reduction in the fracture aperture appears to be minor at all the locations I investigated.
  - Changes in the porosity and permeability of the matrix appear to be minor, and they are unlikely to have a significant contribution to the reduction in the oil production over time: reduction in the fracture aperture rarely exceeds 10% of the initial value in the reservoir under investigation (with the exception of cases with low Young's modulus of elasticity of the fracture), indicating the geomechanical resilience of the system.
  - Maximization of production from shale oil reservoirs should aim to minimize the effect of depressurization on the permeability of the proppant-filled hydraulic facture, either by means of BHP management practices that minimally affect the fracture permeability or through appropriate stimulation methods that yield low-compressibility proppant-filled hydraulic fractures. At this point, numerical simulation can provide information on the feasibility

  (or even possibility) of identifying BHP management practices that can result in minimal reductions in the fracture permeability over the course of production. It is unknown if there are stimulation methods that can result in proppant-filled hydraulic fractures that resist large changes in their permeability.

- In general, the fracture geomechanical parameters appear to be far more important than the matrix parameters to oil production, and this should be the focus of geomechanical data acquisition if reliable predictions of oil production are to be obtained during the preliminary stages of the design of the production system.

Among the fracture geomechanical properties, Young's modulus of elasticity has by far the largest impact, with the effects of the Poisson's ratio and the Biot coefficient being less pronounced and similar in magnitude. Of the matrix geomechanical properties, Young's modulus of elasticity appears to have the largest effect on oil production, with the effects of the Poisson's ratio and the Biot coefficient being moderate to minor.

REFERENCES

Abousleiman, Y., Cheng, A. D., Cui, L., Detournay, E., & Roegiers, J. C. (1996). Mandel's problem revisited. *Geotechnique*, 46(2), 187-195.

Allen, D. 1972. Environmental Aspects of Oil Producing Operations-Long Beach, California. *Journal of Petroleum Technology* **24** (02): 125-131.

Ashida, A., Kashihara, K., and Rutqvist, J. 2017. Coupled Fluid Flow and Geomechanical Modeling for Understanding the Mechanisms of Depletion-Induced Reservoir Compaction and Its Impact on Hydrocarbon Production. In *51st US Rock Mechanics/Geomechanics Symposium*: American Rock Mechanics Association.

Beggs, D.H. and Brill, J.P. 1973. A Study of Two-Phase Flow in Inclined Pipes. *Journal of Petroleum technology* **25** (05): 607-617.

Blasingame, T., Johnston, J., and Lee, W. 1989. Type-Curve Analysis Using the Pressure Integral Method. In *SPE California Regional Meeting*: Society of Petroleum Engineers.ISBN 1555635644.

Blasingame, T. and Lee, W. 1986. *Variable-Rate Reservoir Limits Testing. Permian Basin Oil and Gas Recovery Conference, Midland, Texas, 13-15 March*. SPE-15028-MS. http://dx. doi. org/10.2118/15028-MS.

Blasingame, T., McCray, T., and Lee, W. 1991. Decline Curve Analysis for Variable Pressure Drop/Variable Flowrate Systems. In *SPE gas technology symposium*: Society of Petroleum Engineers.ISBN 1555635377.

Brown, K.E. 1977. Technology of Artificial Lift Methods. Volume 1. *Inflow Performance, Multiphase Flow in Pipes, the Flowing Well*.

Burstein, R.Henry, N.J.Collison, M.L. et al. 2019. Mapping 123 Million Neonatal, Infant and Child Deaths between 2000 and 2017. *Nature* **574** (7778): 353-358. DOI: 10.1038/s41586-019-1545-0

Coussy, O. (1995). *Mechanics of porous continua*. Wiley.

Coussy, O. (2004). *Poromechanics*. John Wiley & Sons.

Dean, R.H., Gai, X., Stone, C.M. et al. 2006. A Comparison of Techniques for Coupling Porous Flow and Geomechanics. *Spe Journal* **11** (01): 132-140.

Duong, A.N. 2011. Rate-Decline Analysis for Fracture-Dominated Shale Reservoirs. *SPE Reservoir Evaluation & Engineering* 14 (03): 377-387. DOI: 10.2118/137748-PA

Duns Jr, H. and Ros, N. 1963. Vertical Flow of Gas and Liquid Mixtures in Wells. In *6th world petroleum congress*: World Petroleum Congress.

Energy Information Administration (EIA). 2016. Annual Energy Outlook 2016 with Projections to 2040, DOE report DOE/EIA-0383. https://doi.org/10.2172/1329373.

Gutierrez, M., Lewis, R., and Masters, I. 2001. Petroleum Reservoir Simulation Coupling Fluid Flow and Geomechanics. *SPE Reservoir Evaluation & Engineering* **4** (03): 164-172.

Ilk, D., Jenkins, C.D., and Blasingame, T.A. 2011. Production Analysis in Unconventional Reservoirs-Diagnostics, Challenges, and Methodologies. In *North*

American Unconventional Gas Conference and Exhibition: Society of Petroleum Engineers.ISBN 1613991223.

Kim, J., Moridis, G., Yang, D. et al. 2012. Numerical Studies on Two-Way Coupled Fluid Flow and Geomechanics in Hydrate Deposits. *SPE journal* **17** (02): 485-501.

Kim, J. and Moridis, G.J. 2014. Gas Flow Tightly Coupled to Elastoplastic Geomechanics for Tight-and Shale-Gas Reservoirs: Material Failure and Enhanced Permeability. *Spe Journal* **19** (06): 1,110-111,125.

Kim, J., Tchelepi, H.A., and Juanes, R. 2009. Stability, Accuracy and Efficiency of Sequential Methods for Coupled Flow and Geomechanics. In *SPE reservoir simulation symposium*: Society of Petroleum Engineers.ISBN 1555632092.

King, M.J., Wang, Z., and Datta-Gupta, A. 2016. Asymptotic Solutions of the Diffusivity Equation and Their Applications. In *SPE Europec featured at 78th EAGE Conference and Exhibition*: Society of Petroleum Engineers.ISBN 1613994575.

Kumar, A., Seth, P., Shrivastava, K. et al. 2018. Optimizing Drawdown Strategies in Wells Producing from Complex Fracture Networks. In *SPE International Hydraulic Fracturing Technology Conference and Exhibition*: Society of Petroleum Engineers.ISBN 1613996225.

Lee, J., Rollins, J. B., & Spivey, J. P. (2003). *Pressure transient testing*. Richardson, Tex.: Henry L. Doherty Memorial Fund of AIME, Society of Petroleum Engineers,.

Liu, Y., Liu, L., Leung, J.Y. et al. 2020. Sequentially Coupled Flow and Geomechanical Simulation with a Discrete Fracture Model for Analyzing Fracturing Fluid Recovery and Distribution in Fractured Ultra-Low Permeability Gas Reservoirs. *Journal of Petroleum Science and Engineering* **189**: 107042.

Mirani, A., Marongiu-Porcu, M., Wang, H. et al. 2018. Production-Pressure-Drawdown Management for Fractured Horizontal Wells in Shale-Gas Formations. *SPE Reservoir Evaluation & Engineering* **21** (03): 550-565.

Moridis, G. 2014. User's Manual of the TOUGH+ Core Code v1.5: A General-Purpose Simulator of Non-Isothermal Flow and Transport through Porous and Fractured Media. *Lawrence Berkeley National Laboratory*. LBNL Report #: LBNL-6871E. https://escholarship.org/uc/item/4t3204ft.

Moridis, G. 2017. High Resolution Investigations of Flow and Thermal Processes During Production from Hydraulically Fractured Ultra-Low Permeability Media. In *SPE Latin America and Caribbean Petroleum Engineering Conference*: Society of Petroleum Engineers.ISBN 1613995334.

Okouma Mangha, V., Guillot, F., Sarfare, M. et al. 2011. Estimated Ultimate Recovery (Eur) as a Function of Production Practices in the Haynesville Shale. In *SPE annual technical conference and exhibition*: Society of Petroleum Engineers.ISBN 1613991479.

Olorode, O., Freeman, C.M., Moridis, G. et al. 2013. High-Resolution Numerical Modeling of Complex and Irregular Fracture Patterns in Shale-Gas Reservoirs and Tight Gas Reservoirs. *SPE Reservoir Evaluation & Engineering* **16** (04): 443-455.

Palacio, J. and Blasingame, T. 1993. Decline Curve Analysis Using Type Curves: Analysis of Gas Well Production Data. *paper SPE* **25909**: 12-14.

Rojas, D. and Lerza, A. 2018. Horizontal Well Productivity Enhancement through Drawdown Management Approach in Vaca Muerta Shale. In *SPE Canada Unconventional Resources Conference*: Society of Petroleum Engineers.ISBN 1613995822.

Rutqvist, J. and Moridis, G.J. 2007. Numerical Studies on the Geomechanical Stability of Hydrate-Bearing Sediments. In *Offshore technology conference*: Offshore Technology Conference.ISBN 1555632548.

Rutqvist, J. and Tsang, C.-F. 2002. A Study of Caprock Hydromechanical Changes Associated with Co 2-Injection into a Brine Formation. *Environmental Geology* **42** (2-3): 296-305.

Settari, A. and Mourits, F. 1994. Coupling of Geomechanics and Reservoir Simulation Models. *Computer Methods and Advances in Geomechanics* **3**: 2151-2158.

Settari, A. and Walters, D.A. 2001. Advances in Coupled Geomechanical and Reservoir Modeling with Applications to Reservoir Compaction. *Spe Journal* **6** (03): 334-342.

Stone, H. 1970. Probability Model for Estimating Three-Phase Relative Permeability. *Journal of Petroleum Technology* **22** (02): 214-218.

Terzaghi, K. 1939. 45th James Forrest Lecture, 1939. Soil Mechanics-a New Chapter in Engineering Science. *Journal of the Institution of Civil Engineers* **12** (7): 106-142.

Terzaghi, K. (1943). Theoretical Soil Mechanics. JohnWiley & Sons. *New York*, 11-15.

Thomas, L.K., Hellums, L., and Reheis, G. 1972. A Nonlinear Automatic History Matching Technique for Reservoir Simulation Models. *Society of Petroleum Engineers Journal* **12** (06): 508-514.

Todd, H. B., and Evans, J. G. 2016. Improved Oil Recovery IOR Pilot Projects in the Bakken Formation. Society of Petroleum Engineers. https://doi.org/10.2118/-180270-MS.

US DOE. 2013. EIA/ARI World Shale Gas and Shale Oil Resource Assessment, EIA report.

U.S. Energy Information Administration (EIA), 2008; 2011; 2012. *Annual Energy Review*. /http://www.eia.gov/totalenergy/data/annual/

Valkó, P.P. 2009. Assigning Value to Stimulation in the Barnett Shale: A Simultaneous Analysis of 7000 Plus Production Histories and Well Completion Records. Paper presented at the *SPE Hydraulic Fracturing Technology Conference*, The Woodlands, Texas, 19-21 January 2009. Society of Petroleum Engineers. DOI: 10.2118/119369-MS.

Valkó, P.P. and Lee, W.J. 2010. A Better Way to Forecast Production from Unconventional Gas Wells. Paper presented at the *SPE Annual Technical Conference and Exhibition*, Florence, Italy, 19-22 September 2010. Society of Petroleum Engineers. DOI: 10.2118/134231-MS.

Wilson, K. 2015. Analysis of Drawdown Sensitivity in Shale Reservoirs Using Coupled-Geomechanics Models. In *SPE Annual Technical Conference and Exhibition*: Society of Petroleum Engineers.ISBN 1613993765.

Wang, Z. (2018). Asymptotic Solutions to the Diffusivity Equation: Validation and Field Applications. College Station, TX: Texas A&M University. (PhD Dissertation)

Wang, Z., Malone, A., King, M.J. (2019). Quantitative production analysis and EUR prediction from unconventional reservoirs using a data-driven drainage volume formulation. *Computational Geosciences*. (doi: 10.1007/s10596-019-09833-8)

Wang, Z., Malone, A., King, M.J. (2018). Quantitative Production Analysis and EUR Prediction From Unconventional Reservoirs Using a Data-Driven Drainage Volume Formulation. *EAGE European Conference on the Mathematics of Oil Recovery*. Barcelona, Spain, 3-6 September 2018. (ECMOR-46177, doi: 10.3997/2214-4609.201802244)

Wang, Z., Chen, L., King, M.J. (2017). Validation and Extension of Asymptotic Solutions of Diffusivity Equation and Their Applications to Synthetic Cases. *SPE Reservoir Simulation Conference*. Montgomery, TX, USA, 20-22 February 2017. (SPE-182716-MS, doi: 10.2118/182716-MS)

Zoback, M.D. 2010. *Reservoir Geomechanics*: Cambridge University Press. Original edition. ISBN 0521146194.